UNIVERSIDAD COMPLUTENSE DE MADRID

FACULTAD DE CIENCIAS BIOLÓGICAS

Departamento de Bioquímica y Biología Molecular I

TESIS DOCTORAL

Role of autophagy in neurodegeneration and new for its study

(Papel de la autofagia en la neurodegeneración y nuevas herramientas para su estudio)

MEMORIA PARA OPTAR AL GRADO DE DOCTOR

PRESENTADA POR

Lucía García Ledo

Directora

Patricia Boya

Madrid, 2015

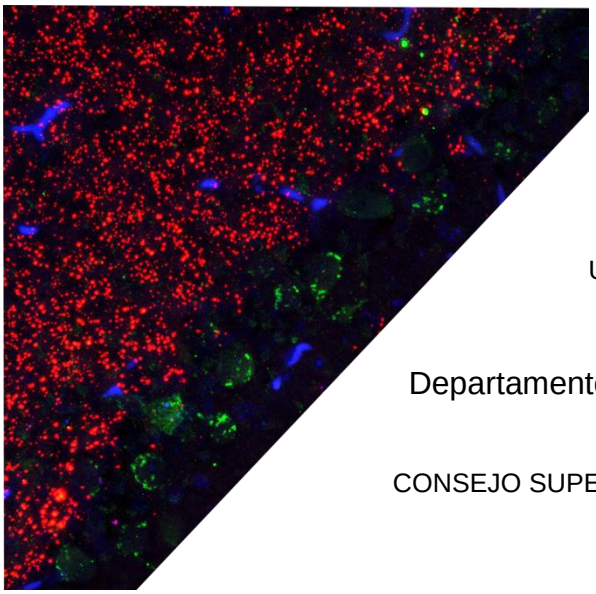

UNIVERSIDAD COMPLUTENSE DE MADRID

FACULTAD DE CIENCIAS BIOLÓGICAS

Departamento de Bioquímica y Biología Molecular I

CONSEJO SUPERIOR DE INVESTIGACIONES CIENTÍFICAS

Centro de Investigaciones Biológicas

Role of autophagy in neurodegeneration and new tools for its study

(Papel de la autofagia en la neurodegeneración y nuevas herramientas para su estudio)

Lucía García Ledo

TESIS DOCTORAL

2015

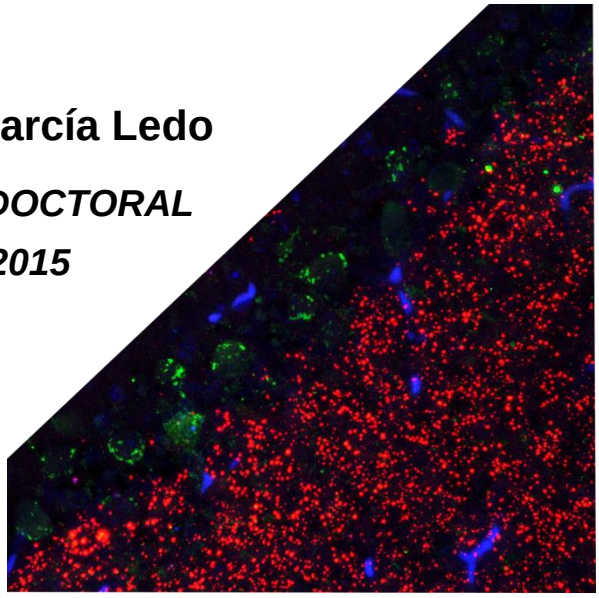

Universidad Complutense de Madrid
Facultad de Ciencias Biológicas
Departamento de Bioquímica y Biología Molecular I

“Role of autophagy and neurodegeneration and new tools for its study”

“Papel de la autofagia y nuevas herramientas para su estudio”

Thesis submitted for the degree of Doctor of Philosophy by Lucía García Ledo at the Universidad Complutense de Madrid, Department of Biochemistry and Molecular Biology.

Memoria presentada por Lucía García Ledo para optar al grado de Doctora en Bioquímica y Biología Molecular por la Universidad Complutense de Madrid

Vº Bº de la Directora de Tesis,
Dra. Patricia Boya

Vº Bº del tutor,
Dr. Guillermo Velasco Díez

Lucía García Ledo
2015

Agradecimientos

Me gustaría agradeceros a todos los que de un modo u otro habéis participado en la realización de esta tesis.

En primer lugar, gracias a la Dra. Patricia Boya por haberme dado la oportunidad de formar parte de su equipo, por su apoyo durante esta etapa y por guiarme con tanta energía a través del mundo de la autofagia. Al "3D lab", gracias por la creación de un ambiente de intercambio y apoyo: Dra. Flora de Pablo, Dra. Catalina Hernández, Dra. Teresa Suárez y, en especial al Dr. Enrique de la Rosa, por sus aportaciones y su espíritu de bienvenida durante estos años. Gracias también a la Dra. Ana María Cuervo por haberme permitido realizar una estancia en su laboratorio. Ha supuesto para mí una experiencia muy enriquecedora a todos los niveles. Mi agradecimiento también a la empresa Wimasis, que me ha permitido descubrir una nueva perspectiva de la ciencia. Y, por supuesto, gracias al Ministerio de Educación y Ciencia, actualmente Ministerio de Competencia, por la financiación de esta tesis doctoral.

Gracias, además, a toda esa gente que hace que el CIB funcione cada día: las chicas de la limpieza, de esterilización, personal de compras, conserjes, seguridad… y, en especial, al personal de servicios (Pedro de citometría, Maite y las chicas del confocal y Fernando en microscopía electrónica) y a la gente del animalario (Carlos, Dani, Esther…) por vuestra gran labor.

Cómo no, gracias a toda la gente del Boya lab, desde los comienzos con Natalia, Marta y Kike, que ya no están pero que con paciencia me introdujeron en este laboratorio, hasta las nuevas incorporaciones: Raquel, Sergio y Elena que, aunque apenas hayamos coincidido, siempre están dispuestos a echar una mano. Pero, sobre todo, a Lore, ese alma paralela, a Esther, por su apoyo y enseñanzas y a Ana, por su alegría y disposición. ¡Muchas gracias a todos!

Por supuesto, gracias también al resto de la familia: a los chicos del 101 (Alberto y Jose- "equipo consolider"- y Marchena), a las chicas del 100 (Patri V, Ana y ahora también Noe) y las chicas del 107 (Marisa y María). Muchas gracias a todos por vuestro tiempo, vuestra paciencia, ayuda y apoyo.

Gracias también a todos los que durante estos años me habéis acompañado en esta experiencia desde fuera del labo: a todos los viejos conocidos y a todos los que se cruzaron en el camino aportando siempre una nueva visión.

Y, para terminar, me gustaría agradecérselo a mi familia, en especial a mis padres, y a Íñigo.

Resumen

La **autofagia** es un mecanismo celular de degradación lisosomal que permite el *reciclaje* de componentes celulares diversos. Sus funciones principales incluyen proporcionar energía y aminoácidos y contribuir al mantenimiento de la proteostasis celular. Es un mecanismo basal presente en todos los tejidos pero también una respuesta a estrés, principalmente a la falta de nutrientes, además de hipoxia o estrés oxidativo entre otros (Boya et al., 2013).

Se conocen tres tipos de autofagia según el modo en que el material a degradar es llevado hasta el lisosoma: macroautofagia, autofagia mediada por chaperonas (CMA) y microautofagia. Las dos primeras son las más descritas. **Macroautofagia** se caracteriza por la formación de *autofagosomas*, vesículas de doble membrana recubiertas con *LC3*, que engloban una parte del citoplasma para ser degradada. El material degradado por macroautofagia puede variar desde proteínas que han finalizado su función celular hasta orgánulos enteros, pasando por lípidos o glucógeno (Boya et al., 2013; Ezaki et al., 2011; Singh and Cuervo, 2011). **CMA** es un sistema más específico que consiste en la degradación de proteínas que expongan la *secuencia de aminoácidos KFERQ*. Esta secuencia es reconocida por la chaperona *Hsc70*, que transporta la proteína hasta el lisosoma. Una vez allí, es translocada al lumen lisosomal mediante el receptor *LAMP-2A*. Se sabe que CMA está implicada no sólo en la eliminación de proteínas solubles alteradas o cuya vida media ha finalizado, sino también en procesos específicos como eliminación de reguladores transcripcionales o enzimas durante una adaptación metabólica. A pesar de sus matices diferenciales, se ha visto que en ciertos tejidos y condiciones la falta de una ruta puede ser compensada por la otra (Kaushik et al., 2008).

La función de la autofagia en todos los tejidos parece indiscutible pero, sin embargo, es especialmente relevante en tejidos constituidos en los que no hay renovación celular, como el sistema nervioso central (Ghavami et al., 2014; Mizushima et al., 2008; Tanaka and Matsuda, 2014). La mayor prueba de ello son modelos como el del ratón ***Atg5*$^{flox/flox}$; nestin-*Cre*** (Hara et al., 2006), que carecen de proteínas iniciadoras del proceso de autofagia específicamente en el sistema nervioso central. Estos ratones, presentan neurodegeneración a distintos niveles en todo el cerebro, demostrando que la autofagia a nivel basal es necesaria para la correcta homeostasis del tejido. Además, la función autofágica se ha visto que está comprometida en conocidos procesos de neurodegeneración como en la enfermedad de Alzheimer o Huntington (Frake et al., 2015). Asimismo, estas patologías suelen estar asociadas con el **envejecimiento**, que se caracteriza, entre otros puntos, por el declive de la autofagia (Lopez-Otin et al., 2013), sugiriendo que el declive de la autofagia podría ser uno de los factores, si no causantes, sí agravantes de la neurodegeneración, remarcando el papel necesario de la autofagia para el mantenimiento de la homeostasis del sistema nervioso central.

La **retina** es un componente del sistema nervioso central pero a día de hoy el papel de la autofagia en la fisiología de la retina es bastante desconocido. La retina es una región altamente estructurada. Presenta tres capas nucleares donde se alojan los somas de las neuronas que la integran: la capa nuclear externa (siglas en inglés: ONL-outer nuclear layer), la

capa nuclear interna (INL, inner nuclear layer) y la capa de células ganglionares (GCL-ganglion cell layer). Entremedias de estas tres capas se encuentran dos capas plexiformes: la plexiforme externa (OPL-outer plexiform) y la interna (IPL-inner plexiform layer), que contienen los procesos de las neuronas y es donde tiene lugar la sinapsis entre las neuronas de las distintas capas. La neurorretina es la encargada de la captación de fotones y su transformación en información eléctrica. Esta transformación tiene lugar en los *fotorreceptores*, situados en la ONL. Los fotorreceptores pueden ser de dos tipos: bastones o conos. Los *bastones* llevan a cabo la visión en condiciones de luz mínimas (visión nocturna) y los *conos* son los encargados de la visión en condiciones de gran cantidad de luz (visión diurna). El siguiente paso en la transmisión de información son las *células bipolares* (específicas para bastones o conos), situadas en la INL y el último eslabón son las *células ganglionares* (en la GCL), cuyo axón constituye el nervio óptico que envía la información hasta los núcleos visuales. En paralelo a esta transmisión, se encuentran en la INL se encuentran neuronas moduladoras de la señal, denominadas células *amacrinas y horizontales* (Cuenca et al., 2015; Kolb, 2003).

La retina está formada también por células no neuronales, como la *macroglia* (que incluye astrocitos y glía radial, denominada glía de Müller) y la *microglía*, que se encargan de la respuesta inflamatoria del tejido. Además, la macroglia tiene funciones muy importantes como mantenimiento del balance iónico en el medio extracelular, eliminación de neurotransmisores sobrantes en el medio extracelular o soporte metabólico de las neuronas. El otro componente no neuronal de la retina es el *epitelio pigmentario*, en la parte más externa de la retina, que recubre a los fotorreceptores a los que les dan soporte físico y metabólico (Cuenca et al., 2015; Kolb, 2003)

Además, la retina presenta la particularidad de estar más expuesta a agentes externos que suelen derivar en generación de especies reactivas de oxígeno (Cuenca et al., 2015). Por eso cabría pensar que la autofagia podría tener un papel relevante en este tejido. Sin embargo, la relación de la autofagia con la homeostasis de la retina es poco conocida. Se ha descrito que la autofagia está implicada en la eliminación de residuos del ciclo visual en el epitelio pigmentario, que está implicada en la regulación de la fototransducción y que la falta de proteínas relacionadas con la autofagia a distintos niveles incrementa la sensibilidad al daño de la retina (Zhou et al., 2015{Chen, 2013 #8307)}. Resultados previos de nuestro laboratorio muestran que la autofagia tiene un papel protector en un modelo de glaucoma, una de las primeras causas mundiales de ceguera, y también han mostrado que la autofagia está disminuida con la edad, al igual que el resto del sistema nervioso (Rodriguez-Muela et al., 2012).

Por todo ello, el **objetivo** de esta tesis ha sido el estudio del papel de la *autofagia* en la *neurodegeneración* en la retina mediante la utilización del modelo murino *Atg5* $^{flox/flox}$; nestin-*Cre* y su comparación con los cambios observados en *retinas envejecidas*. Además, para generalizar nuestros resultados, hemos evaluado las consecuencias de la falta de autofagia en el cerebelo de los ratones *Atg5* $^{flox/flox}$; nestin-*Cre* y las hemos comparado con el fenotipo en retina. De forma adicional, durante el proceso hemos colaborado con una empresa en el

desarrollo de herramientas informáticas para optimizar el análisis de imágenes de autofagia y apoptosis, con el fin de mejorar el propio estudio.

La **determinación del fenotipo del modelo murino *Atg5* $^{flox/flox}$; nestin-*Cre*** en retina se ha realizado mediante un *estudio funcional y morfológico* para comprobar la integridad y funcionalidad de los distintos componentes de la neurorretina. Además, hemos chequeado el estado de *activación de la macroglia* como respuesta a un posible daño tisular y lo hemos comparado con retinas envejecidas. Hemos comprobado, también, el grado de *afectación de la proteostasis* en la retina de los ratones *Atg5* $^{flox/flox}$; nestin-*Cre* debido a la falta de macroautofagia y lo hemos comparado con retinas envejecidas. Finalmente, hemos estudiado si podría existir compensación de la falta de macroautofagia mediante un incremento de *CMA*. Estos resultados fueron contrastados con el fenotipo en cerebelo de los ratones *Atg5* $^{flox/flox}$; nestin-*Cre* para comprobar su generalización.

El **estudio funcional** de la retina de ratones *Atg5* $^{flox/flox}$; nestin-*Cre* se realizó mediante un electrorretinograma de campo lleno, que permite el estudio de la respuesta funcional de la retina en condiciones escotópicas (visión nocturna) y fotópicas (visión diurna). La respuesta obtenida en condiciones escotópicas en estos ratones es significativamente reducida en comparación con hermanos control, mientras que la respuesta obtenida en condiciones fotópicas no presenta diferencias. Este resultado indica que la respuesta derivada de la señalización de bastones es deficiente, mientras que la derivada de conos es normal.

A continuación, realizamos el **estudio morfológico** de la retina centrado en las anomalías detectadas en el electrorretinograma. En primer lugar, observamos el estado de la capa nuclear de los fotorreceptores y encontramos que se estaba produciendo degeneración de fotorreceptores, en concreto de bastones, en consonancia con lo observado en el electrorretinograma. Encontramos también, mediante inmunotinción específica, que las células bipolares de bastón presentaban signos de remodelación, a consecuencia de la degeneración de bastones, y que las células horizontales presentaban una localización anómala.

Una vez confirmada la degeneración de la retina, procedimos a observar si existía una respuesta de **activación de la macroglia**. Mediante inmunotinción con GFAP de los astrocitos de retinas en plano, se determinó que las retinas *Atg5* $^{flox/flox}$; nestin-*Cre* presentaban astrocitos con signos de activación como hipertrofia y ramificación, en comparación con las retinas control. También se comprobó si en retinas envejecidas (12 y 24 meses), que previamente se ha descrito que presentan neurodegeneración y alteración funcional (Kolesnikov et al., 2010b; Rodríguez-Muela, 2011), observábamos que los astrocitos presentaban un alto grado de activación en comparación con controles a 3 meses.

Posteriormente, se realizó el estudio del **estado de la proteostasis** en la retina de los ratones *Atg5* $^{flox/flox}$; nestin-*Cre*. Para ello medimos los niveles de p62 (una proteína que se acumula en el citoplasma en caso de reducción de la actividad autofágica) mediante western blot y observamos que, al igual que en cerebro, están incrementados. Realizamos también una inmunotinción de p62 en cortes transversales de retina para comprobar si algunas células

sufrían más la alteración proteostática que otras y observamos que, si bien hay un aumento general de p62 en todas las capas, hay una acumulación destacada en la capa de la IPL. Realizamos la comprobación de proteostasis también en retinas envejecidas, ya que datos de nuestro laboratorio muestran un declive de la autofagia asociado a la edad (Rodríguez-Muela, 2011). En este caso encontramos un aumento de p62 detectado por western blot y una mayor acumulación de p62en todas las capas, revelado por inmunotinción. Sin embargo, en este caso se aprecia mayor acumulación en los somas neuronales y no en los procesos, como en retinas *Atg5* $^{flox/flox}$; nestin-*Cre*.

Finalmente comprobamos si el bloqueo de macroautofagia podría estar compensado con un incremento de la actividad de **CMA**, especialmente en los conos, ya que estaban evitando la degeneración. Para ello, determinamos mediante western blot los niveles de las proteínas clave: LAMP-2A y Hsc70, y observamos que estaban incrementados. Para un estudio más dinámico de la actividad de macroautofagia y CMA, realizamos ensayos *in vitro* con la línea celular 661w, derivada de conos de ratón. Para ello silenciamos la expresión de Atg7 (proteína necesaria para macroautofagia) o LAMP-2A (proteína necesaria para CMA). Con el indicador de actividad de CMA fotoactivable (Koga et al., 2011b) pudimos determinar que ésta estaba incrementada en las células con bloqueo de macroautofagia. Sin embargo, cuando medimos la actividad de autofagia, encontramos que las células carentes de CMA ni siquiera alcanzaban los niveles de macroautofagia de las células control. La cuantificación de la actividad de autofagia se realizó cuantificando autofagosomas detectados por inmunotinción de LC3 mediante análisis de imagen con la herramienta WimAutophagy desarrollada en colaboración con la empresa Wimasis. Finalmente, sometimos a estas líneas a un tratamiento con paraquat, inductor de estrés oxidativo, y observamos que las células sin LAMP-2A presentaban mayores niveles de muerte. Esto sugiere que la ruta de CMA podría ser crucial para la supervivencia de las células 661w en situaciones de estrés y, teniendo en cuenta la diferencia en la degeneración entre conos y bastones en los ratones *Atg5* $^{flox/flox}$; nestin-*Cre,* quizá también para los conos.

Para comprobar si este mecanismo sucedía en otras regiones del sistema nervioso central, estudiamos el **cerebelo** de ratones *Atg5* $^{flox/flox}$; nestin-*Cre*. Observamos por westernblot que los niveles de p62 y LAMP-2A estaban muy incrementados frente al control. Por inmunotinción, pudimos observar que el incremento era excluyente, es decir, las células con un mayor nivel de p62 no presentaban un incremento en LAMP-2A (células granulares), y viceversa (células de Purkinje). Además, en la descripción de modelo por Hara et al. (2006) se muestra un patrón de muerte diferente entre ambos tipos celulares, siendo las células granulares más sensibles a la falta de macroautofagia que las células de Purkinje. Esto, en conjunto con las diferencias en los niveles de CMA y degeneración observados entre conos y bastones, sugiere que las células de Purkinje pudieran estar más protegidas de la muerte por la compensación por CMA.

Durante el periodo del estudio presentado, se realizó una colaboración con la compañía Wimasis para el **desarrollo de herramientas informáticas** para el estudio de

neurodegeneración. Se desarrollaron dos módulos, WimAutophagy y WimApoptosis, para el análisis de imagen cuantitativo de ensayos celulares de autofagia y apoptosis. WimAutophagy se aplicó para la cuantificación de macroautofagia en líneas celulares, como se ha mencionado anteriormente. Se trata de algoritmos robustos y flexibles que permiten el tratamiento de imágenes procedentes de microscopía de epifluorescencia y confocal, distintas líneas celulares, e incluso tejidos, y ambos permiten identificar varios marcadores para facilitar el estudio. WimAutophagy permite la detección y cuantificación de autofagosomas con distintos marcajes de LC3 e, incluso, marcadores de CMA (LAMP-2A). WimApoptosis permite la cuantificación de células apoptóticas con las aproximaciones más comunes: tamaño nuclear, inmunotinción de caspasa3 activa y tinción de TUNEL (Terminal deoxynucleotidyl transferase dUTP Nick End Labeling).

Conclusiones

La eliminación de Atg5 en células progenitoras neurales de ratón induce *neurodegeneración* en la retina, afectando principalmente a los bastones y sus células bipolares, lo que genera un *defecto en la visión nocturna y activación de macroglía*. Retinas envejecidas, que también presentan principalmente afectación en la ruta de los bastones (Kolesnikov et al., 2010b), presentan además activación de la macroglía.

La ausencia de Atg5 en precursores neurales y el declive de autofagia derivado del envejecimiento alteran la proteostasis de la retina (Rodríguez-Muela, 2011), produciendo la *acumulación de p62 en todas las capas*, aunque *de manera diferencial en los dos modelos*.

La alteración de la proteostasis observada en ratones *Atg5* $^{flox/flox}$; nestin-*Cre* y retinas envejecidas parece ser *compensada por un incremento de CMA*. Aunque esta compensación parece general en todas las capas de la retina, hay un patrón diferencial de la presencia de Hsc70 entre fotorreceptores. Esto, en conjunto con el estudio de las células 661w y los estudios funcionales y morfológicos realizados, parece indicar que los conos podrían ser capaces de compensar la falta de macroautofagia con un incremento de CMA, aunque no viceversa, mientras que los bastones serían más dependientes de macroautofagia para su supervivencia.

Además, los datos obtenidos en cerebelo de ratones *Atg5* $^{flox/flox}$; nestin-*Cre*, mostrando un *patrón excluyente* de la presencia en citoplasma de p62 y LAMP-2A en células granulares y de Purkinje, refuerzan las observaciones en retina y sugieren que la capacidad de un tipo celular para incrementar las distintas rutas de autofagia o la capacidad para compensar la falta de una de ellas podría estar detrás de patrones de muerte tipo celular-dependiente.

Summary

Autophagy is a cellular mechanism of lysosomal degradation that allows the recycling of cellular components. The main functions of autophagy include to provide energy and amino acids and to contribute to cellular proteostasis. Autophagy is a basal mechanism present in all tissues but it is also a stress response, particularly to nutrient starvation as well as to hypoxia or oxidative stress (Boya et al., 2013).

There are described three types of autophagy, depending on how the material is carried to the lysosome for its degradation: macroautophagy, chaperone mediated autophagy (CMA) and microautophagy. The two former are the most studied. **Macroautophagy** is characterized by the formation of *autophagosomes*, which are double membrane vesicles coated with *LC3*, that engulf a portion of the cytoplasm for its degradation. The target material for macroautophagy can vary from long-lived proteins to whole organs, including also lipids or glycogen (Boya et al., 2013; Ezaki et al., 2011; Singh and Cuervo, 2011). **CMA** is a more specific system that targets cytoplasmic soluble proteins which expose the *KFERQ amino acid motif*. This sequence is recognized by the *Hsc70* chaperone, which carries the protein to the lysosome. There, it is translocated into the lysosomal lumen by *LAMP-2A*. CMA is involved not only in the elimination of long-lived proteins or altered proteins, but also the elimination of transcription factors or enzymes during a metabolic adaptation. Besides, their slight differences, it has been shown that under certain conditions, the lack of one pathway can be compensated by the other (Kaushik et al., 2008).

The function of autophagy in all tissues seems unquestionable, especially for tissues lacking cellular renovation, as the central nervous system (CNS) (Ghavami et al., 2014; Mizushima et al., 2008; Tanaka and Matsuda, 2014). The **main probe** of that, are the mice models as the *Atg5*$^{flox/flox}$; nestin-*Cre* mouse (Hara et al., 2006), that have a specific lack of macroautophagy in their CNS. These mice models present neurodegeneration at different levels in the whole brain, demonstrating that basal autophagy is necessary for the proper homeostasis of the tissue. Besides, it has been shown that the autophagic function is reduced in some neurodegenerative processes as Alzheimer's or Huntington's diseases (Frake et al., 2015). Moreover, these pathologies are usually associated with **aging**, which is characterized by autophagic decline (Lopez-Otin et al., 2013). This suggests that the autophagic impairment could be a causing or, at least, an aggravating factor of neurodegeneration and remarks the necessary role of autophagy for the maintenance of CNS homeostasis.

The **retina** is a part of the CNS, but nowadays the role of autophagy in its physiology is poorly understood. The retina is a region highly structured. It has three nuclear layers, which host the somas of the neurons: outer nuclear layer (ONL), inner nuclear layer (INL) and ganglion cell layer (GCL). In between of these layers there are two plexiform layers: the outer plexiform layer (OPL) and the inner plexiform layer (IPL), where the synapses take place. The neurorretina transforms the photons into electrical information. This transformation takes place in the *photoreceptors*, which are placed in the ONL. There are two kinds of photoreceptors: *rods* and

cones. Rods work at minimal light conditions (nocturnal vision) and cones work at higher light conditions (diurnal vision). The next step on the information transmission chain in the retina is the *bipolar cells* (specific for rods or cones), placed at the INL. The last step are the *ganglion cells* (at the GCL), whose axons form the optic nerve, to send the information to the brain. In addition, in the neurorretina there are modulatory neurons, called am*acrine cells and horizontal cells* (Cuenca et al., 2015; Kolb, 2003).

The retina also includes non-neuronal cells, such as *macroglia* (astrocytes and Müller cells) and *microglia*, which carry out the inflammatory response in the tissue. Besides, macroglia also regulates the ionic balance of the extracellular media, elimination of neurotransmitters excess or metabolic support of the neurons. The other non-retinal component of the retina is the *pigment epithelium*, in the outer side of the retina, which surrounds photoreceptors and provides them physical and metabolic support (Cuenca et al., 2015; Kolb, 2003).

Furthermore, the retina has the particularity that it is more exposed to external agents than the brain itself, and they can derive in the formation of reactive oxidative species (Cuenca et al., 2015). Thus, autophagy could have an interesting role in this tissue, as it can eliminate oxidized products. However, the *relation of autophagy and retinal homeostasis* is widely unknown yet. It is known that autophagy is involved in the elimination of residues from the visual cycle, participates in the regulation of the phototransduction and that the lack of certain autophagic proteins increases the sensitivity to retinal damage (Zhou et al., 2015{Chen, 2013 #8307)}. Previous results from our laboratory show that autophagy has a protective role in glaucoma model, one the main causes of blindness, and they also show that autophagy declines with age, as it does in the rest of the CNS (Rodriguez-Muela et al., 2012).

Therefore, the **objective** of this thesis was the study of the role of *autophagy in neurodegeneration* by using the *Atg5* $^{flox/flox}$; nestin-*Cre* mouse model and the comparison of this model with *aged retinas*. To generalize these results, we also evaluated the consequences of the lack of autophagy in the cerebellum of *Atg5* $^{flox/flox}$; nestin-*Cre* mice to compared them with the phenotype in the retina. In addition, during the process we have collaborated in the *development of informatics tools* to optimize the imaging analysis of autophagy and apoptosis assays, to improve the study itself.

For the **characterization of the retinal phenotype** in the *Atg5* $^{flox/flox}$; nestin-*Cre* mouse model, we performed a *functional and morphological study* to test the functionality and integrity of the components of the neurorretina. Besides, we checked the *macroglia activation state* in response to possible tissue damage in *Atg5* $^{flox/flox}$; nestin-*Cre* and aged retinas. We have also studied the level of *proteostasis alteration* in *Atg5* $^{flox/flox}$; nestin-*Cre* retinas and compared it to aged retinas. Finally, we studied the existence of a compensation of the lack of macroautophagy by an increase of *CMA* in the retina. To generalize our findings, we have evaluated the consequences of autophagy down-regulation in the cerebellum and compared the phenotype with that found in the retina.

The **functional study** of *Atg5* $^{flox/flox}$; nestin-*Cre* mice was performed by a full field electroretinogram, that includes the study of the retinal response in scotopic conditions (nocturnal vision) and photopic conditions (diurnal vision). The obtained response in scotopic conditions in these mice was significantly reduced compared to control littermates, while the photopic response was not altered. This result indicates that the signalling performed by rods is deficient, while the cones response is normal.

Hereafter, we performed a **morphologic study** of the retina, focused on the anomalies indicated by the electroretinogram. First, we check the state of the photoreceptors nuclear layer (ONL) and we found that the retina of *Atg5* $^{flox/flox}$; nestin-*Cre* mice was undergoing degeneration, in particular rods, in accordance with the electroretinogram response. We also found out by specific immunostaining that rod bipolar cells presented remodelling signs, as a consequence of the rod degeneration, and that horizontal cells were in an anomalous position.

Once, confirmed that degeneration was occurring in *Atg5* $^{flox/flox}$; nestin-*Cre* retinas, we proceed to observe if there was an **activation response from macroglia**. We performed a GFAP immunostaining on flat-mount retinas to visualize astrocytes and we found that *Atg5* $^{flox/flox}$; nestin-*Cre* retinas presented signs of activation as hypertrophy and ramification, compared to control retinas. We performed the same approach on aged retinas (12 and 24 months), that are known to present neurodegeneration and functional alteration (Kolesnikov et al., 2010b; Rodríguez-Muela, 2011), and we observed that astrocytes presented too signs of activation, compared to 3 month-old controls.

Later, we analysed the **proteostasis state** in the retina of *Atg5* $^{flox/flox}$; nestin-*Cre*. We measure the levels of p62 (a protein that is accumulated in the cytoplasm when autophagy is reduced) by western blot and we found that, as in brain, they were increased. We performed a immunostaining for p62 on retinal cryosections to check if some cells would suffer more intensely the proteostatic alteration and we observed that there is a general increase of p62 in all layers, but particularly in the IPL.

We also performed the proteostasis analysis in aged retinas, as they present autophagic decline associated to age (Rodríguez-Muela, 2011). Here, we found that there is an increase of p62, detected by westernblot, and accumulation of p62 along all the retinal layers. However, in this case there is more accumulation on the neuronal somas and not in the processes, as seen in *Atg5* $^{flox/flox}$; nestin-*Cre* retinas.

Finally, we checked if the macroautophagy blockage could be compensated by an enhancement of the **CMA activity**, especially in cones, as they were avoiding degeneration. For that, we determined by western blot the levels of Hsc70 and LAMP-2A, the key proteins of the process, and we observed that they were increased. For a more dynamic study of macroautophagy and CMA, we performed *in vitro* assays with the cone derived cell line 661w, where we silenced the expression of Atg7 (necessary protein for macroautophagy) and LAMP-2A (necessary protein for CMA). We measure the CMA activity with a photoactivable reporter (Koga et al., 2011b) and it was increased in the cells with macroautophagy blockage. However,

when measure the levels of macroautophagy, we found that the cells lacking CMA were not able to reach the control levels. The measurement of macroautophagy activity was performed by quantifying LC3 immunostained autophagosomes by the WimAutophagy tool, developed in collaboration with Wimasis company. Finally, we challenged the cells with paraquat, an oxidative stress inductor, and we observed that cells lacking LAMP-2A presented higher levels of cells death. This suggests that CMA pathway could be crucial for 661w survival in stress conditions and, taken into account the observed difference between cones and rod degeneration in *Atg5* $^{flox/flox}$; nestin-*Cre* mice retinas, it seems that it could also be for cones.

To test if the compensatory mechanism could also be extrapolated to other CNS regions, we studied the **cerebellum** of *Atg5* $^{flox/flox}$; nestin-*Cre* mice. We checked by western blot that the levels of p62 and LAMP-2A were enhanced compared to control. By performing a immunostaining of these proteins, we could observe that they presented an excluding pattern: cells with p62 accumulation did not present LAMP-2A increase (granule cells), and viceversa (Purkinje cells). Besides, the description by Hara et al. (2006) shows that there is a different cell death pattern among these cell types: granule cells are more sensitive to the lack of macroautophagy than Purkinje cells. All this, together with the differences in CMA levels and degeneration between cones and rods, suggests that Purkinje cells could be more protected from cell death because of CMA compensation.

During the period of time of this study, we collaborated with Wimasis company for the **developing of informatics tools** for the study of neurodegeneration. Two modules were developed for the analysis of autophagy and cell death cellular assays: WimAutophagy and WimApoptosis. As mentioned, WimAutophagy was used for the cell line analysis of macroautophagy activity. These modules include robust and flexible algorithms that allow the treatment of images from epifluorescence and confocal microscopy, different cell lines and even tissue, and both allow the detection of a variety of markers to facilitate the study. WimAutophagy can perform the detection and quantification of autophagosomes with different LC3 labelling and, even, CMA labelling as LAMP-2A. WimApoptosis performs the quantification of apoptotic cells with the most frequent approaches: nuclear size, active caspase 3 mmunostaining and TUNEL staining (Terminal deoxynucleotidyl transferase dUTP Nick End Labeling).

Conclusions

The elimination of Atg5 in neural progenitor cells in mouse induces *neurodegeneration* in the retina, mainly affecting rods and their bipolar cells, which leads to *poor night vision* and to *macroglia activation*. Aged retinas, which also show a principal affectation of the rod pathway (Kolesnikov et al., 2010b), presented macroglia activation too.

The lack of Atg5 in neural progenitor cells in mouse and the autophagy decline described in aged retinas (Rodríguez-Muela, 2011) alter the retinal proteostasis, leading to the *accumulation of p62* along all the layers, but following a *different pattern of distribution*.

The alteration of the proteostasis observed in *Atg5* $^{flox/flox}$; nestin-*Cre* and in aged retinas seem to be *compensated by a CMA enhancement*. Although the compensation seems general to all retinal layers, there is a differential pattern of the distribution of Hsc70 among the photoreceptors. This, combined with the studies performed in 661w cells and the functional and morphological studies of these retinas suggests that cones might be able to compensate the absence of macroautophagy by increasing CMA activity, but not vice versa, while rods would be more dependent on macroautophagy for their survival.

In addition, the data obtained in cerebellum of *Atg5* $^{flox/flox}$; nestin-*Cre* mice, showing an *excluding pattern* of the presence in the cytoplasm of p62 and LAMP-2A in granule and Purkinje cells, reinforce the previous conclusions in retina and suggest that the ability of a cell type to enhance the different autophagic pathways or the ability to compensate the lack of one of them could be underneath cell type-dependent death pattern.

INDEX

1. INTRODUCTION

1. INTRODUCTION

1.1. AUTOPHAGY: MAIN CHARACTERISTICS AND TYPES

Autophagy is a generic term to define the pathways by which cytoplasmic materials are delivered into the lysosome for their degradation and recycling (Boya et al., 2013). It was firstly described as the blooming of “microbodies” around the nucleus of rat hepatic cells after glucagon administration (Ashford TP, 1962). In 1963, at the Ciba Foundation Symposium of lysosomes, Novikoff presented the “cytolysosomes” which are structures clearly related to lysosomes with diverse content such as mitochondria, endoplasmic reticulum membrane and other cytosolic components, in an obvious state of decomposition.This accumulation of cytosolic content in those lysosomal related structures was later found in various tissues and physiological conditions by Novikoff and other researchers. (Novikoff, 1963). Finally, at this symposium, Christian de Duve suggested to differentiate between heterophagic and autophagic functions of lysosomes, depending on the origin of their content; moreover he also proposed to name the “cytolysosomes” as “autophagic vacuoles” (Klionsky, 2008). It was finally established when the laboratory of Duve published two papers about the role of glucagon on autophagy in

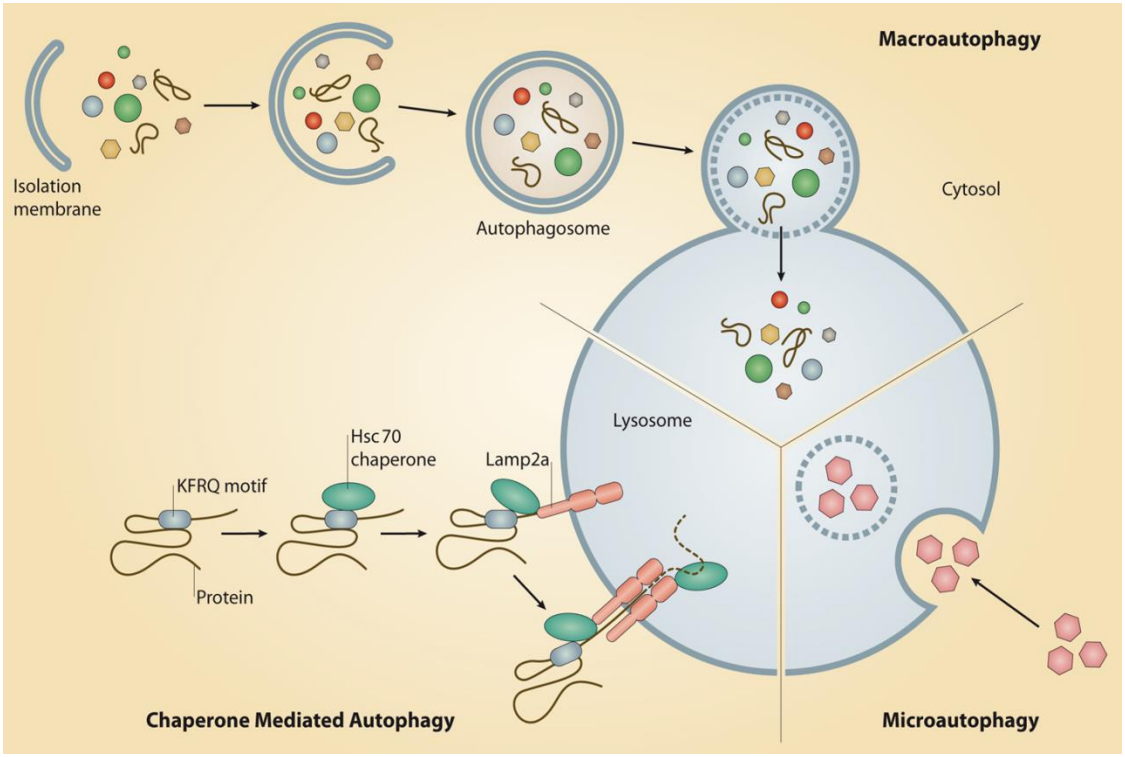

Figure 1.1 The different classes of autophagy. (a) Macroautophagy hallmark is the autophagosome: a double membrane vesicle that engulfs a portion of cytoplasm and finally fuses with lysosome for degradation and degradation. (b) During chaperone-mediated autophagy, proteins carrying the pentapeptide KFERQ-like sequence are recognized by the Hsc70 chaperone, which then associates with the integral lysosome membrane protein LAMP-2A, triggering its oligomerization. This event leads the translocation of the bound protein into the lysosome interior through a process that requires Hsc70. (c) Microautophagy entails the recruitment of targeted components in proximity with the lysosomal membrane, which subsequently invaginates and pinches off.

rat hepatocytes, and the participation of lysosomes on autophagy respectively (Deter et al., 1967; Deter and De Duve, 1967). This new perspective opened the door to a new cell biology field. The main boost of the field came after the discovery of the autophagy related genes. They were first described in *Saccharomyces cerevisiae* by the laboratory of Ohsumi in 1993 and named as *APG* (AutoPhaGy) genes (Tsukada and Ohsumi, 1993), and many others contributed to unravel the genes implicated in different steps of the process (Harding et al., 1995; Mukaiyama et al., 2002; Sakai et al., 1998; Thumm et al., 1994; Titorenko et al., 1995; Tsukada and Ohsumi, 1993; Yuan et al., 1997). With all these contributions, many nomenclatures appeared until the proposal of unification in 2003 for Autophagy Related Genes (ATG) (Klionsky et al., 2003). After the identification of the atg genes many other landmarks for autophagy emerged, such as the discovery of the conjugation of Atg5-Atg12 (Mizushima et al., 1998) and the finding of LC3 as an autophagic membrane marker (Kabeya et al., 2000), and shortly after, its relation with pathology (such as relating Beclin1 knockout with tumorigenesis (Qu et al., 2003)).

Nowadays, it is known that not only one type of autophagy exists but three types, depending on how the cargo is delivered into the lysosome. The three types of autophagy are macroautophagy, chaperone mediated autophagy and microautophagy (Figure 1.1). The two former are the most studied and will be detailed below.

1.1.1. MACROAUTOPHAGY

Macroautophagy is the most widely known form of autophagy in the three types and in most of the cases is simply called as “autophagy”. Its hallmark is the formation of autophagosome: a double membrane vesicle that engulfs the cargo and further fuse with lysosomes for degradation and recycling. Autophagosomes are formed as the closure of an isolation membrane (also termed phagophore) that engulfs a small portion of the cytoplasm -such as protein aggregates or damaged organelles (Figure 1.1). Next, autophagosomes fuse with lysosomes to become autolysosomes and degrade the cargo. Autophagosomes also may fuse with endosomes to form amphisomes before fusion with lysosomes (Boya et al., 2013).

1.1.1.1. Macroautophagic machinery

Macroautophagy is a ubiquitous system in eukaryotic cells that takes place can be divided in five stages: induction, nucleation, elongation and maturation, lysosome fusion and content degradation. A schematic representation of the multi-step process is shown in Figure 1.2.

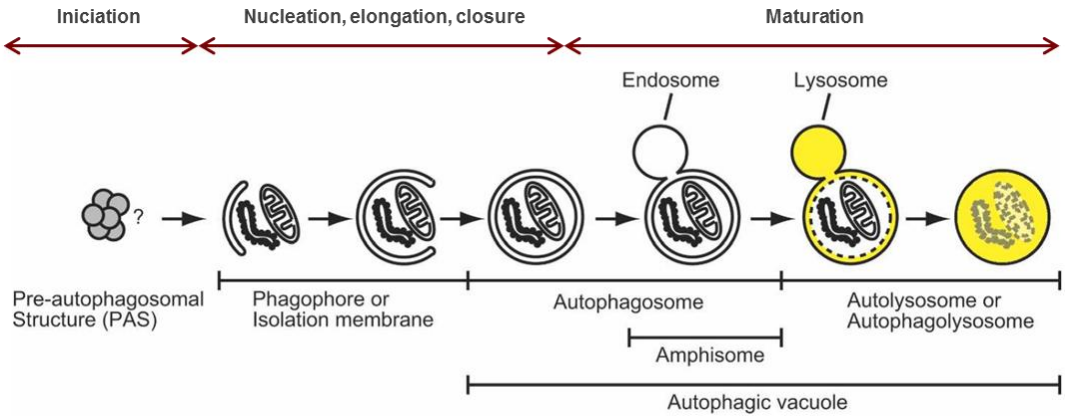

Figure 1.2. The process of macroautophagy in mammalian cells. A portion of cytoplasm, including organelles, is enclosed by a phagophore or isolation membrane to form an autophagosome. The outer membrane of the autophagosome subsequently fuses with the endosome and then the lysosome, and the internal material is degraded. In yeast, autophagosomes are generated from the PAS, which has not yet been identified in mammalian cells. The nomenclature for various autophagic structures is indicated as well as the different steps (Modified from Mizushima (2007).

Induction

In yeast, it is described that the process is always initiated in the same locationnamed PAS (pre-autophagosomal structure), but in mammals it can occur ubiquitously in the cell. The origin of the membrane of the autophagosomes has not been defined as a unique source but with various sources such as plasma membrane, Golgi, endoplasmic reticulum and mitochondria (Hamasaki et al., 2013; Lamb et al., 2013). In any case, membranes enriched in PtdIns3P to recruit the autophagic proteins seem to be necessary (Koyama-Honda et al., 2013).

Nucleation

There are two complexes necessary for the nucleation of the autophagosomes (APs): the phosphoinositide 3-kinase complex III (PI3KC3) and the Ulk1 (unc-51-like kinase 1) complex (Figure 1.3). The PI3KC3 is formed by Vps34, Vps15, Atg14, and Beclin1. Vps34 is a PI3K class III kinase that phosphorylates phosphatidylinositol to PtdIns3P, the indicator of the origin of the phagophore formation (Kihara et al., 2001) which recruits the early autophagosome biogenesis proteins (Abada and Elazar, 2014). The Ulk complex includes FIP200, Atg13 and Ulk1 itself. Ulk1, under stress conditions, is released from the inactive mTOR, autophosphorylating itself and Atg13. mTOR, Atg13 and FIP200 induce the formation of the phagophore (Jung et al., 2009). As Ulk1 seems to be located on the surface of the lysosomes to interact with mTOR, it has been suggested that Ambra-1 could be involved in shuttling Ulk1 complex to the phagophore formation site (Di Bartolomeo et al., 2010). Thus, Ulk1 transmits the information about the metabolic status of the cell sensed by mTOR to the downstream autophagic machinery.

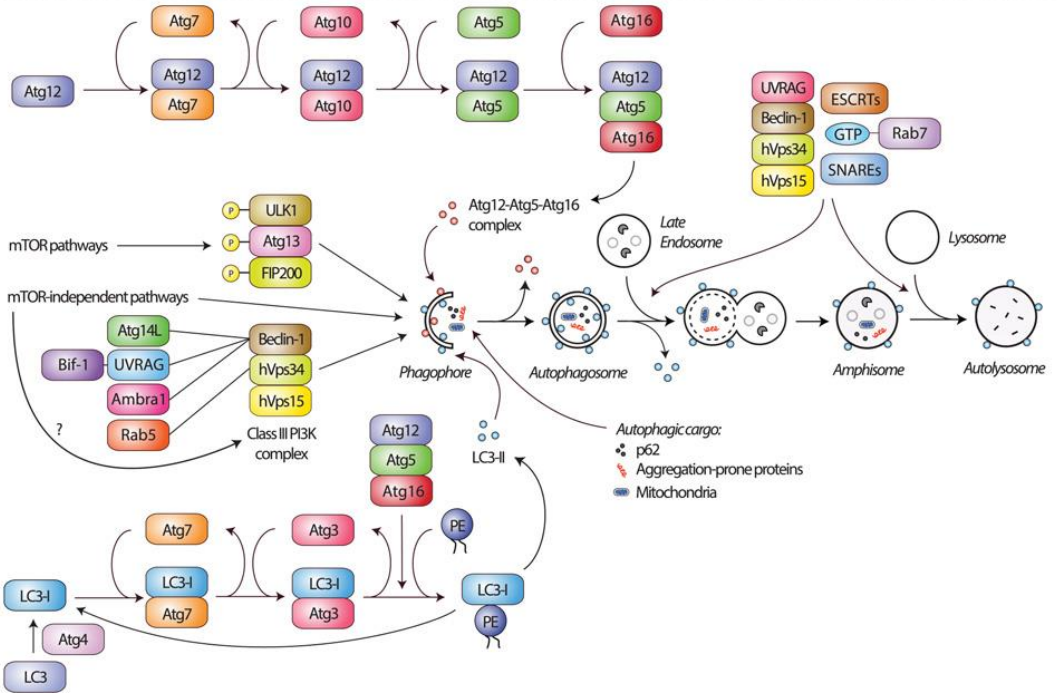

Figure 1.3 The mammalian autophagy pathway and its regulatory machinery. Autophagy is induced by mTOR dependent and independent pathways. The ULK1–Atg13–FIP200 complex regulates autophagosome synthesis downstream of the mTOR signalling pathways. Also, the PI3KC3 complex, comprising hVps34, Beclin-1 and hVps15, regulates autophagosome synthes, which is possibly downstream of the mTOR-independent pathways. Several Beclin-1 interactors, such as Atg14L, UVRAG, Bif-1 and Ambra1, or Rab5 interacting with hVps34, positively modulate this process. Two ubiquitin-like conjugation systems including Atg proteins are implicated in the elongation of phagophores. The Atg5–Atg12 conjugation involves Atg7 (E1-like) and Atg10 (E2-like), whereas the LC3–PE conjugation involves Atg7 (E1-like) and Atg3 (E2-like). The Atg5–Atg12 conjugate forms a complex with Atg16, Atg5-Atg12-Atg16, which has E3-like activity towards LC3–PE conjugation (LC3-II). LC3-II is a specific autophagy marker that is degraded in the autolysosomes as well as delipidated by Atg4 and recycled. Autophagosome maturation entails fusions with late endosomes and lysosomes, mediated by Rab7, ESCRT proteins, SNARE proteins and the UVRAG–Beclin-1–hVps34–hVps15 complex. Autophagic cargo such as p62, aggregation-prone proteins or mitochondria, are degraded in the autolysosomes. Modified scheme from Sarkar 2013.

Elongation and closure

Two conjugation systems participate in this step: Atg5-Atg12-Atg16 and LC3, which are tightly interconnected (Figure 1.3).

LC3 is synthesized in a preform that undergoes a maturing process by Atg4, which leads to the C-terminal cleavage, producing LC3-I. Then, LC3-I is activated by Atg7, transferred to Atg3, and together with the Atg5-Atg12 system, LC3-I is lipidated with phospatidylethanolamine (PE), which is known as LC3-II, and inserted in the phagophore membrane (Mizushima et al., 2011)

During the formation of the Atg5-Atg12-Atg16 conjugation system, Atg12 is activated by Atg7, transferred to Atg10 and finally conjugated with the target Atg5, originating Atg5-Atg12 complex. Finally, Atg5-Atg12 conjugate interacts with Atg16L. It has been shown that Atg5-Atg12

interacts with Atg3 to facilitate the transfer reaction of LC3 from Atg3 to PE, while Atg16L seems to be involved in the location of LC3 lipidation (Mizushima et al., 2011).

Besides Atg5-Atg12-Atg16 and LC3, elongation is in part regulated by Atg9 that provides lipid membrane to the membrane from different organelles (Rogov et al., 2014; Young et al., 2006). It is placed on the outer side of the membrane of the autophagosome until it is mature, when the protein is detached (Yamamoto et al., 2012). In addition, Atg9 has been shown to be required for the autophagosome closure, as its multimerization allows the fusion of membranes (Reggiori et al., 2005; Young et al., 2006). Atg4, aside from the participation in the LC3 conjugation, participates in its deconjugation, removes LC3-II from the autophagosome membrane, which facilitates the maturation of these structures into fusion-capable autophagosomes (Yu et al., 2012).

Autophagosome maturation

After their closure, autophagosomes can fuse in first place with late endosomes, originating amphisomes, and posteriorly fuse with the lysosomes to form autolysosomes (Figure 1.2). These fusion events involve many proteins (Figure 1.3). Rubicon and UVRAG are Beclin1-binding proteins that regulate maturation of autophagosomes and endocytic transport. The complex Beclin1-hVsp34-hVps15-UVRAG upregulates the maturation of autophagosomes, while the addition of the protein Rubicon to the complex downregulates the process. UVRAG stimulates Rab7 (which mediates tethering between vesicular membranes) and recruits C Vsp proteins. Moreover SNAREs protein such as syntaxin-17, late endosomal/lysosomal VAMP8 (vesicle-associated membrane protein 8) and ESCR proteins are implicated be involved in the fusion with multivesicular bodies (Sarkar, 2013).

Cargo degradation

The degradation of the content engulfed by APs is dependent on lysosomes. The syntaxin-5 SNARE complex regulates endoplasmic reticulum- Golgi transport through the secretory pathway that is essential for the activity of lysosomal proteases such as cathepsins for autophagic degradation (Renna et al., 2011). Impairing the lysosomal proteolytic function by preventing lysosomal acidification (for example with bafilomycin A1 or ammonium chloride) or inhibiting its protease activity (with leupeptine or E64d) retards autophagosome maturation and autophagic cargo clearance (Klionsky et al., 2012; Yamamoto et al., 2011).

1.1.1.2. Regulation of autophagy

Autophagy is an active mechanism in basal conditions in all cell types, at different levels, with its activity alleviated under stressed conditions. The most potent inducer of autophagy is starvation, specially amino acids deprivation, meanwhile low energy levels, growth factors retrieval or oxidative stress could also induce autophagy (Abada and Elazar, 2014).

The main regulator of autophagy is the metabolism master *mTOR* (mammalian target of rapamycin), an inhibitor of the process. It is an integrator of multiple signals of the metabolic status of the cell and responds to them by modulating vital activities such as protein translation or cell growth. Thus, many homeostatic variations of the cell state can affect the autophagic activity (Sarkar, 2013). mTOR presents two different functional complexes: mTOR complex 1 (mTORC1) and mTOR complex 2 (mTORC2) (Sarkar, 2013). mTORC1 regulates autophagy by direct interaction with the Ulk1 complex which is an autophagy promoter. Under nutrient-rich conditions, mTORC1 phosphorylates Ulk1 and Atg13, inactivating both and, thus, preventing autophagy (Figure 1.3). In starvation, Ulk1 is dissociated from mTORC1, which dephosphorylates and activates Ulk1, to induce autophagy (Jung et al., 2009). mTORC2 regulates autophagy indirectly through the activation of Akt (Abada and Elazar, 2014).

The classical inducer of autophagy is **starvation**, especially amino acid starvation. It has been described that Rag (Ras-related GTP-binding protein) complex acts as an aminoacid sensor on the lysosome surface (Sancak et al., 2010). It is formed by heterodimers of RagA/B and RagC/D, the vacuolar protein pump vATPase and a multi-protein signalling complex known as Ragulator. Under low concentration of amino acids, Rag complex remains inactive. In the presence of amino acids, the Rag complex activates and interacts with raptor which sequesters mTORC1 to the lysosome surface and inactivates it. Rag GTPases seem to be also implicated in the glucose sensing (Efeyan et al., 2013), acting then as an integrator of both glucose and amino acid signals.

Autophagy can also be regulated by **growth factors.** Insulin**,** which reports the information about the nutritional state of the organism, is implicated to regulate autophagy. Insulin or IGFs receptor pathways activate PI3KI which, in turn, activates Akt and its pathway activates mTORC1, thus inhibiting autophagy (Inoki et al., 2002; Zhang et al., 2003). Serum starvation, a frequently used method for inducing autophagy, is known to activate GSK3 (Glycogen synthase kinase 3) that activates Ulk1 (Lin et al., 2012).

Cell **energy levels** influence autophagy activity as well. When AMP is in excess, it binds and activates AMPK. APMK induces autophagy through many pathways. AMPK phosphorylates Raptor, which inhibits mTORC1 (Gwinn et al., 2008). It also phosphorylates and activates Ulk1, Vps34 and Beclin1(Kim et al., 2013a). **Oxidative stress** is another described inducer of autophagy and it exerts the regulation through many pathways as Beclin1 up-regulation, or p53 up-regulation that inhibits mTOR (Gibson, 2013). In mammals it is known that during starvation, mitochondria increase their reactive oxidative species (ROS) production, which transiently and locally inhibits Atg4, stabilizing LC3-II. In fact, this ROS production by mitochondria could be a

signal to be eliminated by autophagy (Abada and Elazar, 2014; Scherz-Shouval and Elazar, 2011).

1.1.1.3. Macroautophagy functions

Autophagy, as shown in the previous section, has a clear implication in cell metabolism homeostasis, contributing in degrading different substrates. As autophagy is strongly induced by starvation or low energy levels conditions, it is considered as an energy supplier process in which free amino acids can be generated and can be integrated in the tricarboxylic acid cycle for energy production (Boya et al., 2013). Nowadays, it is also known that autophagy can degrade other substrates such as lipid droplets in liver cells, rendering free fatty acids for energy obtaining (Ezaki et al., 2011; Singh et al., 2009), and also glycogen (Singh and Cuervo, 2011). In fact, autophagy is critical during the perinatal starvation, when there is an adaptation to the new nourishment, as knocked out mice for Atg5, Atg3, Atg7 or Atg9 proteins die in neonatal stages and show reduced levels of amino acids in plasma and tissues (Komatsu et al., 2006; Kuma et al., 2004; Sou et al., 2008).

Autophagy is also known to be involved in proteostasis maintenance by degrading proteins that have already accomplished their life-span as well as damaged or aggregated proteins to obtain free amino acids for metabolism and macromolecular support. This contribution is especially important in some post-mitotic cells such as neurons and podocytes at the renal glomeruli (Hara et al., 2006; Hartleben et al., 2014).

Thus, autophagy contributes to cell homeostasis by recycling proteins or organelles that are no longer required as a source of amino acids, lipids and carbohydrates for synthesis or energy supply.

1.1.1.4. Macroautophagy and cargo specificity

Autophagy was first defined as a non-selective mechanism but evidences started growing about cargo-recognition processes (Figure 1.4). Accordingly, the delivery to the autophagosome is generally ensured by interaction of the adaptor protein both with the membrane-anchored form of LC3 and the main targets that are polyubiquitinylated (Lippai and Low, 2014). Usually, the receptors present a LIR motif (LC3 interaction region) that interacts directly with LC3 and a domain to detect ubiquitinated proteins, such as UBA (C-terminal ubiquitin-binding domain), and another domains for oligomerization, self-aggregation or interaction with other receptors, such as PB1 (Phox and Bem 1) or coiled-coil domains.

p62 (sequestosome 1, SQSTM1) is an adaptor protein ubiquitously expressed. It presents three domains that confer its functionality. p62 presents a PB1 domain, responsible for self-aggregation and association with other adaptors such as NBR1 (neighbour of BRCA1 gene), a LIR motif and a UBA domain that interacts with ubiquitinated proteins (Rogov et al., 2014). Once linked to the tagged protein and LC3, is integrated in the autophagosome and degraded

(Lamark et al., 2009). Impairment of autophagy flux is accompanied by accumulation of p62, forming large aggregateswhich include p62 and ubiquitin (Komatsu et al., 2007).

In addition to p62, other adaptor proteins or autophagy receptors have been described, such as NBR1 (neighbour of BRCA1 gene 1). NBR1 presents, as p62, a PB1 domain, a LIR motif and a UBA domain and it detects ubiquitinated proteins in a dependent and independent fashion of p62. It is also accumulated during autophagy flux blockage. Optineurin is another adaptor protein for selective autophagy that, thanks to its UBAN (Ubiquitin binding in ABIN and NEMO domain) and UBZ (ubiquitin-binding zinc finger) domains, is able to interact with misfolded proteins even if they are or not ubiquitinated, and NDP52 (nuclear dot protein 52 kDa) also with a UBZ domain (Rogov et al., 2014).

The most studied processes of selective autophagy are mitophagy: the specific elimination of damaged or excessive numbered mitochondria; aggrephagy: the removal of altered or misfolded protein aggregates; xenophagy: the selective autophagy of pathogenic intracellular parasites (bacteria, protozoa, or viruses) and pexophagy: peroxisome autophagic disposal. These selective autophagy functions are more related to some of the receptors, even if p62 is

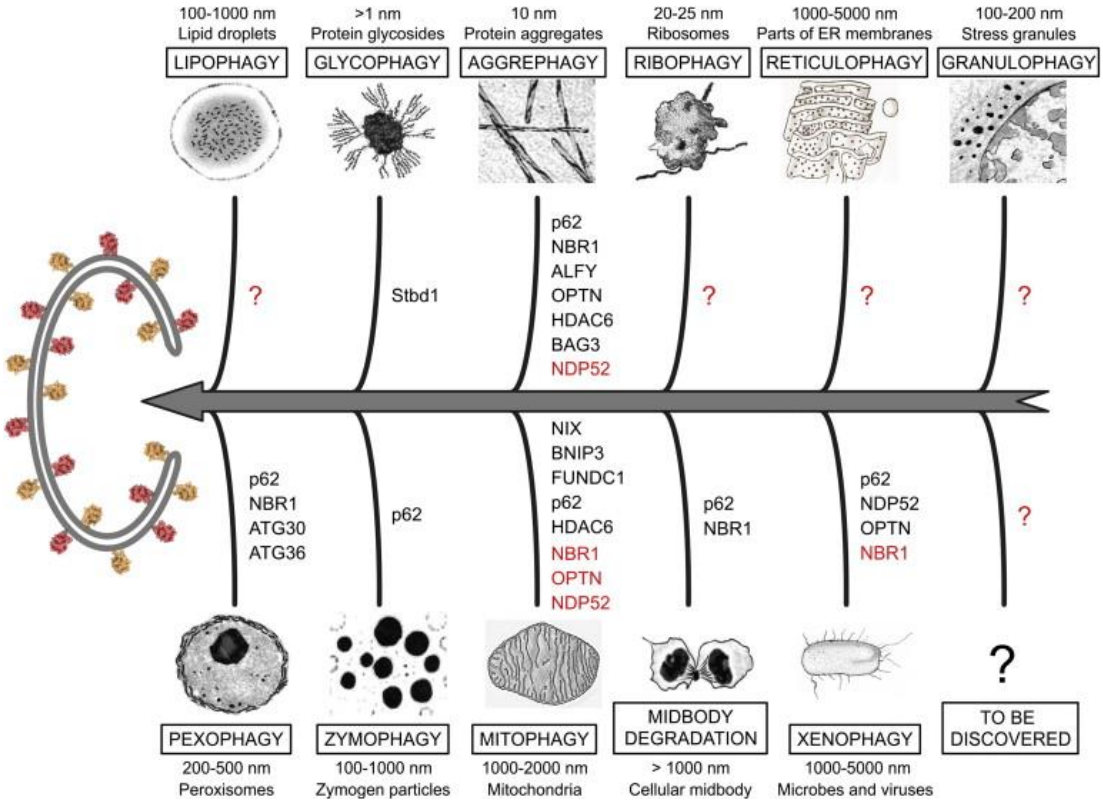

Figure 1.4. Types of selective autophagy in mammals. Established (black) and putative (red) selective autophagy receptors for the respective processes are listed. Question marks indicate as-of-yet unidentified receptor proteins. Extracted from Rogov et al. (2014).

so far involved in all of them. For example, NBR1 with pexophagy and mitophagy and optineurin and NDP52 with xenophagy (Figure 1.4)(Lippai and Low, 2014).

1.1.2. CHAPERONE MEDIATED AUTOPHAGY (CMA)

Chaperone mediated autophagy is a proteolytic system, exclusive of mammalian cells, that targets specific cytoplasmic proteins to the lysosome. It occurs in five steps: a) individual recognition of cytoplasmic soluble proteins, b) protein binding, c) unfolding, d) translocation inside the lysosome for degradation and e) disassembly of LAMP-2A (Cuervo and Wong, 2014). It is exemplified in Figure 1.5.

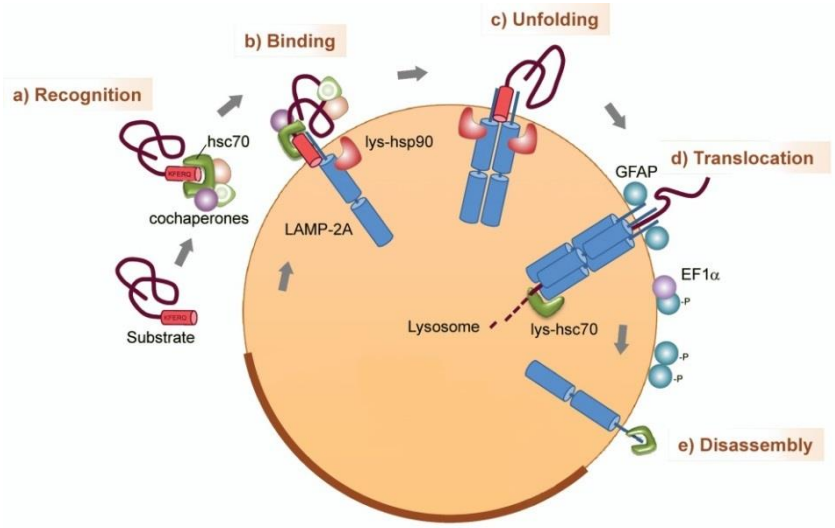

Figure 1.5. Steps and regulation of CMA. Steps: (a) Recognition of substrate proteins by hsc70/ cochaperones; (b) binding of substrate-chaperone complex to LAMP-2A; (c) unfolding of the substrate; (d) LAMP-2A multimerization, substrate translocation and subsequent degradation; (e) disassembly of LAMP-2A multimer/translocon. Modified from Kaushi and Cuervo, 2012.

The selectivity of the pathway relies on the amino acid motif KFERQ present in the target proteins recognized by the chaperone Hsc70. The eligibility of a protein for CMA degradation depends on the exposition of the motif to the chaperone Hsc70. This chaperone, helped by others, also unfolds the proteins. Then the protein binds to the cytosolic tail of LAMP-2A (lysosome-associated membrane protein type 2A) causing LAMP-2A multimerization and protein translocation inside the lysosome lumen for enzymatic degradation. When the protein is delivered inside the lysosome, LAMP-2A monomerizes to prepare for the next round of CMA (Kaushik and Cuervo, 2012).

The limiting step in the CMA pathway is LAMP-2A, but there are some more players in the process (Cuervo and Dice, 2000).

1.1.2.1. Functions

CMA participates in the cell balance both in basal state and during stress response by eliminating proteins selectively. In basal conditions, CMA participates in maintenance of protein quality control by selectively eliminating unfolded or aggregated proteins, as well as it contributes by eliminating proteasome subunits (Cuervo et al., 1995). CMA also participates in the regulation of some specific cellular contexts as the regulation of transcription factors by their

elimination (Aniento et al., 1996; Cuervo et al., 1998), the elimination of liver enzymes involved in glycolysis and lipogenesis for metabolic adaptation to nutritional changes (Schneider et al., 2015), MHC class II antigen presentation by macrophages (Rajagopal et al., 2006; Zhou et al., 2005) or inT cell activation through the targeted degradation of negative regulators of T cell activation (Valdor et al., 2014).

Furthermore, CMA is upregulated in response to stress, as nutrient deprivation, oxidative stress and proteotoxicity (Schneider et al., 2015), participating in the elimination of altered or aggregated proteins as well as providing energy by the integration of the amino acids into the Krebs cycle (Massey et al., 2006).

Therefore, CMA is great machinery for specific elimination of altered or no longer required proteins and a source of free amino acids and energy for the cell.

1.2. CENTRAL NERVOUS SYSTEM: retina and cerebellum

The central nervous system (CNS) is formed by three components: the encephalon (the brain, contained in the cranium), the medullar component (inside of the spinal column) and the ocular component (the retina and optic nerves) (Puelles López et al., 2008). As the present study is focused on retina and cerebellum (a region of the brain) we will detail the structure of these regions bellow.

1.2.1. Retina organization

The retina is a highly organized tissue responsible of encoding the light intensity as an electric signal. It is formed by three cellular layers with two synaptic layers in between, working as a chain of transmission and modulation of the visual information that will be latterly sent to the brain, to create the final image Figure 1.6.

The first step of the visual information cascade takes place in the photoreceptors, in the outer position of the retina. Their cells bodies are grouped in the outer nuclear layer (ONL). Photoreceptors capture photons and transform this information into a membrane potential. There are two types of photoreceptors: rods and cones. Rods are able to detect even a single photon and thus are specialized on dim-light perception or scotopic vision (nocturnal vision). Cones are 100 times less sensitive but they are faster in phototransduction, so they are specialized on bright light and colour detection, as there are different types of cones that present diverse pigments that allow them to detect different wave lengths, so they are specialized in colour vision (diurnal or photopic vision) (Hoon et al., 2014).

Photoreceptors synapse at the *outer plexiform layer (OPL)* with the next link in the chain, the second order neurons: the bipolar cells, specific for rods or cones. They can be classified into OFF or ON bipolars, but only cones present both types, while rods present only ON bipolar cells. Bipolar cell bodies are placed at the *inner nuclear layer (INL)* and the synapse with the third order neurons: the retinal ganglion cells (RGC) at the *inner plexiform layer (IPL).*

The last step in the chain, are the retinal ganglion cells that form the *ganglion cell layer (GCL),* whose axons are packed forming the optic nerve that will send the information to the brain (Hoon et al., 2014).

In addition, there are two types of cells that module the excitation and response, whose somas are placed at the INL: horizontal cells and amacrine cells. Horizontal cells regulate transmission

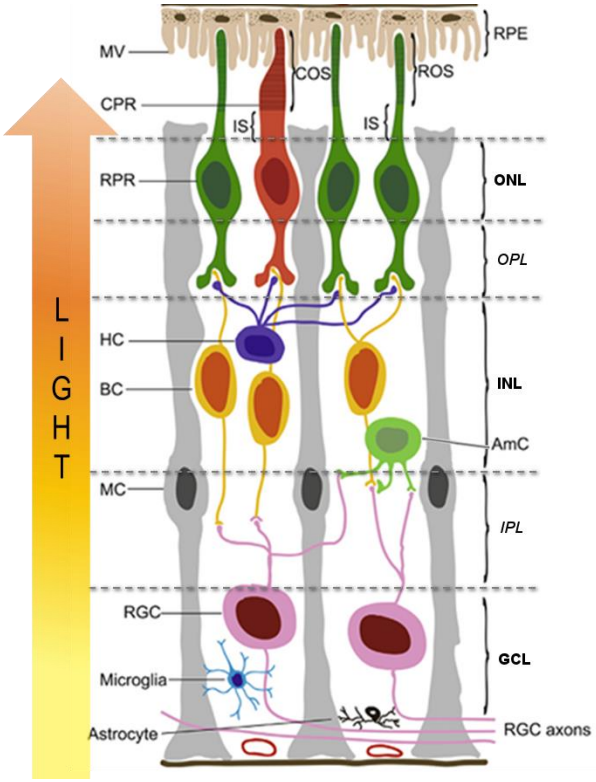

Figure 1.6 Schematic representation of the cellular components of the mammalian retina. In the outer side of the retina, the photoreceptors lay on the REP (retinal pigment epithelium) that extends microvilli (MV) to increase the contact surface. Photoreceptors are divided in four parts: outer segment (COS: cones outer segment, ROS: rods outer segment); inner segment (IS); nucleus, placed at the outer nuclear layer (ONL) and the synaptic button, at the outer plexiform layer (OPL). At the OPL photoreceptors synapse with the horizontal (HC), the bipolar (BC) and the amacrine cells (AmC), whose cell bodies lay at the inner nuclear layer (INL). Lastly, the cells of INL synapse with the retinal ganglion cells (RGC) at the inner plexiform layer (IPL). The cell bodies of RGCs form the ganglion cell layer (GCL). Also Müller cells (MC), astrocytes and microglia are represented at their basal position. Modifed from Athanasiou et al. (2013).

at the level of photoreceptors- bipolars transmission, improving the chromatic contrast, and amacrine cells at the bipolar-ganglion cells level, refining movement detection (Kolb, 2003).

There are also some non-neuronal cells important for the retina with different roles: the glial cells and pigment cells. The glial cells, composed by Müller cells, astrocytes and microglia are responsible for the damage response in the retina. Besides, Müller cells, helped by astrocytes, are in charge of the maintenance of the retinal glucose metabolism, ion and pH control, neurotransmitters clearance and provision of neurotransmitters precursors to neurons (Cuenca et al., 2015). Pigment cells, that form the *retinal pigment epithelium (RPE),* surround the photoreceptors and give them physical and metabolic support. They are basic to complete the visual cycle as they help photoreceptors to eliminate the trans-retinol generated after light reception by phagocyting fragments of their external segments (Boya and Codogno, 2013). RPE is also important as they contain granules with melanin, a pigment that traps the electrons once they crossed the retina, avoiding rebounds that would alter the perception (Kolb, 2003).

1.2.2. Cerebellum organization

The cerebellum is a part of the encephalon that is placed in the posterior face. It is responsible for comparing the performed movement to the previously planned and sends signals for correction to motor control centers (Puelles López et al., 2008). It has two hemispheres separated by a structure called *vermis*. The organization of the cerebellum is quite stereotyped in all the regions. It is divided in cortex (highly lobulated), white matter (placed from the cortex to the ventricle) and nuclei (around the ventricle) (Puelles López et al., 2008).

The most conspicuous cells of the cerebellum are the Purkinje cells, whose cell bodies form an orderly monolayer called Purkinje cells layer, placed between the granular and molecular layers. Purkinje cells extend their planar "fan-like" dendritic trees into the molecular layer above. As these cells are the sole output neurons of the cerebellar cortex, they are central to cerebellar cortical information processing Figure 1.7) (Apps and Garwicz, 2005).

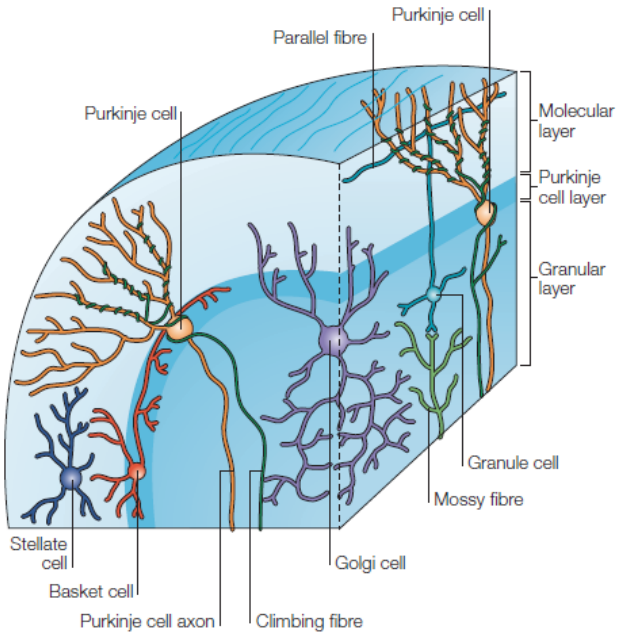

Figure 1.7 Schematic representation of the cerebellar cortex organization showing the three layers: the molecular layer, containing the dendrites of Purkinje cells, the parallel fibres of the granule cells and stellate cells; Purkinje cell layer containing Purkinje cells somas and granular layer that contains Golgi cells and granule cells, that receive the input from the mossy fibres. Also climbing fibres cross the granular layer to reach Prukinje cells in the other two layers. Scheme modified from Apps and Garwicz (2005).

The *molecular layer* contains mainly dendrites, axons and microglia but also some dispersed neurons. The main axons are the parallel fibres, which arise from the granular layer and synapse with the dendritic arborisations of Purkinje cells on their way. The neurons placed in this layer are the stellate and basket cells, whose dendrites synapses with the axon of Purkinje cells (Puelles López et al., 2008).

The inner *granular layer* is the thickest layer and it is packed with small neurons called granule cells, as well as Golgi cells and Lugaro cells, but in a much smaller proportion. Granule cells axons ascend to the molecular layer where the bifurcate forms the parallel fibres that synapse with Purkinje cells dendrites. Granular cells receive aferences from the mossy fibres (with different origins as spinal cord or the mesencephalon) and inhibitory sypnases from the Golgi cells (Apps and Garwicz, 2005; Puelles López et al., 2008).

1.3. NEURODEGENERATION AND AUTOPHAGY

Neurodegeneration is a term commonly used but hard to define. Etymologically, it derives from "neuro-", which means neuron and "-degeneration" which means the loss of structure and function. Thus, in the strict sense, it defines any pathologic condition that affects primarily neurons, but actually it includes a great and heterogeneous group of neurological diseases with different pathophysiology and clinic that affect specific subsets of neurons in specific functional anatomic systems, with unknown triggers and irreversible progress (Przedborski et al., 2003b).

Most of the human neurodegenerative diseases are linked to intra-cytoplasmic inclusions of aggregate-prone proteins in neurons. Autophagy is a potent mechanism to remove them, but neurons are particularly vulnerable to alterations in the autophagic-endocytic-lysosomal pathway, especially as the central nervous system ages. Therefore, interest on the function of autophagy in the CNS is increasing as autophagy appears as possible target for neurodegenerative diseases therapy (Frake et al., 2015; Nixon, 2013).

In the next sections we will review the role of basal autophagy in the brain and the retina, in their physiology and pathology, how CMA is also involved and the contribution of the aging factor.

1.3.1. Macroautophagy and CNS physiology

Autophagy is a process that occurs in all tissues at basal levels, although the levels are different among tissues. Neurons present very low levels of basal and induced autophagy compared to other cell types and, however, autophagy has been shown to be basic for neuron functionality, especially because of the size and post-mitotic nature of the neurons, and their great energetic demand (Ghavami et al., 2014; Mizushima et al., 2008; Tanaka and Matsuda, 2014). The main probe of the relevance of autophagy for the CNS are mouse models that illustrate the fragility of CNS in lack of some of the starter proteins of the autophagic process, and we will put a special emphasis on the *Atg5*$^{flox/flox}$; nestin-*Cre* mice, as it is the model of our study, and *Atg7*$^{flox/flox}$; nestin-*Cre* mice, by similitude.

The neural-specific conditional knockout mouse models *Atg5*$^{flox/flox}$; nestin-*Cre* (Hara et al., 2006) and *Atg7*$^{flox/flox}$; nestin-*Cre* (Komatsu et al., 2006) are the main evidence of the fundamental role of basal autophagy for the brain physiology as they are conditional knockout for autophagy in neural cells. The expression of Atg5 and Atg7 proteins which are required for initial steps of autophagy, is abolished since the expression of nestin at embryonic day 12.5 (Yang et al., 2000), and autophagy levels decrease in the neural cells until total blockage at E15.5, (Hara et al., 2006).

Both mouse models show growth retardation, progressive motor and behavioural deficits, as limb-clasping reflex and tremor, indicative of neuronal affectation, and their lifespan extends until 28 weeks, approximately. At the cellular level, both transgenic models present ubiquitin-positive inclusion bodies in several regions of the brain, such as the cerebral cortex,

hippocampus, thalamus or the pons, and they are mostly placed inside neurons. Also, in the case of *Atg7*$^{flox/flox}$; nestin-*Cre* mice, it was tested that the degradative activity of the subunits 20s and 26s of the proteasome was equal to control animals, suggesting that autophagy was the only cause of the accumulation of proteins and that it was mostly affecting neurons. *Atg5*$^{flox/flox}$; nestin-*Cre* mice show signs of neurodegeneration as axonal swelling in several brain regions, loss of pyramidal cells of the cortex and Purkinje cells in the cerebellum, and TUNEL TUNEL (TdT- mediated dUTP Nick-End Labeling) positive cells in the granular cell layer of the cerebellum. *Atg7*$^{flox/flox}$; nestin-*Cre* mice present, as well, neuronal loss of pyramidal cells of the cortex and hippocampus and TUNEL positive cells in the granular cell layer, but also in the cerebral cortex, which is atrophied, suggesting a slightly more intense degeneration than in *Atg5*$^{flox/flox}$; nestin-*Cre* mice brain.

Another interesting model of neural specific autophagy knockout in mouse is the FIP200$^{flox/flox}$;nestin-*Cre.* FIP200 is a component of the ULK1-Atg13-FIP200 initiation complex, thus, its knockout conditioned to nestin expression, eliminates autophagy in the neural tissue, as in the models described above. These animals present similar characteristics to the previous models as smaller size, reduced survival span, altered limb-clasp reflex, tremor and ataxia. In this case, the main feature at the histological level is cerebellar degeneration with progressive neuronal loss, spongiosis and protein aggregates with ubiquitine in neurons, as well as accumulation of p62 and mitochondria. But besides cerebellum, other regions of the brain also presented spongiosis and ubiquitine positive inclusions (Jung et al., 2009; Liang et al., 2010).

Therefore, these mice models are the clearest demonstration that basal autophagy is necessary for neuron homeostasis and that the lack of the pathway in neural precursor cells is enough to generate the accumulation of inclusion bodies and other typical signs of neurodegeneration.

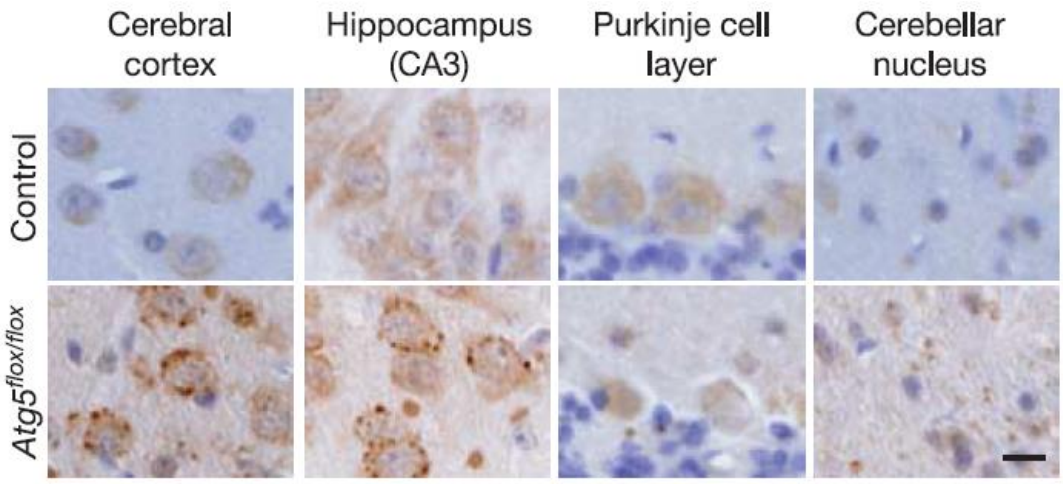

Figure 1.8 Immunohistochemistry for ubiquitine of brain sections from control mice and *Atg5* $^{flox/flox}$; nestin-*Cre*) mice at six weeks of age. Extracted from Hara et al. (2006).

1.3.1.1. The specific case of the retina

The relevance of autophagy for the retinal physiology is still poorly understood. The retina is a tissue more exposed to external agents than the rest of the brain, making it more vulnerable, particularly the photoreceptors, as they develop the light transduction, which is a fast metabolic activity that generates oxidized residues and ROS. The removal of ROS is critical for photoreceptor homeostasis which, in addition to other evidences that will be commented below, suggests that autophagy could play an important role in the maintenance of their homeostasis (Cuenca et al., 2015), besides the relevance *per se* of autophagy for neurons detailed above.

It has been observed that autophagic vacuoles (the authors did not differentiate between autophagosomes or autolysosomes) are concentrated in the inner segment of photoreceptors (IS), where mitochondria, endoplasmic reticulum and Golgi apparatus are placed too (Figure 1.9). It has been suggested that autophagic vacuoles could participate in the elimination of pigments from the discs of the outer segment to regulate light sensitivity of rods according to

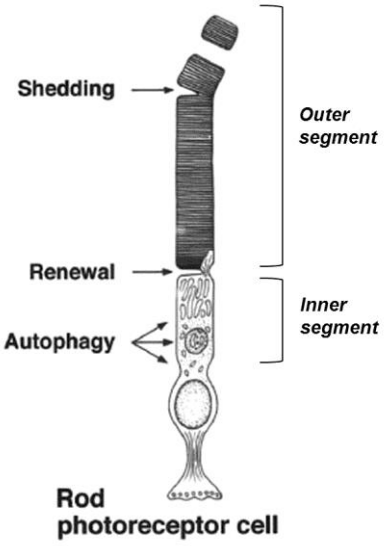

Figure 1.9 Schematic drawing of a photoreceptor cell indicating the main localization of AVs in the inner segment and to a lesser degree in the perinuclear area. It is also indicated the membrane renewal at the OS base and disc shedding from the OS tip. Scheme modified from Reme et al. (1999)

light conditions (Reme et al., 1999). In agreement with this observation, recent findings show that photoreceptors present a circadian modulation of autophagy: AVs formation peaks at 5 hours after shifts between light and dark cycles and it depends on the translocation of transducin and arrestin (intermediaries in the phototransduction process) from the outer to the inner segment of the photoreceptor (Yao et al., 2014). In fact, Zhou et al. (2015) suggesting that autophagy is regulating transducing α and not strictly rhodopsin levels, but still explaining the circadian cycles of autophagy. Further studies from Chen et al. (2013) showed that mouse models Atg7 specific knockout for rod photoreceptors and total body *beclin1* $^{+/-}$ and *Park2*$^{-/-}$ knockout mice presented an increased susceptibility to light-induced retinal damage and to the presence of all trans-retinal, a product of bleaching pigments in photoreceptors that is processed in the RPE during the visual cycle. Interestingly, Kim et al. (2013b), proposed a non-canonical autophagy in the RPE cells with single membrane vesicles coated with LC3-II, and dependent on Atg5 and beclin1 for initiation.

Thus, as the rest of the CNS, in the retina it seems necessary the maintenance of autophagic basal levels for normal physiology, especially for visual cycle, rendering the tissue more susceptible to insults when the pathway is altered, but further research is needed to understand the whole perspective of the participation of autophagy in retinal physiology.

1.3.2. CMA contribution to the CNS homeostasis

CMA contribution to CNS maintenance is barely described for now as there are not mice models deficient of LAMP-2A (which is the restrictive protein for the process) in the total body or specific for CNS or retina. However, the ability of CMA to eliminate proteins no longer required, as transcription factors or enzymes, as well as partially unfolded or oxidized proteins hints a relevant role for the brain homeostasis. In fact, CMA has been described as a regulator of the transcription factor myocyte enhancer factor 2D (MEF2D), required for neuronal survival (Yang et al., 2009). In addition, CMA has been involved in the regulation of HIF-1, which is a transcription factor that regulates hypoxic response (Hubbi et al., 2013). Actually, hypoxia induces CMA activity in neuro-2a cell line and the lack of LAMP-2A renders the cells more sensitive to the stress, leading to cell death. As well, after brain ischemia there is an increase of LAMP-2A too (Dohi et al., 2012). Besides, CMA has been linked to some of the most studied neurodegenerative diseases, as Parkinson's or Alzheimer's disease (Schneider and Cuervo, 2014).

1.3.3. Balance between macroautophagy and chaperone mediated autophagy

Although macroautophagy and CMA present differential characteristics, they share many functional points. It has been observed that they can compensate for each other in certain systems. In mouse fibroblasts, the lack of Atg5 is accompanied by an increase of the CMA activity; and vice versa, the lack of LAMP-2A prompts macroautophagy activity (Massey et al., 2006); (Kaushik et al., 2008). This was further corroborated in a specific LAMP-2A knockout mouse model for liver that also shows an increase of macroautophagy (Schneider et al., 2015).

As both pathways are sequential, for example, in rat liver, macroautophagy peaks after 4-6h of starvation and CMA peak is delayed until 8-10h after starvation. It was thought that maybe some players from the autophagic pathways could regulate the other one. The first candidate was Atg5 as inhibitor of LAMP-2A, which could explain why the lack of Atg5 increases levels of LAMP-2A, but it was not exerting any regulation on CMA. However, it was observed that the absence of macroautophagy itself was favoring the presence of Hsc70 in the lumen of more lysosomes than normal, which is necessary for CMA activity (Kaushik et al., 2008). In any case, whether some molecules are exerting a regulatory effect on the other pathway or whether there are indirect player, it seems that both pathways are able to distribute their functions during the time and also to compensate for each other under the lack of one of them. Further research would enlighten if this mechanism also takes place in the CNS or not.

1.3.4. Neurodegenerative diseases and autophagy: unraveling the relation. Cause or consequence?

During the last years it has been found that some neurodegenerative diseases caused by the accumulation of aberrant proteins also presented impaired autophagy (Frake et al., 2015). For example, Huntington's disease is characterized by the accumulation of the mutant protein huntingtin, prone to aggregate, and it was described in some models that macroautophagy was up-regulated. However, the APs were empty because of an improper recognition of the cargo, impeding the clearance of huntingtin (Martinez-Vicente et al., 2010; Ravikumar et al., 2004). In fact, huntingtin protein was recently related to the formation of APs (Ochaba et al., 2014), to the trafficking of APs, to cargo recognition and to fusion between APs and lysosomes (Martin et al., 2015). Therefore, the mutant huntingtin would impair macroautophagy by direct interference, which in turn worsens the situation, as more huntingtin is accumulated in the cytoplasm. Furthermore, huntingtin is also a CMA substrate, and the mutant form blocks CMA, impeding a compensation of the macroautophagy decline to restore the proteostasis and favouring the accumulation of huntingtin (Koga et al., 2011b).

Another example of neurodegenerative disease with protein aggregates and altered autophagy is Alzheimer's disease, characterized by extracellular deposits of amyloid-β and intracellular deposits of tau. In this case, lysosomes are altered and they cannot fuse with APs, resulting in an accumulation of APs in altered axons (Figure 1.10) (Lee et al., 2010; Lee et al., 2011). Apart from lysosome dysfunction, autophagy can be also carried out in Alzheimer by the mutation of sirtuin 1, an autophagy inducer which is identified as one of the mutations that origin during the disease (Frake et al., 2015). In this pathology, the accumulation of the altered protein amyloid-βdeclines autophagy pathway, which seems to be necessary for the extracellular deposition of amyloid-β, causing the intracellular accumulation of amyloid-β and leading to impaired memory in a mouse model (Nilsson et al., 2013). Besides, tau is substrate for CMA, but the hyperphosphorylated form is not totally translocated and accumulates in the lysosomal membrane, impeding compensation (Wang et al., 2009).

Hence, both examples reflect how entangled autophagy can be with the triggering and progress of the pathology. It seems that some of the mutations found in these diseases directly participate in the autophagic pathway, declining its activity and; on the other hand, the aggregates of the mutant proteins block autophagy, which in turn, impedes the protein clearance. However, in these cases the induction of autophagy decreases the accumulation of aggregates (Ghavami et al., 2014; Tian et al., 2011; Vingtdeux et al., 2011). This arises the doubt of whether the disease is initiated because of a decline in the autophagic pathway at a point, and thus, the mutated protein would accumulate because of the impaired clearance; or whether, on the contrary, the presence of mutant proteins would block the autophagic pathway;or if it is a mixture of both (Frake et al., 2015).

1.3.4.1. Neurodegenerative diseases and autophagy in the retina

Although many studies are focused on neurodegenerative diseases and their relation with autophagy in the brain, few have been performed in the retina yet. For example, the mentioned Alzheimer and Huntington's diseases have being related with functional and morphological alterations of the retina in patients and mouse models, but autophagy has not been analysed here (Krantic and Torriglia, 2014; Paulus et al., 1993; Ragauskas et al., 2014). However, some of the common retinopathies have been linked to altered autophagy, even if it is not clear that autophagic impairment could be among the causes.

For instance, glaucoma, the second leading cause of blindness worldwide, is characterized by optic nerve damage and it has been related to ROS enhancement and secondary accumulation of APs and lysosomeswhich presented reduced enzymatic activity (Boya, 2012). Our group has characterized in an acute model for glaucoma that autophagy has a protective role. The model consists of the axotomy of the optic nerve, inducing the death of RGCs, and it showed a peak of autophagy right before the peak of cell death (Figure 1.11). In addition, blocking autophagy genetically or pharmacologically contributed to increase cell death and, on the contrary, rapamycin treatment resulted protective for RGCs (Rodriguez-Muela et al., 2012)

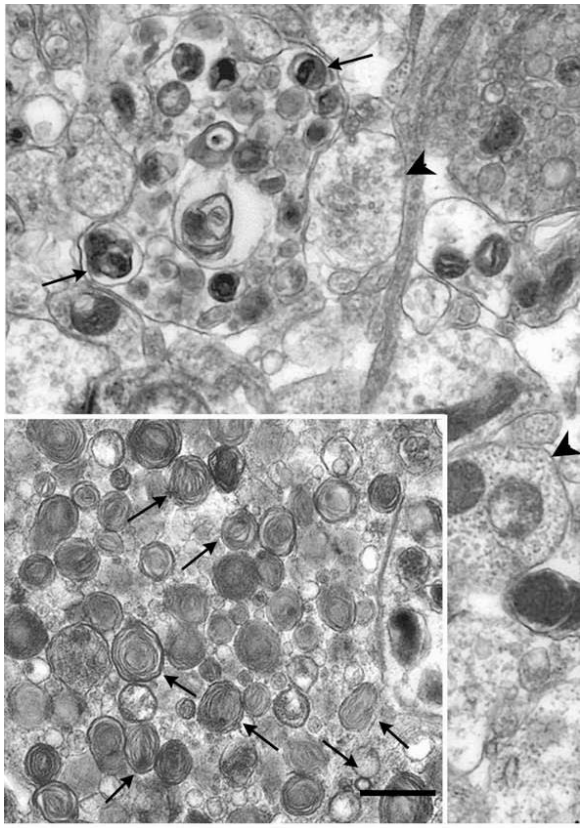

Figure 1.10 Electron microscopy imaging of Alzheimer disease brain samples showing different dystrophic neurites containing distinct AV populations. Abnormal neurites (long arrows), interspersed among normal-appearing neurites (arrowheads), often differ in the predominating AV subtype present and contain AVs of a specific morphologic type. Modified from Nixon et al. (2005)

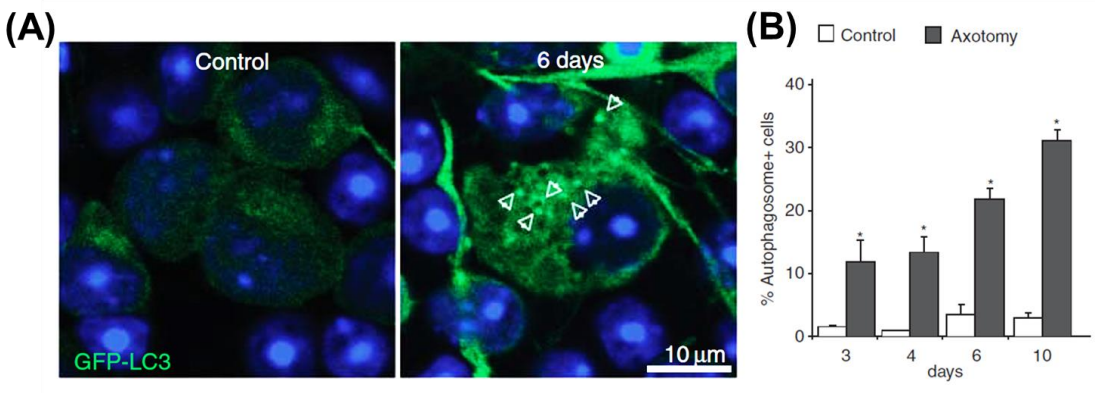

Figure 1.11 Autophagy in glaucoma model of axotomy extracted from (Rodriguez-Muela et al., 2012). (A) Magnification of RGCs in a control retina and 6 days after axotomy. Cells from control retinas display a diffuse and homogeneous green fluorescence of GFP-LC3 in the cytosol, whereas the axotomized RGCs, in the right panel, show visible GFP-LC3 dots identified as autophagosomes and pointed with arrowheads. (B) Quantification of the percentage of cells with GFP-LC3 positive APs in the cytosol versus total number of cells in the GCL in control and axotomiced mice at 3, 4, 6 and 10 days post operation. Modified from Rodriguez-Muela et al. (2012).

Another common retinal disease is AMD, the major cause of visual dysfunction among elder people, and it is also related with ROS and impaired autophagy. It is defined by alterations of choroid, RPE and photoreceptors and the presence of drusen (lipo-proteic deposits) on the edge between RPE and photoreceptors OS, and its onset is related to ROS (Cuenca et al., 2015). Lately, it has been found that RPE cells from AMD patients present reduced autophagic flux and that *in vitro* autophagy induction reduced the cellular damage (Mitter et al., 2014). They also show *in vitro* that acute ROS treatment increases autophagy but chronic exposure declines autophagic activity, suggesting that ROS could impair autophagic flux which, in turn, would lead to the accumulation of oxidized proteins and deteriorate the cellular state.

In addition, recently, our group has described that a mouse model for retinitis pigmentosa presented decreased autophagic flux. Retinitis pigmentosa is a group of inherited mutations that lead to photoreceptor cell death and that has been linked to altered anti-oxidant status (Martinez-Fernandez de la Camara et al., 2013). In the rd10 mouse model we have observed that there is a blockage of the autophagic flux previous to the cell death peak and, in addition, that rapamycin treatment decreased cell survival. Moreover, these animals presented enriched presence of lysosomal enzymes in the cytoplasm, hinting lysosomal permeabilization, which would explain lysosomal dysfunction and autophagy decline previous to cell death (Rodriguez-Muela et al., 2015). Interestingly, there has been also described in four models of retinitis pigmentosa an increase of LAMP-2A in cones, during degeneration, indicating a possible role of compensation by CMA in this disease (Punzo et al., 2009).

All these three examples show alterations of the retina at different points that lead to tissue degeneration and loss of function, and all of them are linked to ROS imbalance and decline of autophagy, suggesting that ROS would be among the main risk factors for the retina

degeneration, and that autophagy modulation at certain stages could ameliorate the progression of the disease by protecting the neurons. Furthermore, the role of CMA seems promising and further research needs to be done to decipher it.

1.3.5. Aging and autophagy

The examples presented here for neurodegeneration in brain and in the retina commonly are multicausal, with a non-defined trigger but many environmental risk factors. Nonetheless, they clearly share one factor: increasing age (Cuenca et al., 2015; Przedborski et al., 2003a).

Lopez-Otin et al. (2013) have defined aging as the loss of physiological integrity, which comes along with impaired function and increased vulnerability to death, and they have delimited some hallmarks of aging. Two of them are clearly related to autophagy: loss of proteostasis and mitochondrial dysfunction. The loss of proteostasis is due to the functional decline of autophagy, both macroautophagy and CMA (Cuervo and Wong, 2014; Rubinsztein et al., 2011) and of the proteasome (Tomaru et al., 2012). Accordingly, the mitochondrial dysfunction, added to autophagic decline, renders the cell exposed to the excess of ROS that is especially harmful to neurons as detailed above (Terman et al., 2010). A common manifestation of ROS excess is lipofuscin, a heterogeneous mixture of oxidized lipids and proteins resistant to hydrolysis that accumulate in the lysosomal lumen. It alters lysosomal functionality, which in turn would impact on autophagy pathways (Terman et al., 2010).

A great example of the decline of autophagy degradation by age is shown by Schneider et al. (2015) in liver knockout for LAMP-2A at different ages. Young animals lacking CMA in the liver can compensate the proteostasis with other mechanisms, even if the organ is more sensitive to challenges. However old animals loss their proteostasis without CMA because there is not enough compensation.

Therefore, the impairment of the autophagic pathways with age would contribute to the onset of age-related pathologies like neurodegeneration. Actually, the induction of autophagy by different strategies reduces the incidence of age-related pathologies and extends life-span in models from yeast to mammals (even primates), remarking the relevance of autophagy for cell homeostasis, particularly in neurons (Frake et al., 2015).

1.3.5.1. Aged retina and autophagy

Pervious data from our laboratory has shown that aged retina presents neurodegenerative features as well as impaired autophagy (Rodríguez-Muela, 2011). In accordance, it has been described a declined rod function (Kolesnikov et al., 2010a).

Our data show that mouse retina presents losses of neurons in all layers at 22 months,glia activation and dystrophic vessels in the INL and GCL. The autophagic flux in aged retinas is reduced but not totally blocked (Figure 1.12) with accumulation of p62 and ubiquitin. However, Experiments with pulse and chase have demonstrated that the proteolytic ability is higher in retinas of aged mice than in those of young mice. Also, proteostasis of young retinas relies

mainly on the proteasome, but in aged retinas it depends on lysosomal pathways. These results were puzzling and indicative of another lysosomal pathway than macroautophagy that should be up-regulated.

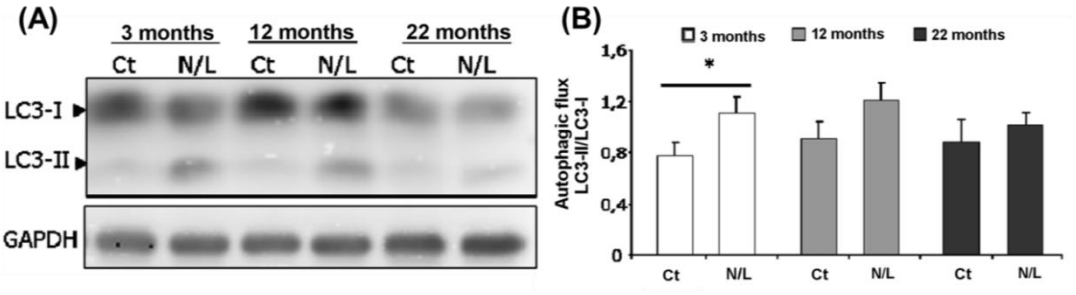

Figure 1.12.(A) Western blot of LC3 forms I and II in C57/Bl6 mice retinas at 3, 12 and 22 months cultured for 4h in the presence (Ct) and absence of lysosomal inhibitors (N/L). (B) Autophagic flux quantification determined by the ratio between the quantification of LC3-II and that of LC3-I. Extracted from Rodríguez-Muela (2011).

1.4. CURRENT METHODS FOR MONITORING AUTOPHAGY AND INTERPRETATION

The approaches to study autophagy and the interpretation of the data have evolved since its discovery by electron microscopy in the 1960s, facing the challenge that autophagy is a dynamic process. The most common techniques and their interpretation are detailed bellow.

1.4.1. Transmission electron microscopy

Autophagy was discovered thanks to transmission electron microscopy as vesicles with diverse content and linked to lysosomes. Nowadays, we can distinguish two kind of vesicles related to autophagy: autophagosomes and autophagolysosomes (Figure 1.2). Autophagosomes appear as double membrane subcellular structures containing undigested cytoplasmic content, as they have not been fused with lysosomes. Frequently, organelles as mitochondria or endoplasmic reticulum are visible in their interior. Sometimes they are difficult to identify as they can be mistaken as mitochondria because of the double membrane. Autophagolysosomes are even more complicated to identify as they present only one membrane and the content is only distinguishable in early stages after fusion, because later it is degraded into an electron-dense mass, which makes it difficult to differentiate autophagolysosomes from other vesicles, such as lysosomes (Mizushima et al., 2010). Figure 1.13 shows a representation of both autophagosomes and autophagolysosomes at different stages.

Electron microscopy is a powerful tool to locate autophagosomes, to observe some irregularities and could be also used to identify substrates in the lumen, even though it is a very tedious task. However, electron microscopy is not suitable for autophagy quantification by itself as it is a static method, it provides a small area of study, and besides it is an expensive and time-

consuming technique. Therefore, it is only recommended to support quantifications performed by other techniques.

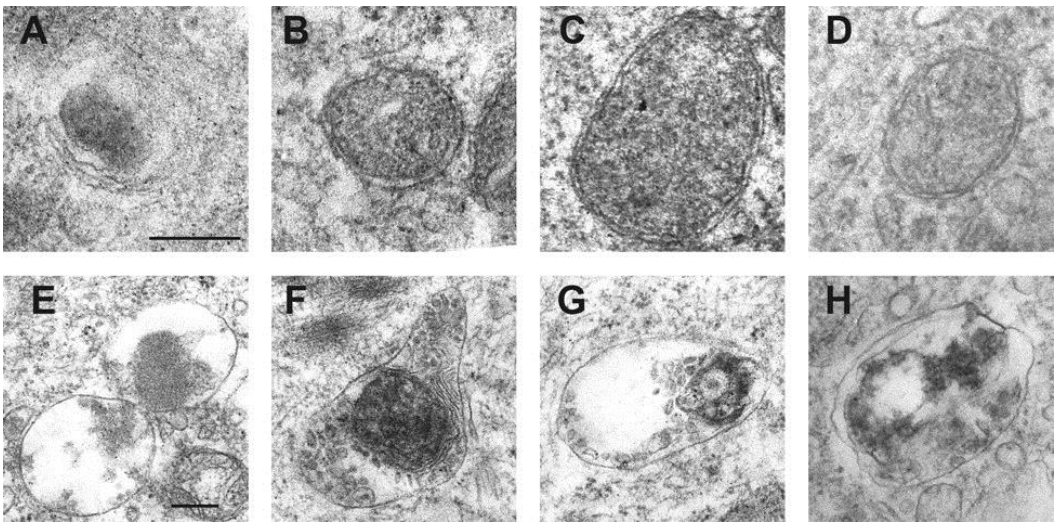

Figure 1.13 Electron microscopy images of autophagic vesicles in different stages. (A) Possible phagophore enclosing the cargo material, (B-D) Autophagosomes delimited by double membrane, (E-H) Autophagolysosomes delimited by one membrane with cargo in different stages of digestion. The bar in panel A represents 200 nM for panels A to D, and the bar in E represents 200 nM for panels E to H. Figure extracted from McFarlane et al. (2011)

1.4.2. Fluorescence microscopy

LC3 is the marker per excellence of autophagy as it is attached to autophagic vesicles. For visualizing LC3 with fluorescence, the frequent methods are LC3 immunostaining and GFP-LC3 overexpression.

GFP-LC3 transfected models present the advantage that both forms of LC3 (LC3-I and -II) are tagged with GFP, avoiding problems with antibodies labelling. Thus, cells present a diffuse cytoplasmic pattern with few puncta that turns into a clear punctate pattern when autophagy is induced (Figure 1.14) (Mizushima et al., 2010). For immunostaining detection, all antibodies detect both LC3-I and II, but LC3-II shows a punctate pattern which clearly differs from the diffused cytosolic pattern to LC3-I.

These APs imaging techniques are qualitative, but that can become quantitative with the measurement methods detailed in the results section. For that, some precautions need to be taken: a uniform approach needs to be established both for the definition of puncta (LC3 dots) and the quantification method, and it is highly recommendable to use software for detection and quantification, as visual/manual quantification is possible but quite susceptible of subjectivity (Mizushima et al., 2010).

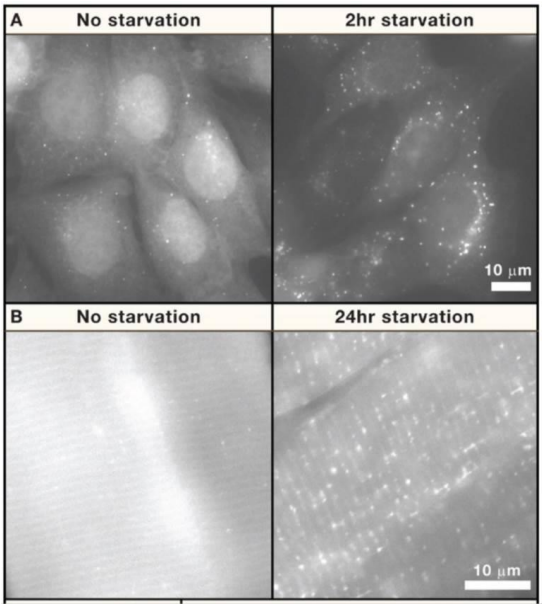

Figure 1.14 Fluorescence imaging of GFP-LC3 stably transfected systems. (A) NIH 3T3 cells in control culture (left) and after 2h of starvation (depletion of both amino acids and serum); (B) Skeletal muscle sample of mice in control conditions and after 24h of starvation. In both cases is perceptible the change of pattern from cytosolic diffused GFP to punctate. Extracted from Mizushima et al. (2010).

The quantification can be performed by three estimation ways:

a) *Percentage of LC3 positive cells*: it is suitable for a visual counting but it is not "strictly true" as in theory all cells present autophagosomes. In case of performing this quantification, a clear threshold to define "autophagy active cells" is necessary.

b) *Total area of LC3 per cell*: can be performed by software for imaging treatment. It is necessary to rule out artefacts.

c) *Average of LC3 puncta per cell*: this method can be performed with image analysis programs (for example, Top Hat algorithm of MetaMorph version 7.0 by Molecular Devices, and G-Count by G-Angstrom).

As the autophagic-lysosomal pathway is characteristic by a series of fusions, the quantification of puncta per cell and the estimation of the volume of the vesicles are complementary to understand the autophagic state of the studied model, which is basically defined by the autophagic flux (see below) (Klionsky et al., 2007; Mizushima et al., 2010).

1.4.3. Biochemical assays

Another common method to estimate the levels of autophagy in a system is by western blotting LC3, a semi-quantitative technique. A good point of this method is that it allows following and quantifying the conversion of LC3-I in LC3-II, as they present a different molecular weight. LC3-I appears at 16kDa and LC3-II, even if it is larger, migrates to 14 kDa, because of the hydrophobicity conferred by phospatidylethanolamine (Mizushima et al., 2010). Figure 1.15 shows an example of both proteins.

The three methods detailed above (*electron microscopy, fluorescence detection and biochemical assays*) provide an estimation of the activity of autophagy but only fluorescence can be transformed into a quantitative technique. Thus, in order to obtain a proper conclusion

from the experimental data, it is preferable to use more than one technique. Especially electron microscopy is not recommendable for wide quantification, but for supporting of other data. Furthermore, these methods offer a static measurement of a dynamic process, which is not conclusive about the autophagic state of the model. However, we can use them for autophagy flux monitoring (see below).

1.4.4. Autophagy flux monitoring

As mentioned, autophagy is a dynamic process that involves the formation of AVs and their fusion with lysosomes for degradation. Thus, a punctual measurement of the number of autophagosomes or quantification of LC3-II is not revealing much information by itself. To fully understand the autophagic state of a system it is necessary to compare the number of autophagosomes/quantity of LC3-II in a studied condition (we can call it "basal condition") and in the addition of lysosomal inhibitors (adding them to the culture medium, treating the mice or as appropriate), so autophagosomes will not fuse with lysosomes. Blocking the maturation of autophagosomes but not their synthesis, we can observe, in the time window of our treatment, the accumulation of the autophagosomes/quantity of LC3-II generated during this time. The difference between the quantification with lysosomal inhibitors and the basal state is called autophagic flux. Once we know the autophagic flux of a system we can compare it with other systems or conditions.

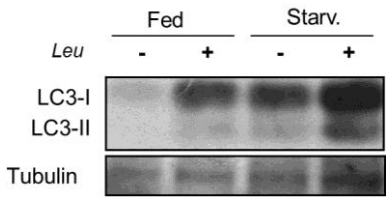

Figure 1.15. Example of western blot detection of LC3 I and II in the presence and absence of leupeptin as lysosomal inhibitors (leu). LC3 I and II are separated by 2 kDa of difference. There is clear the accumulation of LC3 II in the presence of lysosomal inhibitors, even greater in starvation conditions. The samples are retinas of fed and starved mice at postnatal day 20 cultured for 6h with leupeptine.

Figure 1.15 shows an example of LC3-I and II detection by western blot in the presence and absence of the lysosomal inhibitor leupeptin in mouse retina samples of control and starved animals. We can clearly appreciate the accumulation of LC3-II in the presence of leupeptin compared with the initial state without it, especially after starvation, which means that the autophagic flux is higher after starvation than in fed conditions.

On the contrary, if the samples were measured after a treatment with an autophagy inhibitor (detailed in the next section), the autophagic flux would be quite reduced compared to fed/control conditions.

Besides LC3, other proteins related with the process can be used to follow the autophagic flow. For example, p62 and ubiquitin are common indicators of autophagy blockage, as they tag proteins for lysosomal degradation and they accumulate when clearance pathways are interrupted.

1.4.5. Drug modulators of autophagy

Autophagy modulators, both inhibitors and inducers, are notably important to study the autophagic response of a system (Mizushima et al., 2010). They allow us to study the autophagic flux of a system through its capacity of response to modulations. Genetic modulation is also a desirable tool when studying a system but it is difficult to achieve in primary cells, tissues or animals. Figure 1.20 shows a scheme of the main modulators of autophagy both chemical and genetic, and we will detail the pharmacological ones bellow.

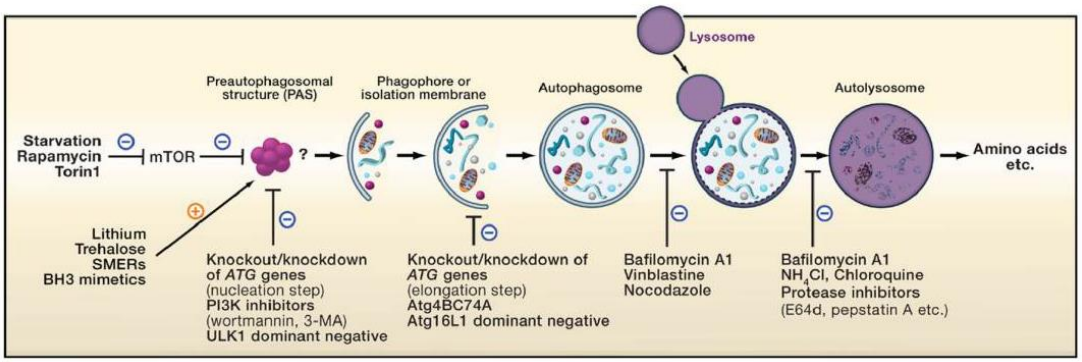

Figure 1.16 Scheme of the target stages of the major modulators of the autophagic process. Modified from Mizushima et al. (2010).

Inhibitors can work at two points: early and late stages (Mizushima et al., 2010). *Inhibitors of early stages* prevent the formation of autophagosomes by inhibiting the activity of PI3K class III. Some examples are 3-methyladenine, LY 294002 or wortmannin. *Inhibitors of late stages* block the fusion of autophagosomes with the lysosomes or prevent the degradation of the cargo, by altering the pH of the lysosomes (ammonium chloride, chloroquine, bafilomycin A1) or by inhibiting their proteases (leupeptin, E64D, pepstatin A). These inhibitors are used to study autophagic flux. It is also recommendable if possible the genetic inhibition of autophagy, as drugs can always have side effects (Mizushima et al., 2010; Vakifahmetoglu-Norberg et al., 2015).

The most potent known physiological **inducer** *in vivo* and *in vitro* is starvation, mainly of amino acids but also of growth factors withdrawal (Mizushima et al., 2010). Autophagy can also be modulated pharmacologically. Most of the inducers target mTOR, by supressing its activity, such as rapamycin and analogues and other compounds more specific as Torin1. As mTOR is a keystone of metabolism, mTOR-independent inducers, as trehalose, are recommendable to better understand the effect, for instance (Kim and Guan, 2015; Mizushima et al., 2010).

1.5. CELL DEATH: APOPTOSIS AND CURRENT METHODS OF DETECTION

Through the evolution, cells have developed a range of mechanisms that lead to cell death in response to a great variety of potentially lethal insults. Cell death pathways are traditionally defined by their morphology and molecular effectors (Lalaoui et al., 2015). The typical cell death

pathways are apoptosis and necrosis, although recently other types and classifications have emerged (Galluzzi et al., 2015; Kroemer et al., 2009).

Apoptosis is morphologically defined by the following features: rounding up of the cell and shrinkage, chromatin condensation, nucleus fragmentation (karyorrhexis), exposure of phosphatidylserine and shedding of apoptotic bodies (vacuoles containing cytoplasm and intact organelles) (Galluzzi et al., 2015; Kroemer et al., 2009). On the other hand, necrotic cells present organelles swelling (as endoplasmic reticulum or mitochondria), nucleus distension, plasma membrane rupture and the lysis of the cell. At the molecular level the difference between apoptosis and necrosis relies on the orchestrated fate of apoptosis directed by caspases versus a "purely accidental event" that necrosis was considered, but this simplistic classification is under review nowadays (Galluzzi et al., 2015).

Autophagy used to be considered a cell death type too, however nowadays autophagic cell death is a term that only describes that autophagy happens in parallel with cell death, but not that it is the executer (Kroemer et al., 2009).

Several methods have been developed to detect these mechanisms based on their differences. Here we will focus on some of the most characteristic ones by imaging detection and quantification.

1.4.5. Current methods for apoptosis detection by imaging

Apoptosis is a well-studied phenomenon and thus it presents a plethora of assays for its detection. Here we will only focus on some of the most common imaging, quantitative and also differential methods based on Kroemer et al. (2009).

1. Cytomorphic alterations by electron microscopy

Transmission electron microscopy allows the visualization of ultrastructural modifications as gaps in plasma or mitochondrial membrane, mitochondrial swelling or the first phases of chromatin condensation. However, it is an expensive and time-consuming technique that only provides a small area of study and, thus it should be complemented with other quantitative methods.

2. Nuclear condensation

Nuclear condensation can be easily appreciated by nuclear staining with DAPI or Hoescht. Those are easy techniques that provide great information for quantification of apoptotic cell death.

3. DNA fragmentation

A classical approach for detecting DNA fragmentation is TUNEL staining, which presents higher sensitivity than most other cytochemical method. It consists in the addition of labelled nucleotides to the DNA fragmented strains by the terminal deoxynucleotidyl transferase (Tdt).

3. Caspases detection

Caspases, as well as their substrates, regulators or inhibitors can be labelled by several methods, but a highly effecient one is immunocytochemistry. It allows us to follow apoptosis at different steps of the caspase cascade with different primary antibodies.

4. Membrane alteration

During apoptosis, phosphatidylserine is exposed to the external face of the plasma membrane, which allows for the detection via Annexin V labelled with FITC. Usually this technique is used for cytofluorometry and luminometry but it can also be applied to visual analysis.

2. OBJECTIVES

2. OBJECTIVES

The main objective of this thesis is to determine the consequences for retinal homeostasis of deleting and the essential autophagy regulator Atg5 in neuronal precursors and compare this phenotype with changes observed in aged retinas. Moreover, and to generalize our findings we have evaluated the consequences of autophagy down-regulation in the cerebellum and compared the phenotype with that found in the retina.

In particular, the concrete objectives were to:

1. Study the functionality retina retinal function of *Atg5* $^{flox/flox}$; nestin-*Cre* mice.

2. Study the morphology of the retina of *Atg5* $^{flox/flox}$; nestin-*Cre* mice.

3. Determine the response of the macroglia in the retina of *Atg5* $^{flox/flox}$; nestin-*Cre* mice and aged mice retina.

4. Evaluate the proteostasis state of the retina of *Atg5* $^{flox/flox}$; nestin-*Cre* mice and aged mice retina.

5. Assess whether there could be the existence of a compensation mechanism from chaperone mediated autophagy in the retina of *Atg5* $^{flox/flox}$; nestin-*Cre* mice and aged mice retina.

Moreover and based on the results, we decided to study another brain region, the cerebellum. By comparing both areas we to check if they were extrapolable or they were a particularity of the retina. For that end, we stablish another objective:

6. Study proteostasis and the levels of CMA proteins in cerebellum of *Atg5* $^{flox/flox}$; nestin-*Cre* mice.

7. In parallel, in collaboration with the Wimasis company, we collaborated in the development of two new tools for automatized imaging analysis of autophagy and apoptosis assays as potential tools for neurodegeneration studies.

3. MATERIALS AND METHODS

3. MATERIALS AND METHODS

3.1. Cell lines

3.1.1. Cell lines and culture conditions

The cone photoreceptor 661W murine cell line (Tan et al., 2004) was provided by Dr Muayyad Al-Ubaidi (Department of Cell Biology, University of Oklahoma Health Sciences Center, OK, USA). Bax/Bak double knockout and wild-type MEFs (murine embryonic fibroblasts) were kindly provided by Aviva Tolkovsky (John van Geest Centre for Brain Repair, Cambrige, UK). HeLa cells were purchased from the ATCC.

Cells were cultured at 125 cell/mm^2 cell density in Dulbecco's modified Eagle's medium (DMEM) supplemented with 10% inactivated fetal bovine serum and 2 mM glutamine at 37 °C in an incubator with a 5% CO_2 atmosphere.

For autophagy induction, serum starvation was performed by thoroughly washing the cells with phosphate buffered saline (PBS) and placing them in serum-free complete DMEM. Also culture with rapamycin 100 nM was used.

For autophagic flux blockage, cells were treated by adding leupeptin 100 µM (Thermo Fisher Scientific, MA, USA) and 20 mM ammonium chloride (Sigma-Aldrich) to the culture medium, in order to inhibit the lysosomal activity. Leupeptin is a reversible inhibitor of trypsin-like and cysteine proteases. Ammonium chloride basifies the pH of the lysosomes, decreasing the activity of the lysosomal enzymes. Also hydroxychloroquine (HCQ) was used in other experiments, adding the compound for the last three hours at 30mg/mL.

For apoptosis induction, cells were treated with staurosporin (StS) at 500 nM for 16 h. For oxidative stress induction, paraquat (PQ) was used in culture at 1 mM for 24h.

3.1.2. Cell lines stable transfection

Previously in the laboratory, 661W LAMP-2A and Atg7 knockdown cells were generated with lentiviruses. Those were obtained in HEK203T cells, by culturing the cells in the presence of a mixture of the following plasmids: viral cap plasmid (pMD2.VSVG), packaging plasmid (pMDLg/pRRE), viral replication proteins plasmid (pRSV-Rev) and siRNA sequences carrier plasmid (pLVTHM). Transfection was mediated by calcium phosphate, as described by Mailand et al. (2002).

The silenced regions were for the gene *LAMP-2A*: 5´-GACTGCAGTGCAGATGAAG-3´, 5´-CTGCAATCTGATTGATTA-3´, and 5´-TAAACACTGCTTGACCACC-3´, corresponding to bases 1198–1216, 1331–1359, and 1678–1700. For the gene *atg7*: 5´- GCAGCTCATTGATAACCAT-3´.

The obtained supernatant with the lentiviruses was added to the 661W cells, in confluence, in presence of polybrene, a transduction enhancer. As the plasmid was coupled to a GFP reporter, once obtained a good level of transfection, cells were sorted by flow cytometry (FACS Vantage, Becton Dickinson, New Jersey, USA), to select the transfected cells. Also, control cells were transfected with a nonsilencing lentiviral vector expressing the unrelated protein phosphoglycerate kinase (PGK) coupled to GFP to correct for the effects of lentiviral infection, as previously described Singh et al. (2009).

To determine CMA activity pKFERQ-PA-mCherry1 plasmid construction, a CMA photoconvertible fluorescent reporter (Koga et al., 2011b) was transfected into 661W cells using the same transfection technique.

3.2. Animal experimentation

All animal procedures were approved by the local ethics committee for animal experimentation, under animal study protocols approved by the CSIC and were carried out in accordance with the European Union guidelines. Animals of either sex were used for this study. Mice were maintained on a 12-h light/dark cycle in a temperature-controlled barrier facility, with free access to water and food.

C57BL/6J aged mice were obtained from The Jackson Laboratory (Bar Harbor, ME) and a breeding colony was established at the animal facility at the Centro de Investigaciones Biológicas (CIB-CSIC). Aged animals were used at 12 and 23 months of age, with control animals at 3 months of age.

Atg5$^{flox/flox}$ mice, a mice model, described by Hara et al. (2006), were kindly provided by Noboru Mizushima (Tokyo Medical and Dental University, Japan). Nestin-*Cre* mice were provided by Marcos Malumbres (CNIO, Spain). Control animals are considered *Atg5*$^{flox/flox}$; nestin-*Cre* the *Atg5*$^{flox/flox}$ and the *Atg5*$^{+/flox}$ as described in Hara et al., 2006. *Atg5*$^{flox/flox}$; nestin-*Cre* mice present the depletion of *Atg5* gene (a key regulator of the autophagy pathway) in neural cells under the promoter of nestin (Figure. 3.1), active in the whole brain at E15.5, which leads to mice with progressive motor deficits, accumulation of cytoplasmic inclusion bodies in neurons and short lifespan (2-3 months), as described in the introduction.

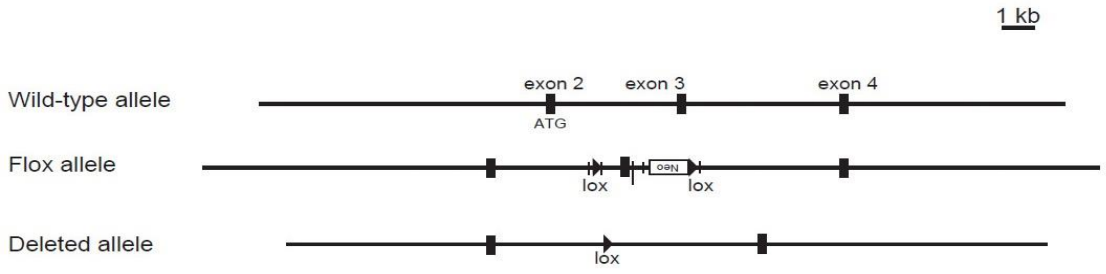

Figure 3.1. Scheme of the wild-type *Atg5 allele,* the flox allele, and the deleted allele after Cre-mediated recombination. Black boxes indicate exons 2-4. Modified from Hara et al. (2006).

GFP-LC3 mice were also were kindly provided by Noboru Mizushima (Tokyo Medical and Dental University, Japan). This mouse model presents a genomic insertion of a construct with the light chain 3 gene (LC3) linked to the green fluorescent protein (GFP) under a constitutive promoter (Mizushima et al., 2004). Therefore, LC3 is overexpressed and can be detect under a fluorescence microscope. In any case, the overexpression does not affect the endogenous production of LC3, neither the mice present any overt phenotype.

3.2.1. Mouse colonies genotyping and phenotyping

3.2.1.1. *Atg5* $^{flox/flox}$; nestin-*Cre* genotyping and phenotyping

To determine the presence of the *Atg5*$^{flox/flox}$ gene two pairs of primers were used, as described by Hara (Hara *et al*., 2006):

- Primers for Atg5 wt: A- 5´-GAATATGAAGGCACACCCCTGAAATG-3´, B- 5´ GTACTGCATAATGGTTTAACTCTTGC-3´
- Primers for Atg5$^{flox/flox}$: C-5´-ACAACGTCGAGCACAGCTGCGCAAGG-3´, D- 5´-CAGGGAATGGTGTCTCCCAC-3´

To determine the presence of the nestin-*Cre* gene we used the pairs of primers described by Hara et al.:

- cre1: 50-AGGTTCGTTCACTCATGGA-30
- cre2: 50 -TCGACCAGTTTAGTTACCC-30

For the PCR reaction we used 1 µL of genomic DNA in a final volume of 25 µL and the Master Mix© (5 PRIME) kit. The conditions for the reaction were as follows: 1 cycle at 95ºC 2 minutes, 35 cycles of 30 seconds at 95ºC, 50 seconds at 60ºC and 1 minute at 72ºC each cycle, 1 cycle at 72ºC 10 minutes. Figure 3.2 shows an example of the bands obtained for each gene and the allelic variations.

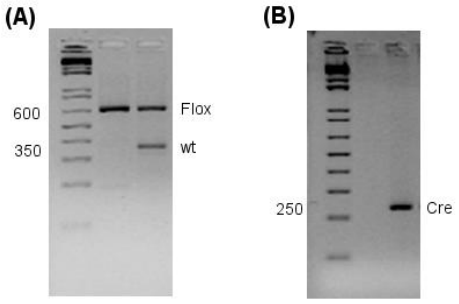

Figure 3.2. Example of genotyping for (A) Flox of 600bp and wild-type of 350 bp alleles and for (B) Cre allele of 250 bp. Left lane in both panels shows the DNA ladder of 100 bp each step.

The genotype was also confirmed with phenotype. As described by Hara et al. (2006), the KO animals present an abnormal limb-clasping when suspended by the tail (Figure 3.3) as well as tremor in most of the cases and a smaller size.

Figure 3.3. Limb related behavior shown by control and Atg5 $^{flox/flox}$; nestin-*Cre* when suspended by the tail. Atg5 $^{flox/flox}$; nestin-*Cre* show limb clasping reflexes not observed in control animals. Extracted from Hara *et al*., 2006.

3.2.1.2. GFP-LC3 genotyping and phenotyping

GFP-LC3 mice were genotyped until the establishment of the colony in homozygosis. Once it was stable, the animals were only phenotyped. For phenotyping these animals, a small piece of the tail was observed under an epifluorescence microscope with 488 wavelength light. The recognition of GFP-LC3 positive animals was quite clear as they always present strongly green fluorescence in comparison to wild-type animals (Figure 3.4).

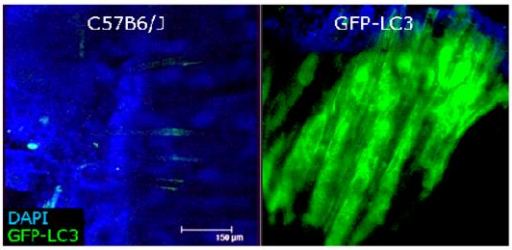

Figure 3.4. Phenotype of wild-type and GFP-LC3 mice. Tails of both strains stained with DAPI and illuminated with a 488 wave length light. Only GFP-LC3 animals present green fluorescence.

3.3. Evaluation of retinal function by electroretinogram (ERG)

ERG experiments were performed in collaboration with Pedro de la Villa (Department of Physiology, Universidad de Alcalá, (Alcalá de Henares, Spain). 6 week-old *Atg5* $^{flox/flox}$; nestin-*Cre* mice and their control littermates were subjected to the experiment. Mice were dark adapted overnight and subsequent manipulations were performed in dim red light. Mice were anesthetized with intraperitoneal injections of ketamine (95 mg/Kg of body weight) and xylazine (5 mg/Kg of body weight) solution and maintained on a heating pad at 37°C. Pupils were dilated with a drop of 1% tropicamide (Colircusıi Tropicamida; Alcon Cusi, Barcelona, Spain). To optimize electrical recording, a topical drop (2% Methocel; Hetlingen, Switzerland) was instilled on each eye immediately before situating the corneal electrode.

Flash-induced ERG responses were recorded from the right eye in response to light stimuli produced with a Ganzfeld stimulator. Light intensity was measured with a photometer at the level of the eye (Mavo Monitor USB; Nuremberg, Germany).

Four to 64 consecutive stimuli were averaged with an interval between light flashes in scotopic conditions of 10 s for dim flashes and of up to 60 s for the highest intensity. Under photopic conditions, the interval between light flashes was fixed at 1 s.

ERG signals were amplified and band-filtered between 0.3 and 1000 Hz with an amplifier (CP511 AC amplifier; Grass Instruments, Quincy, MA, USA). Electrical signals were digitized at 20 kHz with a power laboratory data acquisition board (AD Instruments, Chalgrove, UK). Bipolar recording was performed between an electrode fixed on a corneal lens (Burian-Allen electrode; Hansen Ophthalmic Development Laboratory, Coralville, IA, USA) and a reference electrode located in the mouth, with a ground electrode located in the tail.

Under dark adaptation, scotopic threshold responses (STR) were recorded to light flashes of - 4 log cd·s·m^{-2}; rod responses were recorded to light flashes of -2 cd·s·m^{-2}, and mixed responses were recorded in response to light flashes of 1.5 cd·s·m^{-2}. Oscillatory potential (OP) was isolated using white flashes of 1.5 log cd·s·m^{-2}in a recording frequency range of 100–10 000 Hz. Under light adaptation, cone-mediated responses to light flashes of 2 log cd·s·m^{-2} on a rod-saturating background of 30 cd·m^{-2}were recorded. Wave amplitudes of the STR, rod responses (b-scotopic), mixed responses (a-mixed and b-mixed), and OP were measured off line by an observer masked to the experimental condition of the animal.

3.4. Retinal extraction and processing

3.4.1. Retina isolation

After killing the mouse, eyes were enucleated and disposed in cold PBS. Under a binocular Leica lens and a pair of thin tweezers, the neural retina was separated from the rest of components of the eye, first from the sclera and pigment epithelium, then from the *ora serrata* and finally, from the lens, as shown in Figure 3.5.

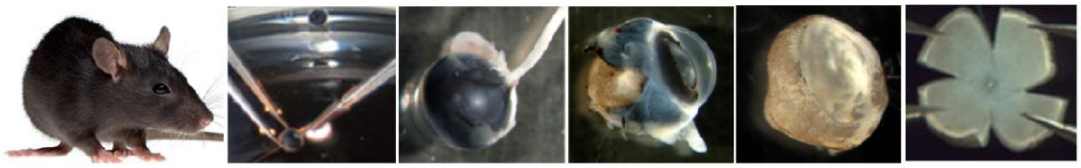

Figure 3.5. Retina extraction and flat-mounting. After eye enucleation, the sclera, pigment epithelium (first four images) and *ora serrata* (fifth image) are removed, then the retina is separated from the crystalline and finally it is flattened on a nitrocellulose membrane (sixth image). Extracted from Rodriguez-Muela, N, 2011.

Extracted retinas were used whether for immediate fixation in PFA 4% (see below flat-mounting of retinas section) or preservation at -80ºC or either culture.

3.4.2. Retinal culture

After isolation, retinas were placed in 24-well plates with 1 mL of R-16 nutrient medium at pH 7.14 without serum (described by (Romijn et al., 1988)) and kept in an incubator at 37ºC with 5% of CO_2 for 24h.

For inducing autophagy, retinas were thoroughly washed with PBS and incubated with Earle´s Balanced Salt Solution (EBSS). To obtain a higher induction, rapamycin was added to the medium at 100 nM (Calbiochem).

For studying the autophagic flux, retinas were cultured with a cocktail of proteases inhibitors (PI) that consisted of E64d 5µg/mL, leupeptin 100 µM and pepstatin A 10 µg/mL (Calbiochem). E64d is a cysteine protease inhibitor, pepstatin A is aspartyl peptidase inhibitor and leupeptin, as mentioned before, is a reversible inhibitor of trypsin-like and cysteine proteases. After the corresponding culture, retinas were either fixed with PFA 4% for 1h RT or immediately frozen at -80ºC.

3.4.3. Flat-mounting of retinas

After the retina extraction or culture, four cuts were performed from the periphery to the center of the retinas to flat them, forming a maltese cross (Figure 3.5). Then, retinas were attached to a piece of black nitrocellulose of 0.44 µm pore (Sartorius, Götingen, Germany) by slightly pressing the edges of the retina against the nitrocellulose.

Retinas were placed with photoreceptors faced to the nitrocellulose for the astrocyte study in Atg5 $^{flox/flox}$; nestin-*Cre* and in the other way around for the GFP-LC3 Wimasis analysis.

Finally, the retinas were fixed 1h at RT in PFA 4% (p/v) in 0.1 M phosphate buffer pH 7.14 and then kept in PBS at 4ºC till staining.

3.4.4. Eyeball cryosectioning

After enucleation, eyes were fixed for 2h in paraformaldehyde (PFA) 4% % (p/v) in 0.1 M phosphate buffer pH 7.14, washed with PBS and kept in PBS with sodium azide 0.001%, until cryosectioning. Before cryosections, samples were cryoprotected by immersion in crescent concentrations of sucrose in PBS: 15%, for at least 24h, and 30%, for the next 48-72h. To immobilize the samples for the slicing process, eyes were immersed in OCT (Tissue Tek, Sakura Finetek, Tokio, Japon) and freezed at -80ºC. Samples were next sliced at 12 µm of thickness with a Leica CM 1800 cryostate and disposed on positively charged glass slides (Superfrost® Plus, Thermo Scientific, Massachusetts,USA). Cryosections were maintained at RT o/n (overnight) and then conserved at -80ºC.

3.5. Cerebellum extraction and processing

3.5.1. Cerebellum extraction

After cervical dislocation of the mice, brains were carefully extracted from the skull with the help of small scissors and tweezers, and then, longitudinally cut into hemispheric sections. The right hemisphere of the brain was designated for immunohistochemistry and was immediately submerged in 4% PFA for fixation during 24h at 4ºC in a shaker. The left hemisphere was designated for protein extraction and was immediately frozen at -80ºC.

3.5.2. Cerebellum cryosectioning

After fixation in PFA, brains were washed with PBS and then cryoprotected by embedding the samples in sucrose at 15% for 2 days and 30% for another 2 days. Once finished the process, samples were immersed in OCT and frozen at -80ºC. Then, they were sliced with the cryostat at 15 µm of thickness, placed in positively charged glass slides and kept at -80ºC for conservation.

3.6. Samples staining and imaging

3.6.1. Immunostaining

3.6.1.1. Immunostaining of cell lines

After a PBS washing, cells where fixed with PFA 4% for 1h, washed again and permeabilized with 0.1 % SDS (sodium dodecyl sulphate) in PBS for 10 minutes. After washing three times, samples are incubated o/n in a humid chamber at 4ºC in the presence of the antibody diluted in 10% NGS (normal goat serum). After a long washing step (1h), samples are incubated in the presence of the secondary antibody conjugated with a fluorophore in BGT buffer (3mg/mL BSA, 10 mM Glycine and 0.25% Triton X-100 in PBS) during 1h at RT in a humid chamber. After another long washing step, the samples are stained with the nuclear marker DAPI (4',6-diamidino-2-phenylindole) at 1 µg/mL (Invitrogen, California, USA), washed again and finally, mounted with Fluoromount-G (Cultek).

3.6.1.2. Immunostaining of retinal cryosections

Frozen samples at -80ºC were tempered first at RT for 10 minutes and then, at 50ºC 30 minutes in a stove. Once dry, samples were rehydrated in PBS and then blocked and permeabilized in BGT buffer for 30 minutes. After washing three times with PBS, samples were incubated o/n in a humid chamber at 4ºC in the presence of the primary antibody mixture diluted in BGT. After three long washing steps (1h), samples were incubated in the presence of the secondary antibody conjugated with a fluorophore in BGT during 1h at RT. After another three long washing steps, the samples were mounted with DABCO with the nuclear staining DAPI at 1 µg/mL.

3.6.1.3. Immunostaining of flat-mounted retinas

Samples were washed three times in PBS and blocked and permeabilized in BGT buffer for 30 minutes. After washing three times, a stronger permeabilization is performed with 1% of triton X-100 for 90 minutes plus another washing step (three times). Then samples were incubated o/n in a humid chamber at 4ºC in the presence of the primary antibody cocktail diluted in BGT. After three long washing steps (1h), samples were incubated with the secondary antibodies mixture in BGT during 2h at RT. After another long washing step, the samples are mounted with DABCO with DAPI at 1 µg/mL.

The image analysis of the retinas was performed in two fields in the central region.

3.6.1.4. Immunostaining of cerebellum cryosections

As samples were stored at -80ºC, they were tempered at RT for 10 minutes and then dried at 50ºC in a stove. Once ready, samples were washed three times in PBS and blocked and permeabilized with a blocking buffer (1% triton X-100, 1% BSA and 3% FBS in PBS) for 2 days at 4ºC. After washing three times, samples are incubated o/n in a humid chamber at 4ºC in the presence of the primary antibody cocktail diluted in the same blocking buffer. After three long washing steps (1h), samples were incubated in the presence of the secondary antibody diluted in the blocking solution during o/n at 4ºC. After another three washing steps, the samples are mounted with DABCO with the nuclear staining DAPI at 1 µg/mL.The analysed areas were the molecular, Purkinje and granular layers.

3.6.1.5. Primary and secondary antibodies for immunofluorescence staining

The proteins detected by immunostaining in the conditions detailed bellow are listed in the Table 3.1 Secondary antibodies are listed in Table 3.2.

Detected protein	Provider	Reference	Specie	Dilution
Caspase-3	Cell Signalling	9662	Rabbit	1:100
LC3 *(Light Chain 3)*	NanoTools	0231-100/LC3-5F10	Mouse	1:250
Lamp2	Invitrogen	51-2200	Rabbit	1:100
Hsc70 *(Heat Shock Cognate)*	Enzo	ADI-SPA-815	Rat	1:100
p62	Progen	GP62-C	Guinea pig	1:100
Calbindin	Sigma	C2724	Rabbit	1:1000
PKCα *(Protein Kinase C α)*	Sigma	P4334	Rabbit	1:100
GFAP *(Glial Fibrillary Acidic Protein)*	DAKO	Z0334	Rabbit	1:500
Cone opsin red and green	Chemicon	AB5405	Rabbit	1:100
Cone opsin blue	Chemicon	AB5407	Rabbit	1:100

Table 3.1. List of the primary antibodies used for the immunostaining procedures commented above, detailing the provider, reference, animal species of obtainment and used dilution.

Type of secondary antibody	Provider	Reference	Specie	Dilution
Alexa 568 anti-mouse	Invitrogen	A11004	Goat	1:2000
Alexa 546 anti- rabbit	Invitrogen	A11011	Goat	1:2000
Alexa 647 anti-rabbit	Invitrogen	A21244	Goat	1:2000
Alexa 568 anti-guinea pig	Invitrogen	A11075	Goat	1:2000
Alexa 647 anti-rat	Invitrogen	A21248	Goat	1:2000

Table 3.2. List of the secondary antibodies used in the immunostaining procedures commented above, detailing the provider, reference, animal species of obtainment and used dilution.

3.6.2. Apoptosis labelling by TUNEL staining (*dead end fluorimetric system)*

The TUNEL staining detects the fragmented DNA of apoptotic cells by incorporating fluorescein-12-dUTP at the 3' -OH ends of the DNA using the enzyme terminal deoxynucleotidyl transferase (recombinant), which forms a polymeric tail using the principle of the TUNEL (TdT- mediated dUTP Nick-End Labeling) assay.

The assay was performed in retinal cryosections. Slides were rehydrated in PBS, permeabilized with 2% triton for 1h and blocked with BGT for 30 minutes. After washing, samples were incubated 15 minutes in equilibration buffer (200 mM potassium cacodylate, 25mM Tris-HCl, pH 6.6, 0.2 mM DTT, 2.5 cobalt chloride, 0.25 mg/mL BSA). Once equilibrated, the samples were incubated 1h at 37ºC with the TUNEL reaction mix (2% rTDT enzyme, 10% nucleotide mix, 88% equilibration buffer). The reaction was stopped with 2x SSC (Salt Sodium Citrate).

3.6.2. Photoconvertible fluorescent reporter to measure chaperone-mediated autophagy activity

The pKFERQ-PA-mCherry1 plasmid construction and the establishment of stable cell lines expressing the CMA reporter was performed using lentiviral transfer vectors as described by (Koga et al., 2011b). The reporter is linked to the KFERQ motif of the proteins that carry it and it get photoactivated under UV light exposure. Thus, for the experiments, photoactivation of the

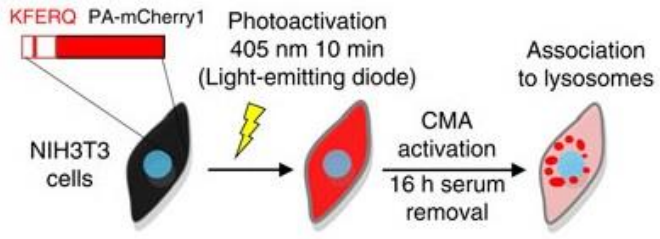

Figure. 3.6. Scheme of the experimental design to monitor CMA activity in cells transfected with pKFERQ-PA-mCherry1 reporter.

reporter was performed on transfected cells grown on coverslips with a 405/20 nm LED array (Norlux) for 10 min using 50 mW cm-2 light intensity previously to the CMA induction. Hence, only the proteins with the photoactivated reporter will be followed and not those synthesized during the experiment, so we could estimate the CMA activity. More than 90% of the cells were viable after the photoactivation. These experiments were carried out at the laboratory of Dr. Ana Maria Cuervo, Albert Einstein College of Medicine (New York, USA). Depending on the experiment, images were acquired by different microscopes. For eplifluorescence a Zeiss Axioscopp microscope was used and for confocal acquisition, a Leica TCS-SP5-A0BS.

3.6.2. ONL thickness measurement

This technique allows following the degeneration of the photoreceptor nuclear layer in an easy way. Retinal cryosections stained with DAPI and mounted with DABCO were used for the measurement.

3.6.3. Images acquisition

Images were taken with an epifluorescence microscope at 40x of magnification. Six images were taken in total on every section, three at each side of the optic nerve, as disposed in Figure 3.6 at least, 3 sections of every sample are needed for the quantification.

Using ImageJ software, the thickness of ONL and INL was measured at three points in every image (1, 2, 3 in Figure 3.7). Then, we calculated the ratio ONL/INL at each point and the mean in the picture, and, finally, the mean of the three images acquired in each position (A, B, C, D, E, F) in the cryosection. This is repeated in at least three cryosections for each sample.

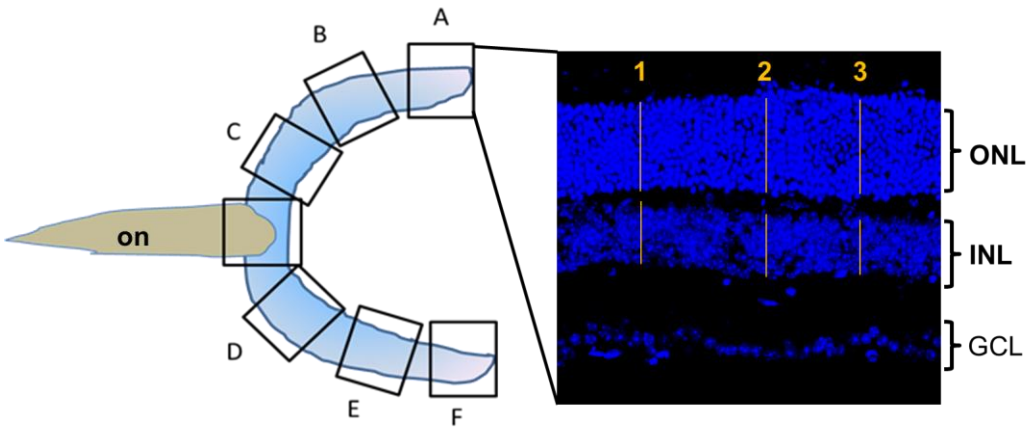

Figure 3.7. Representation of the measurement of the ONL and INL thickness in a retinal cryosection. Left illustration exemplifies a retinal cryosection and the 6 acquisitions distributed along the retina (A, B, C, D, E, F). Right image shows an example of a retinal cryosection stained with DAPI, showing the three nuclear layers: ONL, INL and GCL. Here, there are represented three example points for the measurements performed in each image (1, 2, 3). ONL: outer nuclear layer, INL: inner nuclear layer, GCL: ganglion nuclear

The ratio ONL/INL is calculated in order to relativize the value of the ONL to a constant value, as the INL thickness, eliminating errors associated with eye orientation before sectioning and making it comparable parameter between samples.

3.7. Flow cytometry for cell death detection on cell lines

661W cells were plated at 125 cell/mm^2. After the culture, cells were washed with PBS, trypsinized and centrifuged 5 minutes at 1000 r.p.m. Then, cells were resuspended in DMEM with propidium iodide at 1 mg/mL and were incubated at 37ºC for 5 min. The signal was measured by a flow cytometer EPICS XL (Beckman Coulter, California,USA.), analyzing 20.000 cells per sample.

3.8. Protein extraction

For protein extraction from cultured cells, after the treatment, cells were washed with PBS and collected in 200 µL of lysis buffer (50 mM Tris-HCl pH 6.8, 10% glicerol (v/v), 2% SDS (p/v) with protease inhibitors (Roche, Indianapolis, UEE.U.) and phosphatase inhibitors (1 mM sodium orthovanadate, 1 mM sodium fluoride, 5 mM sodium pirophosphate).

For protein extraction from retina or cerebellum, once the tissues were obtained, they were immediately frozen at -80ºC, until usage, or they were directly immersed in 75 µL of buffer lysis (in the case of the retina) or 150 µL (in the case of the cerebellum). To disaggregate the tissues, a plastic homogenizer for the retinas or a sonicator for the cerebella were used.

For protein denaturalization in all cases, the homogenates were heated to 95ºC for 10 minutes and then, cerebellum samples were centrifuged at 10.000g for 5 minutes to rescue the supernatant, avoiding tissue debris. Then, samples were kept at -20ºC until usage. The protein quantification the samples, was performed with a BCA Protein Assay© (Pierce, Thermo Fisher Scientific Inc., Ilinois, USA) and samples were measured with the wavelength of 540 nm.

3.9. Western blot

30 µg per sample were mixed with loading buffer (10 mM DTT and 0.005% (p/v) bromophenol blue), to fill the adequate volume for the wells of the gel, and then were run in a AnyKD Criterion™ TGX™ Precast Gels (BioRad) with a Criterion™ Cell electrophoresis system (BioRad). Later, proteins were transferred to a PVDF membrane (Trans-Blot® Turbo™ Midi PVDF Transfer, BioRad) with Trans-Blot® Turbo™ Transfer System (BioRad). PVDF membranes were blocked with 5% milk (p/v) in PBS-T (PBS 1X, 0.5% tween 20 (v/v)) for 1h, washed three times with PBS-T and incubated with the primary antibodies o/n at 4ºC in a shaker. Primary antibodies were diluted in 3% BSA with 0.001% of sodium azide. After washing the membranes with PBS-T, they were incubated with the secondary antibodies peroxidase-conjugated (dilution 1:2000-1:10000, Pierce) diluted in PBS-T 1h at RT, in a shaker. After the last washing step, membranes were incubated with SuperSignal West Pico Chemioluminiscent

Substrate (Pierce). The signal was detected and photographed with Fuji Film Intelligent Dark with a Fuji LAS-3000 camera. The bands were quantified with ImageJ program.

3.9.1. Primary and secondary antibodies for Western blot protein detection

The proteins detected by western blot are listed above in Table 3.3.

Detected protein	Provider	Reference	Specie	Dilution
LC3	MBL	PD014	Mouse	1:2000
Lamp2	Invitrogen	51-2200	Rabbit	1:1000
Hsc70	Enzo	ADI-SPA-815	Rat	1:1000
p62	Enzo	BML-PW9860	Rabbit	1:1000
Ubiquitin	Santa Cruz	sc-8017	Mouse	1:1000
Tubulin	Santa Cruz	sc-8035	Mouse	1:5000
GAPDH	Abcam	ab8245	Mouse	1:5000
Actin	Sigma	A-5441	Mouse	1:5000

Table 3.3. List of the antibodies used for protein detection by western blot, detailing the provider, reference, animal specie in which it was obtained and used dilution.

3.10. Statistical analysis

Statistical analysis was performed with IBM SPSS statistics 21. In case the data were normal, to compare two conditions t test was applied and ANOVA for more conditions. In case the data were not normal, U-Mann Whitney was applied and for more conditions Kruskal Wallis was applied. Data are shown as the mean value +/- standard error.

4. RESULTS

4. RESULTS

4.1. STUDY OF THE RELATION BETWEEN AUTOPHAGY AND NEURODEGENERATION

It has been shown a crescent relation of autophagy with neurodegenerative diseases, which are also linked to aging in many cases. The focus of our study was to understand how the lack of autophagy affects the physiology of the central nervous system, and if it also leads to neurodegeneration and how. For this purpose, we have studied two areas of the CNS, whose relation with autophagy remains widely unknown: retina and cerebellum, in the mouse model presented by Hara et al. (2006). We have chosen to perform the study of these animals at seven weeks of age, the early stages of neurodegeneration, and we also compared them in some cases with aged animals (12 and 24 month-old) in order to answer our question.

4.2.1. RETINAL PHENOTYPE IN *Atg5* $^{flox/flox}$; nestin-*Cre* MICE AND COMPARISON WITH RETINAL PHENOTYPE IN AGED MICE.

We characterised the retinal phenotype of the *Atg5* $^{flox/flox}$; nestin-*Cre* mouse retina at six and seven weeks of age, focusing in four aspects: functional and structural alterations, macroglial response and proteostatic balance.

4.2.1.1. Analysis of the visual function of *Atg5* $^{flox/flox}$; nestin-*Cre* mice retina

The visual function of *Atg5* $^{flox/flox}$; nestin-*Cre* mice was studied by electroretinography. This technique consists on registering the electric response of the retina after the exposure to different light flashes. The performed electroretinogram (ERG) is a modification of the standard proposed for humans by the ISCEV (International Society for Clinical Electrophysiology of Vision), adapted to mice retina and implemented with some more recordings. It was done in collaboration with the group of Prof. Pedro de la Villa at the Universidad de Alcalá de Henares. The designed ERG is a full field protocol which includes scotopic and photopic tests. The scotopic tests are done after adapting the eye to darkness and they reflect the night vision performance, which is carried out by rods and downstream neurons. For photopic tests the eye is pre-adapted to bright light and they reflect the activity of the cone pathway, responsible for the diurnal vision, as rods are bleached in these conditions.

The study of the scotopic conditions response was measured after darkness adaptation and applying flashes with different intensity to obtain the following waves:

- b-scotopic: it reflects the electrical work of rod bipolars, which are all ON type.
- a-mixed: it shows the combined work of cone and rod photoreceptors.
- b-mixed: shows the functionality of ON bipolars, both of rods and cones, and the OFF bipolars of cones.
- Oscillatory potentials: these waves reflect the performance of amacrine and, to a lesser

extent, ganglion cells.

- Scotopic threshold response (STR): it is a response obtained to light stimuli near to rod minimum threshold. It shows the activity of the ganglionar cells downstream of the rods, which is a reflection of the “rod only” (not mixed with cones) activity.

For the study of photopic conditions response, the recorded waves were:

- Flicker: it reflects the activity of cones.
- b-photopic: represents the electrical work of cone bipolars.

The results for all the waves registered for *Atg5* $^{flox/flox}$; nestin-*Cre* mice at six weeks of age and their control littermates are shown in Figure 4.1 *Atg5* $^{flox/flox}$; nestin-*Cre* mice show a reduced electrical work of rods (reflected through the work of their ganglionar cells downstream on the STR wave), rod bipolars (b-scotopic wave) and amacrine and ganglion cells (OP), which on the whole they are indicating that *Atg5* $^{flox/flox}$; nestin-*Cre* mice present a diminished response in scotopic conditions at different levels of the neuronal pathway, and thus, a deficient night vision.

On the other hand, flicker and b-photopic waves are not altered, showing that cones and cone

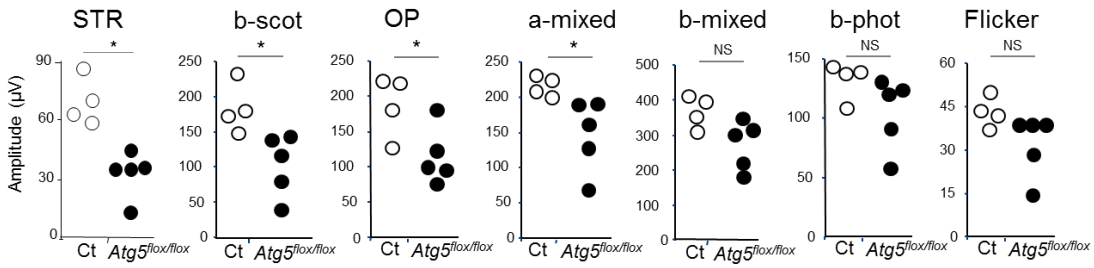

Figure 4.1 Values of the electroretinograms for control (Ctr) and *Atg5* $^{flox/flox}$; nestin-Cre mice (*Atg5* $^{flox/flox}$) at 6 weeks of age (n = 5). STR, scotopic threshold potential; OP, oscillatory potentials, b-scot: b-scotopic wave, b-phot: b-photopic wave. *P < 0.05 vs. Ctr.

bipolars present normal activity and, thus, the diurnal vision of *Atg5* $^{flox/flox}$; nestin-*Cre* mice is not affected.

As mentioned above, a- and b-mixed waves reflect the combined work of both responses from rods and cones. The register of the a-mixed wave shows a lower response of the photoreceptors of *Atg5* $^{flox/flox}$; nestin-*Cre* in relation to control. As we know that cones are stable, the a- mixed wave is reflecting the alteration of rods. However, on the case of bipolars, b-mixed is not significantly affected, even if the b-scotopic wave shows that rod bipolars have a decreased activity, which is probably due to the sample size.

In summary, we can conclude that rods of *Atg5* $^{flox/flox}$; nestin-*Cre* retinas are showing a diminished response, which attenuates the activity of their downstream neurons as bipolars and amacrine cells, while, on the other hand, cones are preserving their functionality.

4.2.1.2. Structural study of the retina of *Atg5* $^{flox/flox}$; nestin-*Cre* mice

The ERG is a study of the visual function and so it may point out morphological alterations of the retina. Thus, as the altered waves were indicating a poor activity of rods, we first checked if the photoreceptor population was degenerating. We measured the ONL thickness of *Atg5*$^{flox/flox}$; nestin-*Cre* retinas and their control littermates at seven weeks of age. The obtained results are depicted in Figure 4.2, as well as the mean of the ONL thickness (that is, the mean of all the measured points in a retina, simplifying every retina to only one point). We can appreciate that there is a reduction in all the measured points and also in the mean value, indicating that *Atg5*$^{flox/flox}$; nestin-*Cre* retinas present a degeneration of the ONL.

For further verification of the degeneration, and to observe if it was also occurring in other

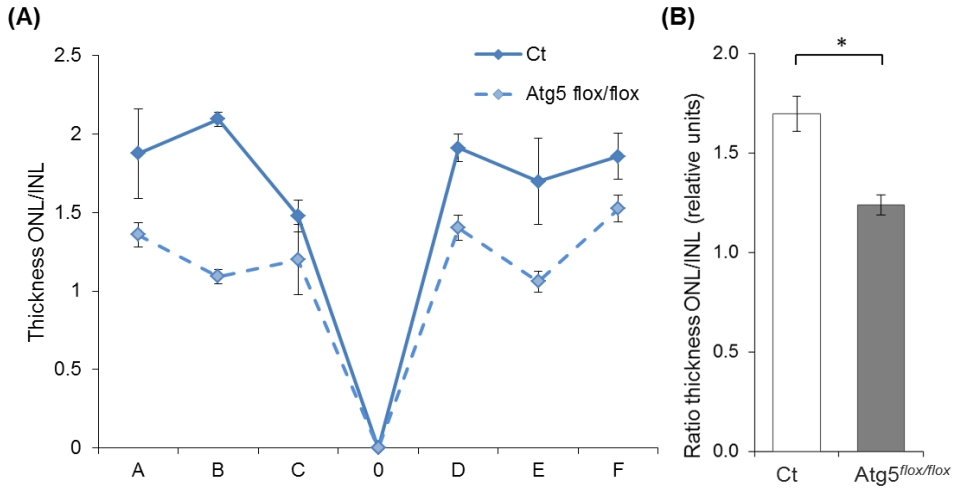

Figure 4.2. (A) Example of the comparison of the ONL/INL thickness between a *Atg5*$^{flox/flox}$; nestin-*Cre* mice and its wild-type littermates at 7 weeks of age, (B) Representaion of the mean of the ONL/INL thickness in medial-central retina of wild-type and a *Atg5*$^{flox/flox}$; nestin-*Cre* mice.

cellular layers, we used a TUNEL staining in cryosections of retinas of *Atg5*$^{flox/flox}$; nestin-*Cre*

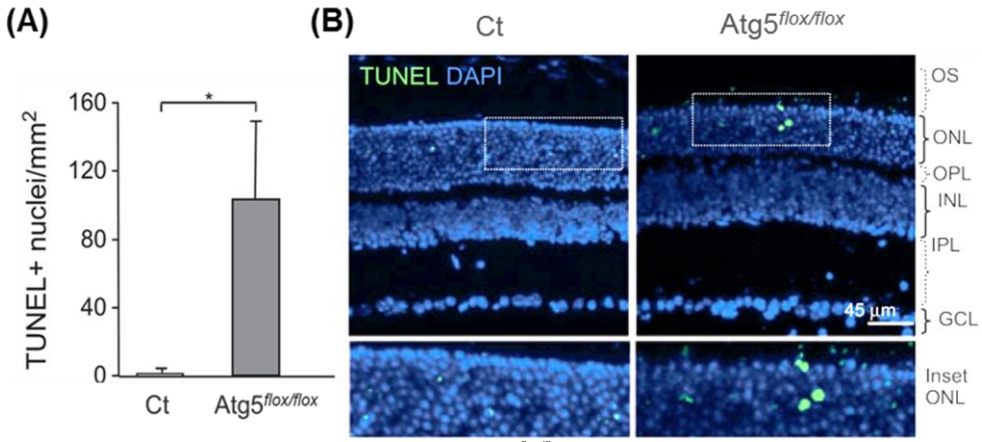

Figure 4.3. (A) TUNEL staining in retinal sections of *Atg5*$^{flox/flox}$; nestin-*Cre* mice and control littermates at 7 weeks of age and the corresponding quantification (B). OS, outer segment; ONL, outer nuclear layer; OPL, outer plexiform layer; INL, inner nuclear layer; IPL, inner plexiform layer; and GCL, ganglion cell layer. Scale bar as depicted.

mice and their controls. Figure 4.3 shows that cell death is only detected in the photoreceptor

layer. Moreover, in combination with immunostaining for cone opsins, we observed that they were never colocalizing, thus cell death was not occurring in cones (Figure 4.4) and we neither observe morphological alterations.

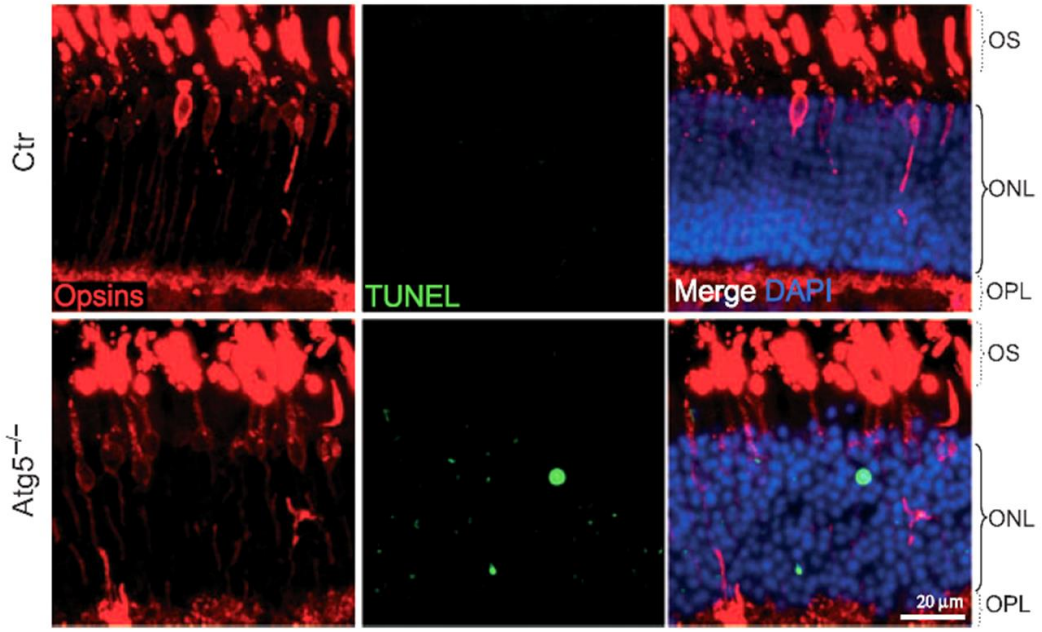

Figure 4.4. Representative immunostaining for cones in retinal cryosections from control (Ctr) and *Atg5*$^{flox/flox}$; nestin-*Cre* mice at 7 weeks of age by combination of blue and red/green opsins (red). Apoptotic cells are stained by TUNEL (green). OS, outer segment; ONL, outer nuclear layer; OPL, outer plexiform layer; INL, inner nuclear layer; IPL, inner plexiform layer; and GCL, ganglion cell layer. Scale bar as depicted.

Thus, we can conclude that *Atg5*$^{flox/flox}$; nestin-*Cre* mice retina presents degeneration of rods at seven weeks of age, which could be the cause of the observed reduced night vision, while cones are preserved.

Next, as the ERG also indicated a reduced activity of rod bipolar cells but no TUNEL staining was found on the INL, we checked if their morphology could show degenerative signs with an immunostaining for protein kinase C alpha (PKCα), a specific protein expressed in these cells. We found two degenerative symptoms quite frequent in the rod bipolar cells of the *Atg5*$^{flox/flox}$; nestin-*Cre* retinas. On the one hand, some PKC-α positive cells were losing their dendritic arborisation, as shown in Figure 4.5 (A-bottom panel- and B-top panel-). On the other hand, we observed that some varicosities appear empty (Figure 4.5 (A-bottom panel- and B-bottom panel, bottom image). Both symptoms have been described in neurons that are not receiving any electrical input and are starting to degenerate (Cuenca et al., 2015; Cuenca et al., 2004; Marchena et al., 2011). In our case, rod bipolar cells would be degenerating as a consequence of rod disappearance.

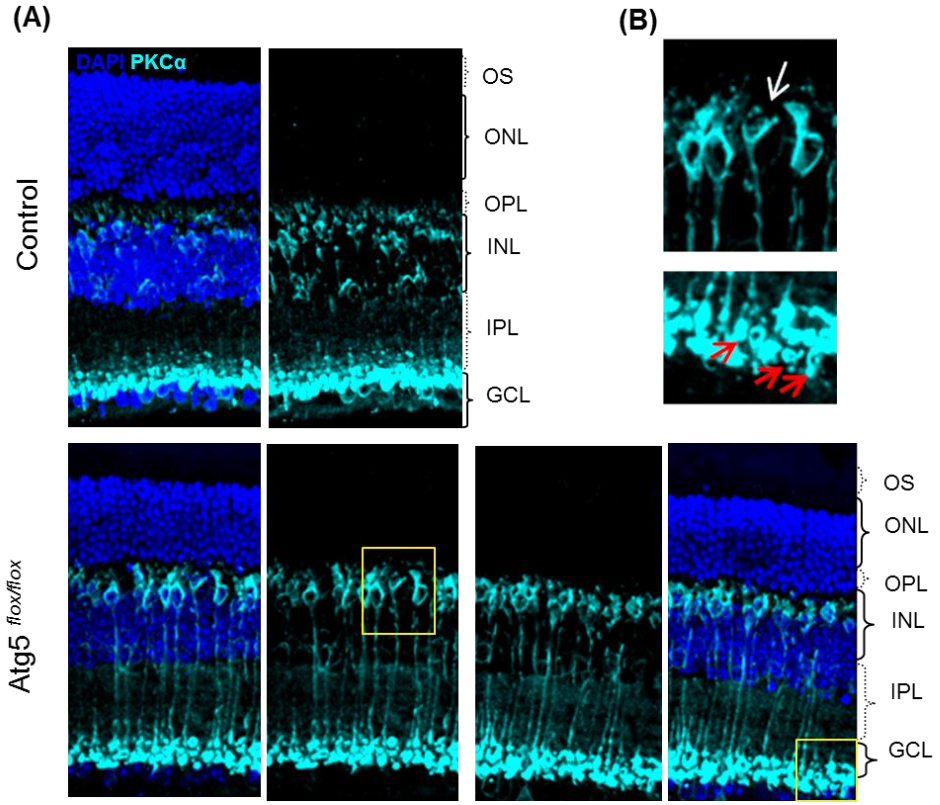

Figure 4.5. (A) PKC staining in retinal sections of *Atg5*$^{flox/flox}$; nestin-*Cre* mice and control littermates at 7 weeks of age, labeling rod bipolar cells, (B) magnification of a defective dendritic arborisation (top image) and empty

The ERG also showed an alteration of the amacrine cells, on the oscillatory potentials waves. To study the morphology of the amacrine cells, we performed a calbindin immunostaing on retinal cryosections (Figure 4.6). We did not find any difference in the amacrine cells (A and dA in Figure 4.6) between control retinas and *Atg5*$^{flox/flox}$; nestin-*Cre* retinas. Maybe, the alteration of the OP could reflect an affectation of the amacrine cells at a functional level but could not be detected at the level of morphological alterations. Calbindin also detects horizontal cells (H in Figure 4.6), which are not clearly reflected in the ERG, completing our study. We did not find any difference in their dendritic arborisation in the *Atg5*$^{flox/flox}$; nestin-*Cre* retinas, but we found that some of the somas of their horizontal cells were presenting a slightly sclerotical position, situating them among the dendritic processes.

In conclusion, our data show that *Atg5*$^{flox/flox}$; nestin-*Cre* mice present a decreased night vision because rods are degenerating and rod bipolars are starting to degenerate. Also horizontal cells present an altered position in the INL. On the contrary diurnal vision is maintained, and cones do not seem to be affected by degeneration.

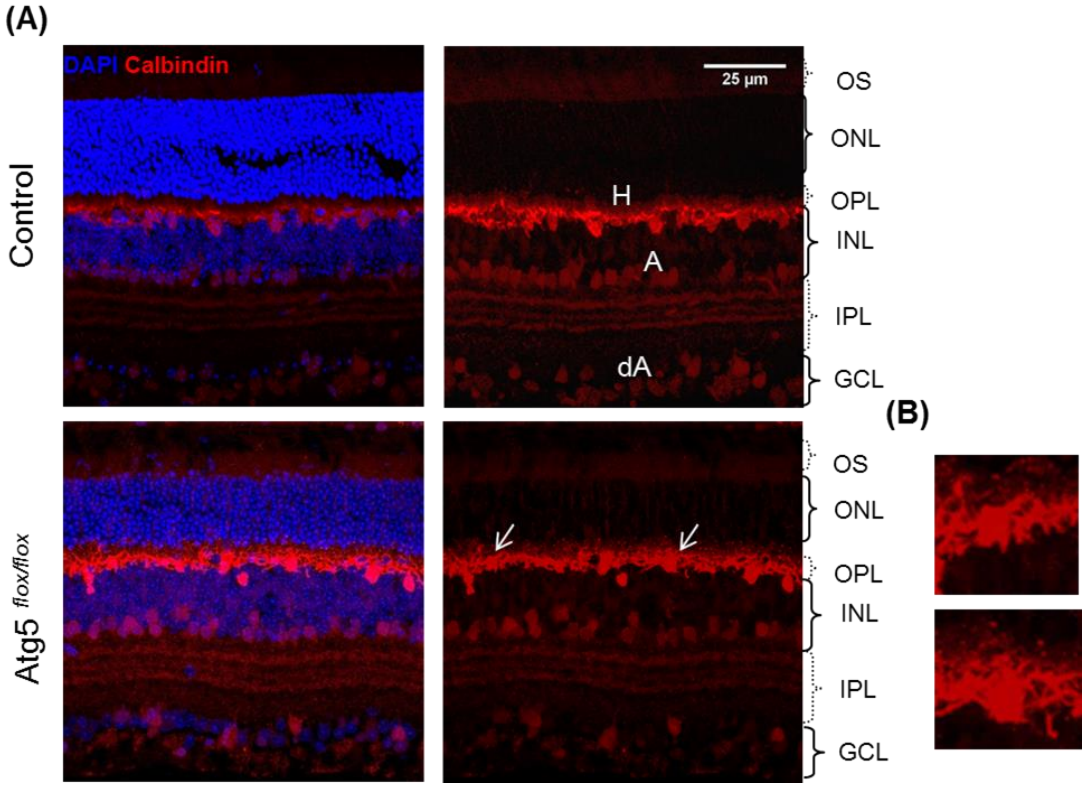

Figure 4.6. (A) Calbindin staining in retinal sections of *Atg5*$^{flox/flox}$; nestin-*Cre* mice and its control littermates at 7 weeks of age, showing horizontal (H), amacrine (A) and displaced amacrine cells(dA), (B) maginification of 2 horizontal cells with a slight sclerotical position of *Atg5*$^{flox/flox}$; nestin-*Cre* retina.

4.2.1.3. Study of the activation state of macroglia in the retina of *Atg5* $^{flox/flox}$; nestin-*Cre* mice and comparison with aged retina

In many neurodegenerative processes, the glia is activated to protect the tissue from the damage (Cappellano et al., 2013) and retina is not an exception (Cuenca et al., 2015). In the retina, the glia is divided into macroglia and microglia. Macroglia includes Müller cells, radial cells that cross all the retina layers, and astrocites, mainly placed in the ganglion cell layer. They maintain the homeostasis of the environment around the neurons (control the levels of released neurotransmitters, water and ion concentrations and help in neuromodulation processes), provide trophic support and also activate microglia in case of injury. Microglia, also helps to maintain the homeostasis of the neuronal environment and besides, they act as phagocytes (Cuenca et al., 2015; Kolb, 2013 ed).

Activation of macroglia is seen in early stages of retinal degeneration (Cuenca et al., 2015). During activation, astrocytes present hypertrophy, ramify their processes and increase their GFAP expression (Formichella et al.). Thus, we studied the activation state of astrocytes in *Atg5*$^{flox/flox}$; nestin-*Cre mice* and their control littermates at seven weeks of age by immunostaining flat-mount retinas at the ganglion cell layer for GFAP, a specific protein of macroglia. We observed that the retinas of *Atg5*$^{flox/flox}$; nestin-*Cre* mice at seven weeks present

more intense GFAP staining. Astrocytes of these retinas are hypertrophic, as their soma occupies more area than in control animals and they are more ramified too (Figure 4.6).

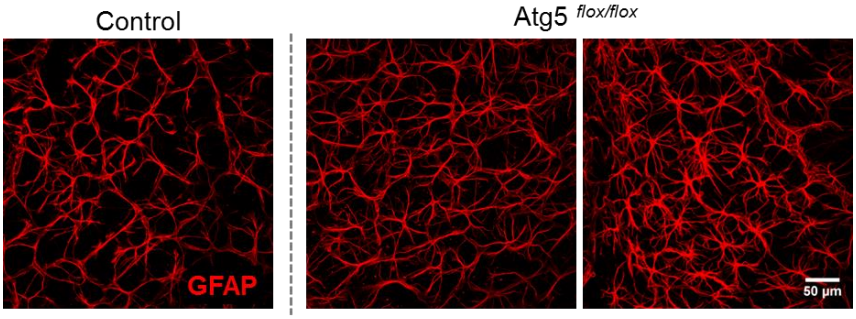

Figure 4.7. Flat-mounted retinas of *Atg5*$^{flox/flox}$; nestin-*Cre* mice and control littermate at 7 weeks of age immunostained for GFAP for astrocyte visualization.

As we know from previous work of our laboratory, that aged retinas shared some features with *Atg5*$^{flox/flox}$; nestin-*Cre* retinas, such as declined autophagy and degeneration (Rodríguez-Muela, 2011), we tested the macroglia activation state in aged. Therefore, we performed the same approach in flat-mount retinas of aged mice (12 and 24 months) and compared them with 3 month-old control retinas. Astrocytes of aged retinas were progressively more reactive with age. They presented wider soma area, more ramifications and those were also thicker and longer than in control astrocytes.

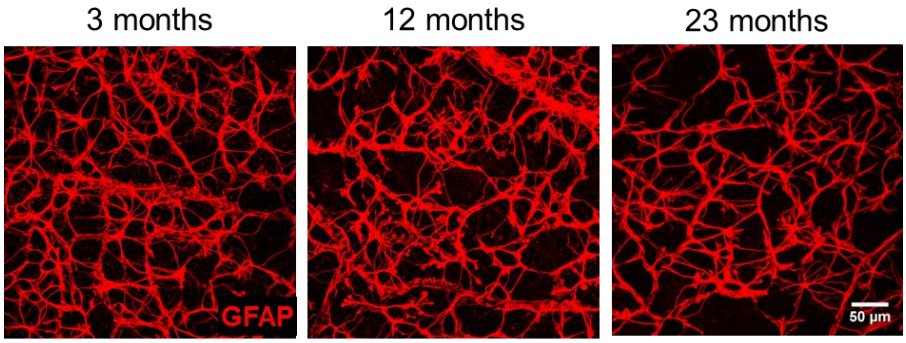

Figure 4.8. Flat-mounted retinas of 3, 12 and 24 month-old mice immunostained for GFAP for astrocyte visualization.

In conclusion, these data show that the degeneration observed in *Atg5*$^{flox/flox}$; nestin-*Cre* and aged retinas goes along with the activation of astrocytes.

4.2.1.4. Proteostasis alterations in the retina of *Atg5* $^{flox/flox}$; nestin-*Cre* mice: similarities with aging

From the description of the model of *Atg5*$^{flox/flox}$; nestin-*Cre* mice (Hara et al., 2006), we know that autophagy is blocked in the CNS, inducing the accumulation of inclusion bodies and autophagy related proteins as p62 and ubiquitin in several regions of the brain, as mentioned in

the introduction . Hence, as the retina is a particular component of the CNS, we checked if this accumulation was also occurring in the retinal tissue.

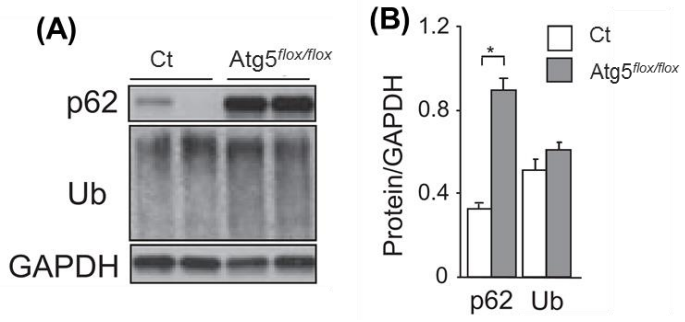

Figure 4.9. (A) Determination of the levels of p62 and ubiquitin by westernblot detection of *Atg5*$^{flox/flox}$; nestin-Cre mice and its control littermates at seven weeks of age and (E) its corresponding quantification.

As shown in Figure 4.9, *Atg5*$^{flox/flox}$; nestin-*Cre* retinas presented higher levels of p62 and ubiquitin than control. We then analysed the distribution of the accumulation of p62 along the retinal layers with an immunostaining in retinal cryosections (Figure 4.10). We found accumulation of p62 in all the layers, but especially in the IPL, where there are numerous and large accumulations.

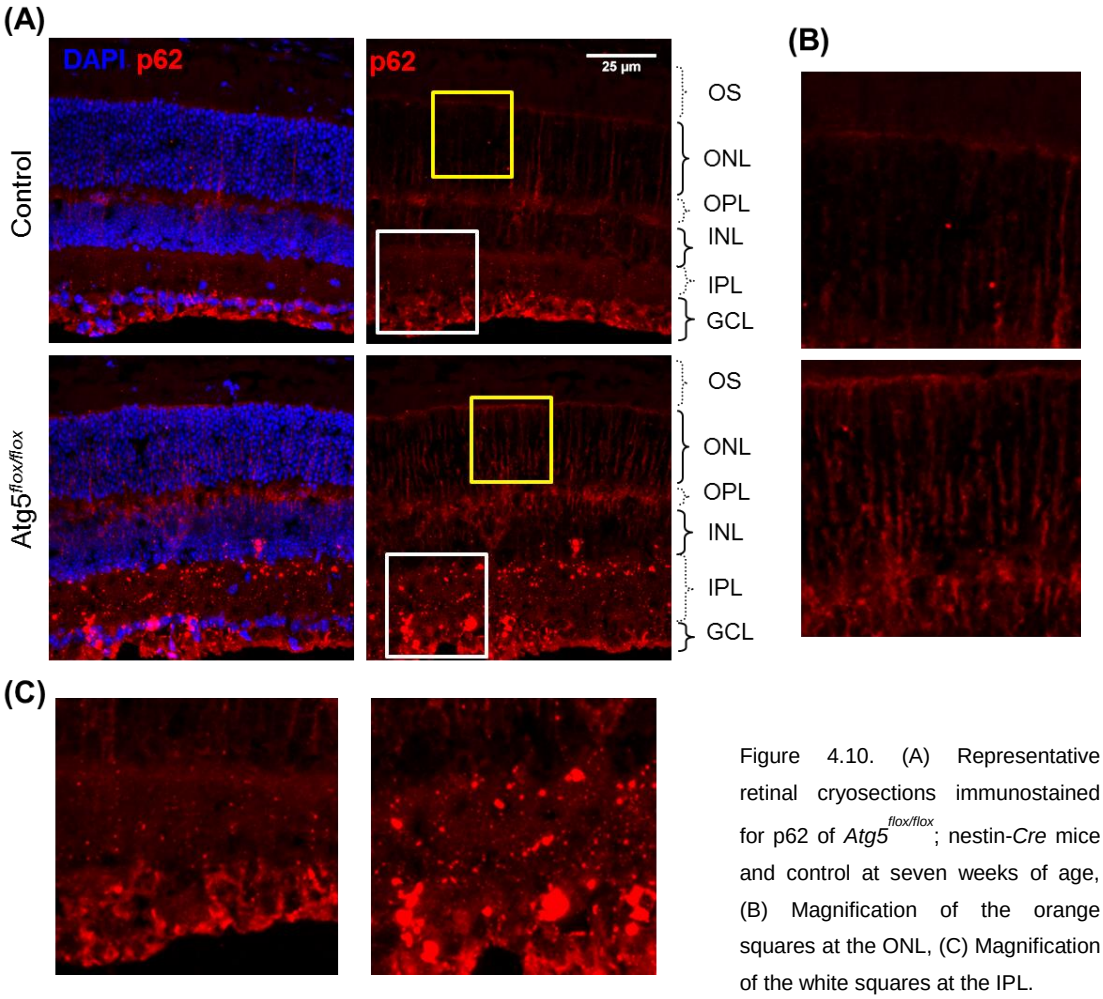

Figure 4.10. (A) Representative retinal cryosections immunostained for p62 of *Atg5*$^{flox/flox}$; nestin-*Cre* mice and control at seven weeks of age, (B) Magnification of the orange squares at the ONL, (C) Magnification of the white squares at the IPL.

As mentioned before, previous results showed that aged retinas presented defective autophagy, as many other tissues (Rodríguez-Muela, 2011) and that they also accumulated p62.

This increase was progressive with time (Figure 4.11 -A and B) and independent of mRNA

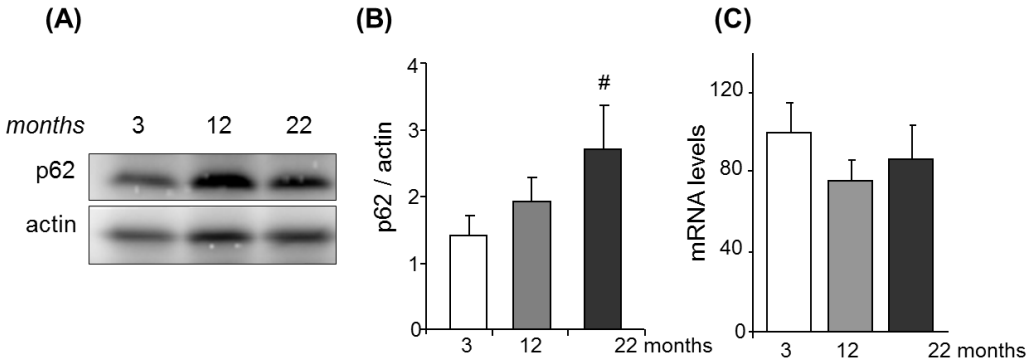

Figure 4.11. Determination of the protein levels ofp62 in mice at 3, 12 and 22 month of age (A) and its respective densitometry quantification (B) and (C) p62 mRNA expression determined by qPCR.in retinal extracts from 3-, 12-, and 22-month-old animals (n = 6). *P < 0.05. Extracted from (Rodriguez-Muela et al., 2013).

expression enhancement (Figure 4.12 -C). Thus, we performed an immunostaining of retinal cryosections of aged retinas for p62 in order to observe if the p62 also followed a differentiated pattern as in *Atg5*$^{flox/flox}$; nestin-*Cre* retinas Figure4.12 shows the obtained results. p62 was also distributed along all layers, but in a milder way than in *Atg5*$^{flox/flox}$; nestin-*Cre* retinas and with a slightly different pattern than in *Atg5*$^{flox/flox}$; nestin-*Cre* retinas, which will be discussed later.

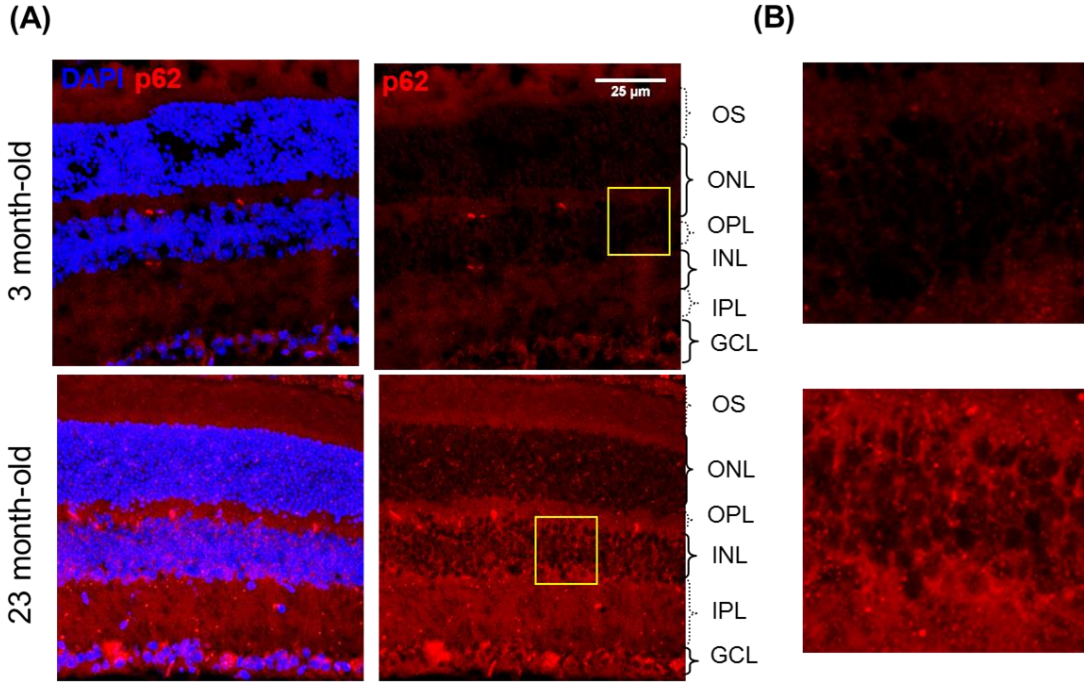

Figure 4.12 (A) p62 immunostaining of retinal cryosections of *Atg5*$^{flox/flox}$; nestin-*Cre* mice and control at seven weeks of age, (B) Magnification of the framed area in INL.

In conclusion, our data show that autophagy blockage originated whether by autophagy inhibition or aging induces the accumulation of p62 and ubiquitine along all the retinal layers, which is especially relevant at the IPL of the *Atg5*$^{flox/flox}$; nestin-*Cre* retinas.

4.2.1.5. Study of the link between macroautophagy and CMA in the retina of *Atg5* $^{flox/flox}$; nestin-*Cre* mice and possible relations with aging

As mentioned before, in some tissues, an alteration of macroautophagy originates a compensation by increasing CMA activity levels, and vice versa (Cuervo and Wong, 2014). We, thus, wondered if this phenomenon could happen in our models.

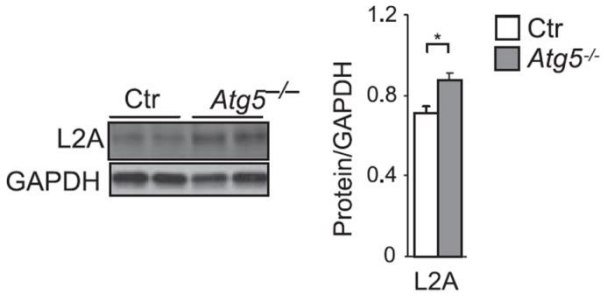

Figure 4.13. Determination of the protein levels of LAMP.2A in *Atg5*$^{flox/flox}$; nestin-Cre retinas at seven weeks of age and a control littermates (A) and the respective densitometric quantification (B).

We analysed LAMP-2A protein levels, as it is the limiting protein for CMA, by western blot and it revealed an increase of LAMP-2A in *Atg5*$^{flox/flox}$; nestin-*Cre* retinas compared to control (Figure 4.13). Thus, we also checked by immunostaining if any cell subset of the retina could be participating more in the observed enhancement of CMA. Indeed, we found a slight increase of

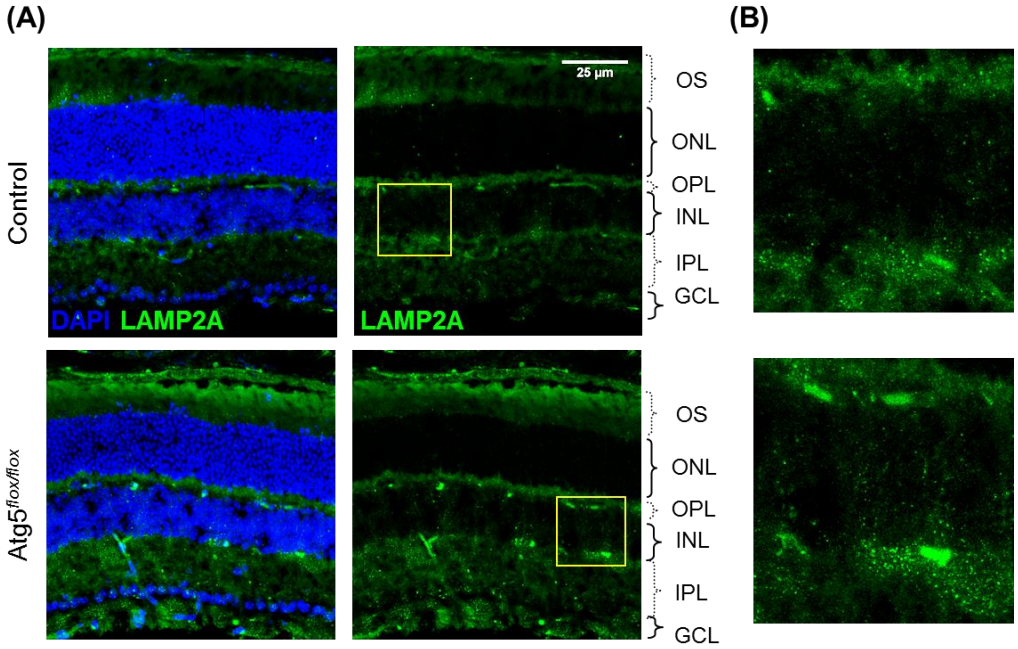

Figure 4.14. (A) LAMP-2A immunostaining of retinal cryosections of mice at 3 and 23 month-old (B) Magnification of the framed area in INL.

LAMP-2A in lysosomes in all layers of the retina. Especially they were more patent in the INL as well as in the GCL, but also a more blurry pattern appeared in both plexiform layers and the OS of the photoreceptors (Figure 4.14).

As mentioned above, in some models it has been shown that CMA could compensate the lack of macroautophagy, but it has been seen reduced CMA activity with age (Cuervo and Wong, 2014); (Schneider et al., 2015). Hence, we checked the situation of LAMP-2A in aged retinas, as we knew from previous data that this protein,unlike other tissues, was also increased (Figure 4.15) (Rodríguez-Muela, 2011).

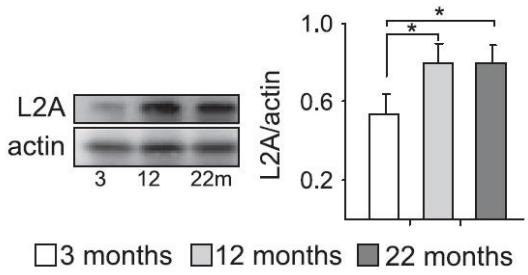

Figure 4.15 Determination of the protein levels of LAMP-2A in retina from mice at 3, 12 and 22 month of age (A) and its respective densitometry quantification (B).

We, then, performed an immunostaining to compare if there was a similar pattern or, on the contrary, there would be differences as also for p62. Figure 4.16 shows that there is a remarkable increase of LAMP-2A in all layers, especially in the INL and GCL, as well as in the plexiform layers, even if with a more diffuse distribution, as observed in *Atg5*$^{flox/flox}$; nestin-*Cre* retinas.

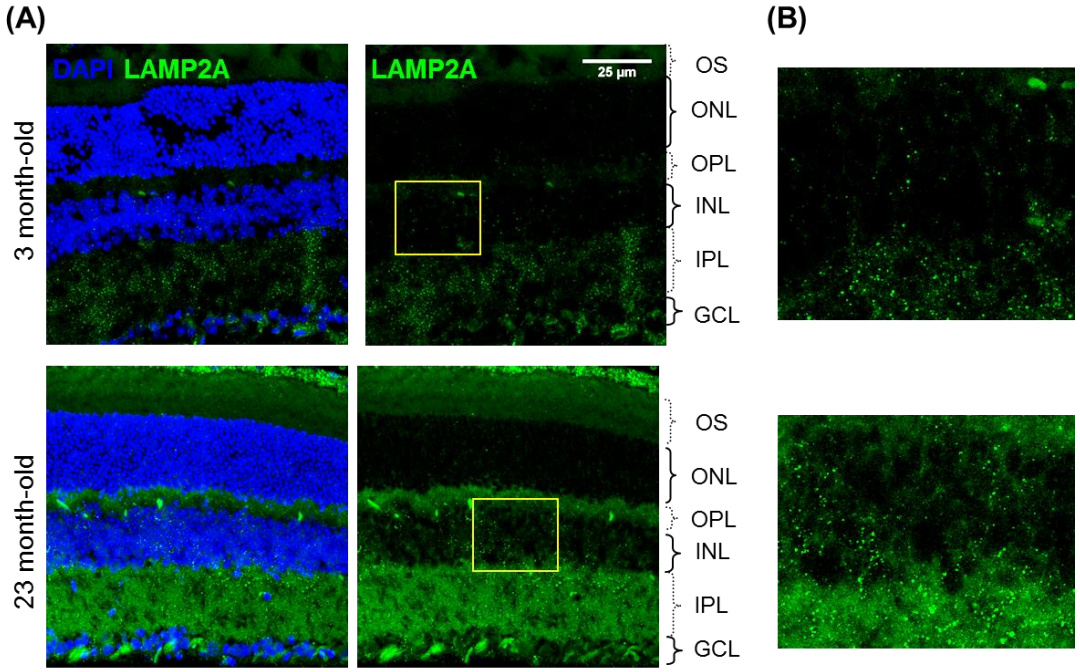

Figure 4.16. (A) LAMP-2A immunostaining of retinal cryosections of mice at 3 and 23 month-old (B) Magnification of the framed area in INL.

As described in the introduction, LAMP-2A is the limiting protein of CMA, but to develop its function, the collaboration of the co-chaperone Hsc70 is needed. Therefore, we analysed the presence of Hsc70 in *Atg5*$^{flox/flox}$; nestin-*Cre* retinas by immunostaining to precise its localization.

We found that, in control retinas, Hsc70 is present in all cell layers and that it is increased in *Atg5*$^{flox/flox}$; nestin-*Cre* retinas. However, it is remarkable the difference in the levels of Hsc70 in the ONL, among cones and rods, where the former present enhanced levels of the protein Figure 4.17-A and B). Nonetheless, in the INL and GCL the levels are more equilibrated in all cell types included.

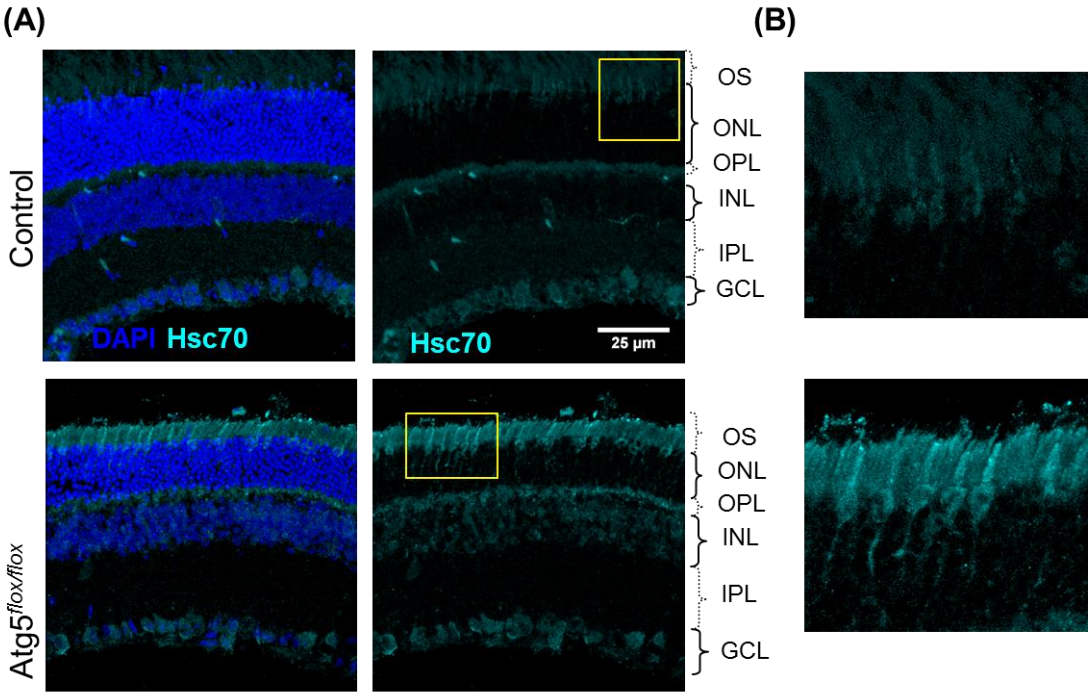

Figure 4.17(A) Immunostaining for Hsc70 on retinal cryosections of retinas from wild-type and *Atg5*$^{flox/flox}$; nestin-*Cre* mice at 7 weeks of age (B) Detail of the IPL.

Thus, we checked if this fact was also common to aged retinas. Figure 4.18 shows that retinas at 3 months present a similar distribution to that observed before both in control and aged retinas. As well, we observed that the increased levels of Hsc70 in all layers but the difference between cones and rods was persistent and this was enhanced in aged retinas. There was also an increase of Hsc70 in the other layers but again the levels among them remained balanced. This shows that the different levels between cones and rods were not a punctual phenomenon produced at seven weeks of age in C57/Bl6 mice but a basal condition.

The observed increased levels in LAMP-2A and Hsc70, fundamental proteins for CMA activity, in *Atg5*$^{flox/flox}$; nestin-*Cre* and aged retinas suggest the possibility of a compensation between macroautophagy and CMA, especially remarkable in cones.

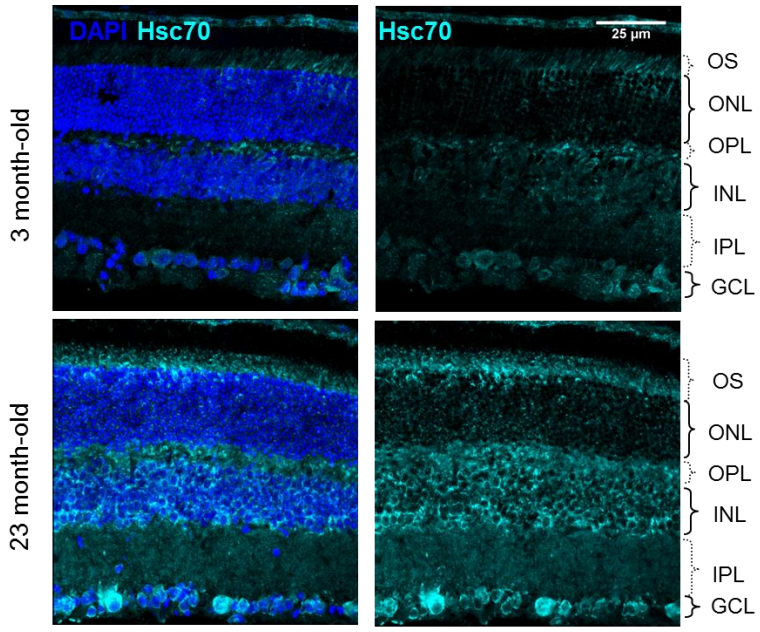

Figure 4.18 Immunostaining on retinal cryosections of mice at 3 and 23 month-old for the protein Hsc70.

4.2.1.6. Study of the crosstalk between macroautophagy and CMA in 661W cell line

To confirm the possible existence of a balance between macroautophagy and CMA in the retina and, especially in cones, we used a *in vitro* model: the 661W cone-derived cell line. These experiments were performed in collaboraton with the laboratory of Dr. Ana María Cuervo. Hence, we knocked down two main proteins of the respective pathways: Atg7 and LAMP-2A. As it is shown on Figure 4.19, LAMP-2A KD 661W cells were expressing a minimal amount of LAMP-2A protein comparing to control cells (PGK), as well as Atg7 KD 661W cells were

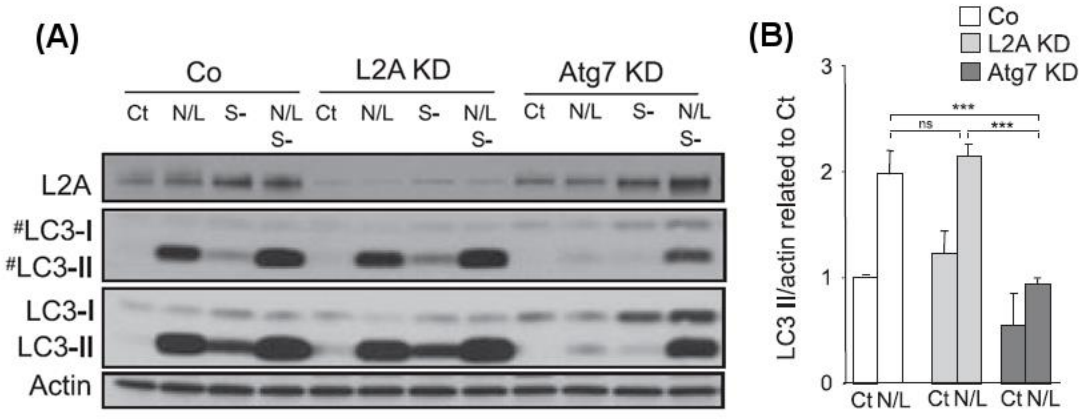

Figure 4.19. Westernblot detection for LAMP-2A (L2A) and LC3-I and II, and actin as loading control in control (PGK transfected cells), LAMP-2A KD and Atg7 KD 661w cells cultured in in the presence or absence of serum (S-) and of the lysosomal inhibitors ammonium chloride and leupeptin (N/L). (A) Representative immunoblot (#) lower exposure time immunoblot; (B) Densitometric quantification of LC3-II in A and autophagic flux determined as the ratio of LC3-II in the presence/absence of N/L (n = 3). ***P < 0.005.

expressing a significantly lower quantity of LC3-II, also in the presence of lysosomal inhibitors, indicating a decline of autophagy flux. We can appreciate too that in LAMP-2A KD cells, LC3 levels are similar to control and also Atg7 KD cells present comparable levels of LAMP-2A to control cells.

As mentioned before, protein levels do not necessary reflect an increase of the activity. Thus, 661W cells were cultured in serum-free medium to induce CMA. To follow the CMA activity, cells were transfected with the CMA reporter described by Koga et al. (2011b). It is a photoactivable fluorocrome linked to KFERQ proteins, which allows to follow the traffic of these proteins to CMA positive lysosomes. Representative images are shown on Figure 4.20 and it is perceptible that control and Atg7 KD cells are carrying a high number of KFERQ proteins to the lysosomes, while LAMP-2A KD cells are not. Moreover, the quantification puntualizes that Atg7 KD cells in basal conditions present increased CMA activity than control cells, but not in serum free conditions, where probably the cell reaches a plateau.

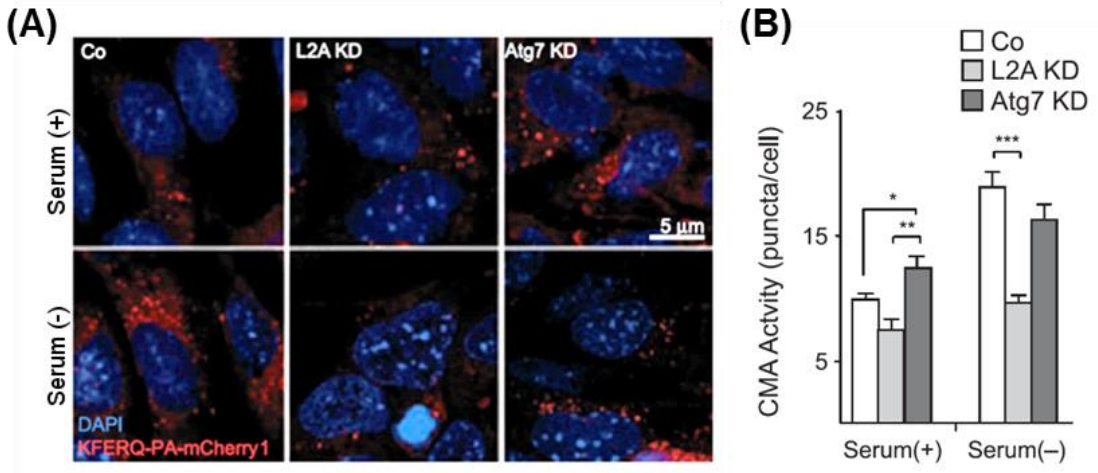

Figure 4.20. CMA activity was determined with the fluorescent reporter KFERQ-PA-mCherry1 in control, Atg7, and LAMP-2A KD 661W cells maintained in the presence or absence of serum for 16 h. Representative images (left) and quantification of the number of puncta per cell (right). Scale bar as depicted. *P < 0.05, ** P < 0.01, ***P < 0.005.

For studying macroautophagic activity, we cultured the 661W control, LAMP-2A KD and Atg7 KD cells in the presence or absence of lysosomal inhibitors and performed an immunostaining of LC3. We analysed the images with the WimAutophagy module, explained in the next section of this chapter. Figure 4.21-A shows that, in fact, Atg7 KD cells were not able to perform macroautophagy, and APs are not detectable even in culture with N/L. The quantified levels of LC3 of LAMP-2A KD cells were lower than those of control cells (Figure 4.21-B), showing that they were not able to compensate the lack of CMA by increasing macroautophagy pathway, and their levels were even lower than control. The result of LAMP-2A KD cells is a bit contradictory with the obtained by the western blot, but it is explainable because the quantification performed by WimAutophagy only includes transfected cells while, by western blot, both populations of transfected and non-transfected cells are considered, shadowing the result.

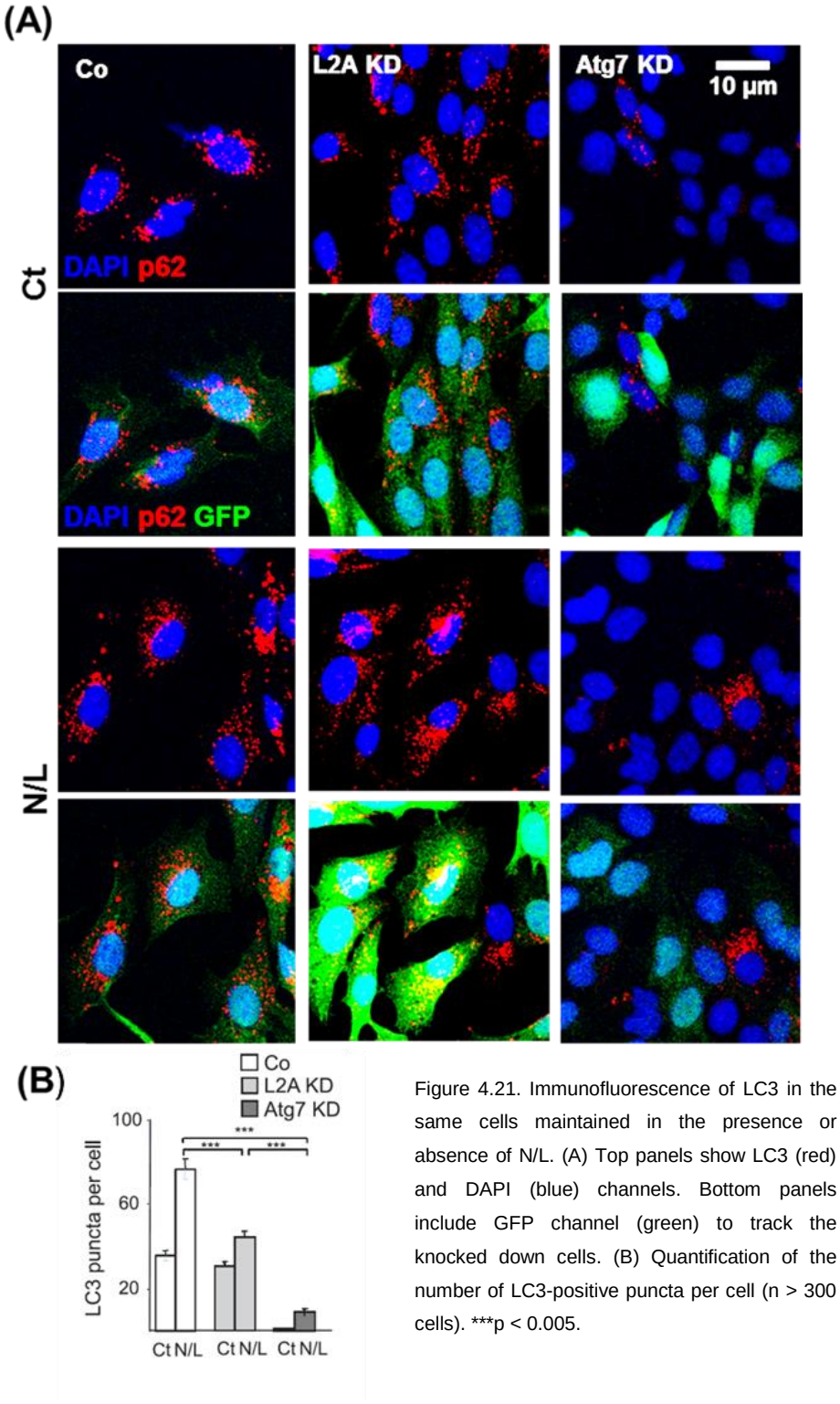

Figure 4.21. Immunofluorescence of LC3 in the same cells maintained in the presence or absence of N/L. (A) Top panels show LC3 (red) and DAPI (blue) channels. Bottom panels include GFP channel (green) to track the knocked down cells. (B) Quantification of the number of LC3-positive puncta per cell (n > 300 cells). ***p < 0.005.

Finally, to further understand the role of CMA in the homeostasis of cones, we challenged control, LAMP-2A KD and Atg7 KD 661W cells with paraquat 1 mM for 24 h, a ROS generator, and cell viability was measured by flow cytometry with propidium iodine. Results show that the lack of CMA function reduces de viability of 661W cells while the silencing of Atg7 does not affect them more than it does to control cells (Figure 4.22).

Thus, we can conclude that 661W cells can compensate the lack of macroautophagy with an increase of CMA activity, but not in the opposite way, which makes them more susceptible to stress. This suggests that CMA could be more necessary for the homeostasis of 661W cells than macroautophagy and therefore, it could also be for cones. It would explain why cones, which present higher levels of Hsc70 than rods, are protected against the degeneration caused

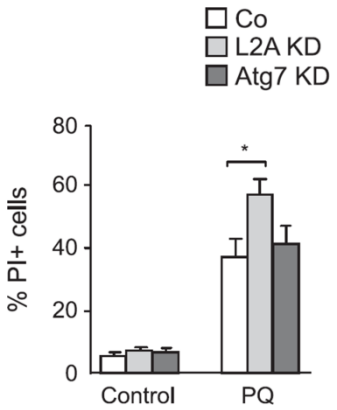

Figure 4.22. Cell viability as determined by propidium iodine (PI) staining and flow cytometry in control, Atg7 and LAMP-2A KD 661w cells treated with or without 150 µM paraquat (PQ) (n = 10). *P < 0.05.

by impaired macroautophagy, both by an original absence of autophagy or by a gradual decline of the process, and even when both cell types show similar levels of p62 accumulation. We can also affirm that the observed degeneration of the retinal tissue, which affects rods, bipolar rod cells and slightly horizontal cells, is inducing the activation of the macroglia that persists during the tissue damage, probably worsening the system. Finally, it seems that CMA activity is increased in the retina when macroautophagy is impaired, and thus, it could be acting as a compensation mechanism in the retina. However, our results suggest that there is a differential CMA ability between cones and rods, which could let the latter in disadvantage when facing a challenge.

4.2.2. STUDY OF THE MACROAUTOPHAGY AND CMA ACTIVATION STATE IN THE CEREBELUM OF *Atg5* $^{flox/flox}$; nestin-*Cre* MICE.

As the results shown in the previous section were suggesting a compensatory mechanism between macroautophagy and CMA, we studied if this phenomenon was exclusive of the retina or could similarly occur in different part of the CNS, as the cerebellum, which is a highly structured part of the CNS. We also focus on the cerebellum because in the description of the Atg5 $^{flox/flox}$; nestin-*Cre* model by Hara et al. (2006), they mention that granular cells of the cerebellum are more sensitive to the lack of autophagy and present a different pattern of cell death than Purkinje cells.

We first checked the levels of p62 and ubiquitin by western blot in the cerebellum of *Atg5* $^{flox/flox}$; nestin-*Cre* mice and control at six and eight weeks of age, to confirm the description of the model in cerebellum. p62 appears to accumulate with time, presenting a great increase at eight weeks in Atg5 $^{flox/flox}$; nestin-*Cre* animals (Figure 4.23). The levels of ubiquitin do not show

significant difference but it is perceptible a slight trend of increment in Atg5 $^{flox/flox}$; nestin-*Cre* cerebella.

Moreover, we analysed the CMA pathway in the cerebellum of *Atg5* $^{flox/flox}$; nestin-*Cre* mice and control at six and eight weeks of age determining the protein levels of LAMP-2A and Hsc70 by western blot (Figure 4.24). LAMP-2A levels in *Atg5* $^{flox/flox}$; nestin-*Cre* cerebella were slightly more elevated than in control, while the Hsc70 levels quantification did not reveal any difference

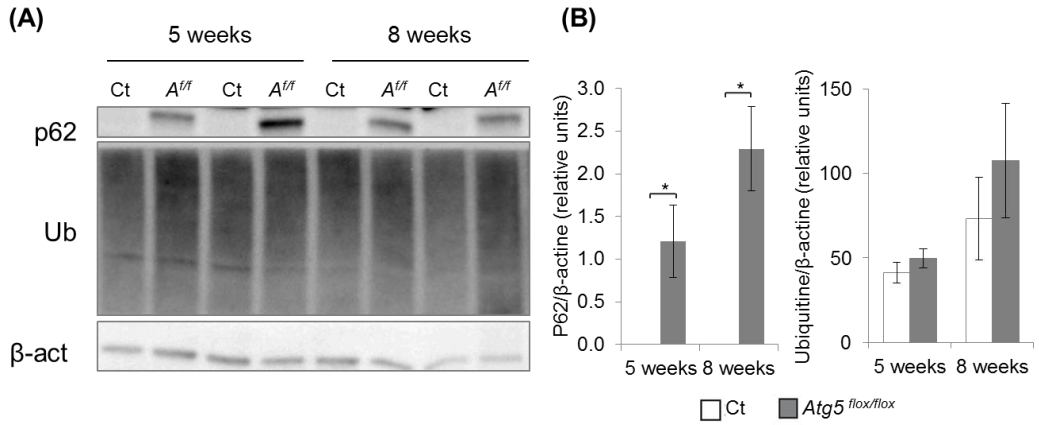

Figure 4.23. Determination of p62 and ubiquitine levels by western blot in *Atg5* $^{flox/flox}$; nestin-*Cre* mice at 5 and 8 weeks of age. Western blot (A) and quantification (B). Ct: control; *Atg5* $^{f/f}$: *Atg5* $^{flox/flox}$; nestin-*Cre,* ub: ubiquitine. ($p<0.000$).

between control and *Atg5* $^{flox/flox}$; nestin-*Cre* animals, as there was a high variability among samples. This could be explained as Hsc70 is an important player in CMA but it is not limiting of the pathway, and it is also involved in other processes as protein refolding (Kaushik and Cuervo, 2012). To relate the increase of LAMP-2A and p62 to a location, we performed an

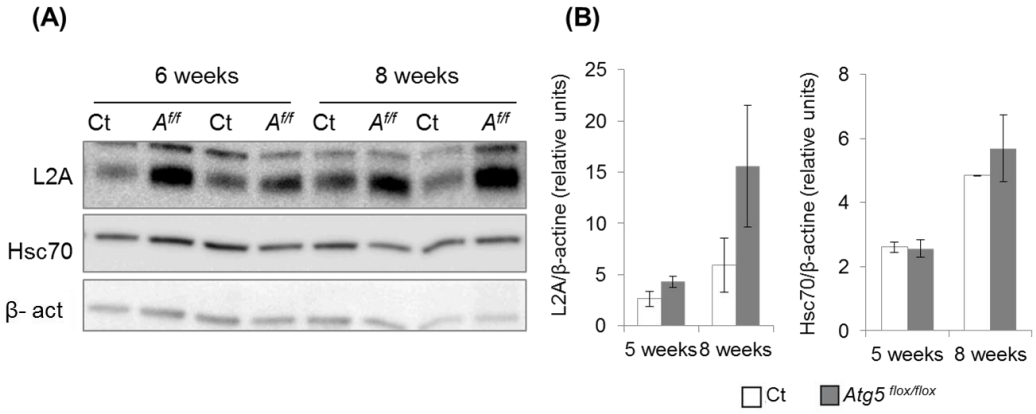

Figure 4.24. Determination of LAMP-2A and Hsc70 levels by western blot in Atg5 $^{flox/flox}$; nestin-*Cre* mice at 6 and 8 weeks of age. Western blot (A) and quantification (B). Ct: C57-Bl6; F+: *Atg5* $^{flox/flox}$; nestin-*Cre*, L2A: LAMP-2A, β-act:

immunostaining of both proteins (Figure 4.25). We found that LAMP-2A was mainly placed in Purkinje cells and that there was a different staining pattern among the strains. Control animals presented a diffuse pattern of LAMP-2A occupying all the cytoplasm, whereas the *Atg5* $^{flox/flox}$;

nestin-*Cre* Purkinje cells showed a perinuclear punctate pattern, hinting a lisosomal location. This pattern would explain why, even if an increase in LAMP-2A levels was signalled by the westernblot, it was not significantly different. The detection of p62 in control animals was almost null, but there were great accumulations in the granule cells of *Atg5* $^{flox/flox}$; nestin-*Cre* mice among the whole layer in the form of discrete dots.

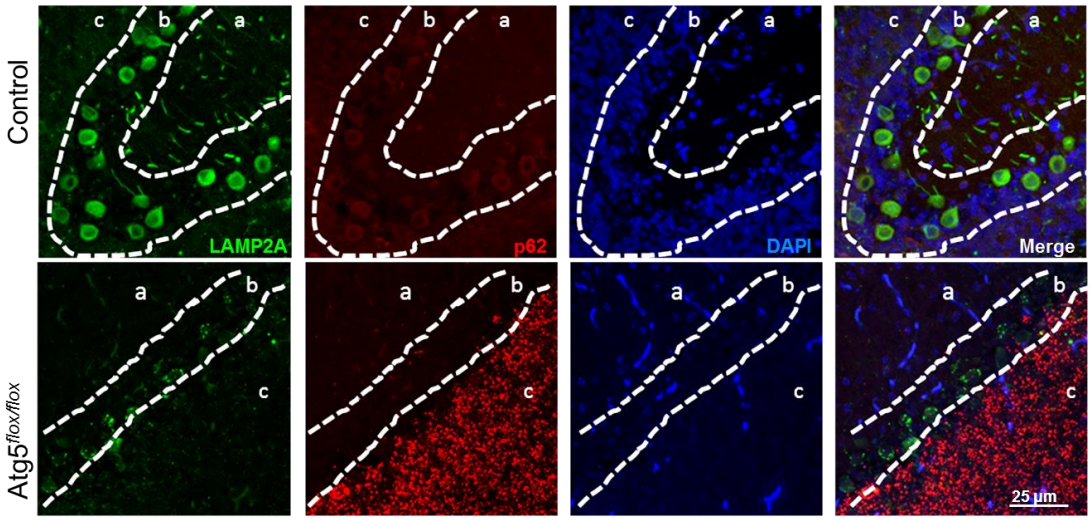

Figure 4.25. Presence of LAMP-2A and p62 in cerebellum (Purkinje and granular layers) of C57-Bl6 and *Atg5*$^{flox/flox}$; nestin-*Cre* mice at 7 weeks of age. a: molecular layer, b: Purkinje layer, c: granular layer.

Therefore, in cerebellum in the absence of macroautophagy, Purkinje cells, which are also more resistant to the consequent degeneration than granule cells, present high levels of LAMP-2A localized in perinuclear puncta and do not accumulate p62, whereas granule cells, which are more sensitive to the neurodegeneration in this case, present lower levels of LAMP-2A, a different pattern of emplacement and a prominent accumulation of p62 in a dotted pattern. Indirectly, these results could be supporting the compensation mechanism between macroautophagy and CMA observed in the retina, and remarking a cell-dependent implication of the mechanism.

4.1. QUANTITATIVE TOOLS FOR AUTOPHAGY AND APOPTOSIS DETERMINATION USING IMAGE ANALYSIS

In collaboration with our group, the company Wimasis (www.wimasis.com) has developed two modules for quantitative analysis of autophagy and apoptosis assays: WimAutophagy and WimApoptosis, respectively. This project was carried out in the frame of an INNPACTO project from MINECO that favours public-private partnership in research. They are based on the high-end image-processing algorithm developed by the company Wimasis, which is a robust and flexible algorithm that performs an accurate analysis of cell imaging in a short time, and adapted with the expertise of our laboratory on autophagy and apoptosis images, which will allow our laboratory to analyse most of our experiments with an easy and accurate tool.

The modules are accessible to the scientific community through the website thus, there is no need to install any software and so, no need to have any hardware to support it. For the analysis, users only have to upload the images on the Wimasis cloud and they will receive the results in a few hours. Therefore, users do not need any knowledge about the handling of the module and neither to spend the time processing the images.

For all these reasons, the developed algorithms represent tools to improve research on the mentioned cellular processes. Therefore, they are promising instruments for neurodegenerative studies as they provide the most objective and accurate analysis of autophagy and apoptosis images and because it does not require the investment of time on software handling, but just the time to analyse the data.

4.1.1. Autophagy image analysis: WimAutophagy module

This module has been developed to provide a reliable and fast tool for quantification of autophagy on microscope images. WimAutophagy has been probed to work both with epifluorescence and confocal images. Also, it is able to recognize different LC3 labelling, as transfected GFP-LC3 or LC3 immunostaining, on different cell types and even tissues, as it will be detailed in the next sections. Furthermore, as it is a flexible algorithm, it can also recognize other markers as LAMP-2A, hallmark of CMA, which suggests the possibility to apply the module to study other organelles with similar size to autophagosomes as endosomes or peroxisomes, for instance.

4.1.1.1. WimAutophagy algorithm description

In this section we will detail the steps of processing followed by the module. The introduced images should be RGB, with a constant size in all the images and could present a range of formats (tif, jpg…). The images also should present a clear signal delimiting the autophagosomes from a dark background and the nuclei need to be labelled too. Some examples of adequate images for the module are shown in Figure 4.26. Both images are from HeLa cells transfected with GFP-LC3. Figure 4.26- A was acquired by epifluorescence

microscopy and it is perceptible a punctate pattern but also a diffuse cytoplasmic signal, while B image was acquired by confocal and presents a clear punctate pattern. Both types of images are suitable for the module, as well as antibody or other LC3 labeling.

The analysis of the images takes part in three phases: pre-processing, processing and data merge.

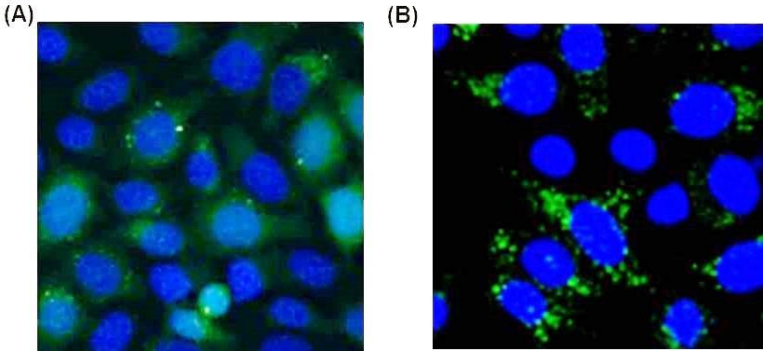

Figure 4.26. Example of suitable images for the analysis with WimAutophagy module of GFP-LC3 transfected cells. (A) epifluorescence image; (B) confocal image.

a) Pre-processing: determination of autophagosome size

Previous to the analysis itself, the algorithm defines a mean size of the autophagosomes in pixels, as it is the object of study and it can vary widely between cell types and treatments. In case that the user previously knows the mean size of the autophagosomes in the analysed system, the algorithm offers the possibility to include it, avoiding the pre-processing step. The establishment of a mean size of APs will be helpful for guiding the next processing steps.

Thus, during the pre-processing the module detects the labelling for APs in a perimeter around the nuclei (called “cytoplasmic region” and stablished by statistical calculations) and determines the area in pixels occupied by the autophagosomes signal. The steps to calculate the area of autophagosomes are:

- *Recognition of the puncta labelled for LC3 and determination of the area in pixels* of the puncta in each image.
- *Estimation of a probability density function of the areas.* Usually, there are two distinguishable populations as shown in Figure 4.27. The population with smaller area corresponds to isolated APs but, as a pre-processing step, it also includes noise signal with small size. The second population, with larger area, includes several autophagosomes grouped (named here as clusters).
- *Calculation of the estimated area of AP based on the obtained populations*. The estimated area of the autophagosome will be the mean value of the two peaks (red line in panel (A)). In this way, the noise signal is avoided, allowing the algorithm to achieve a more real estimation, which will render a better identification of APs in posterior steps. Puncta with an area 1.5 times the estimated AP area will be considered as clusters of APs.

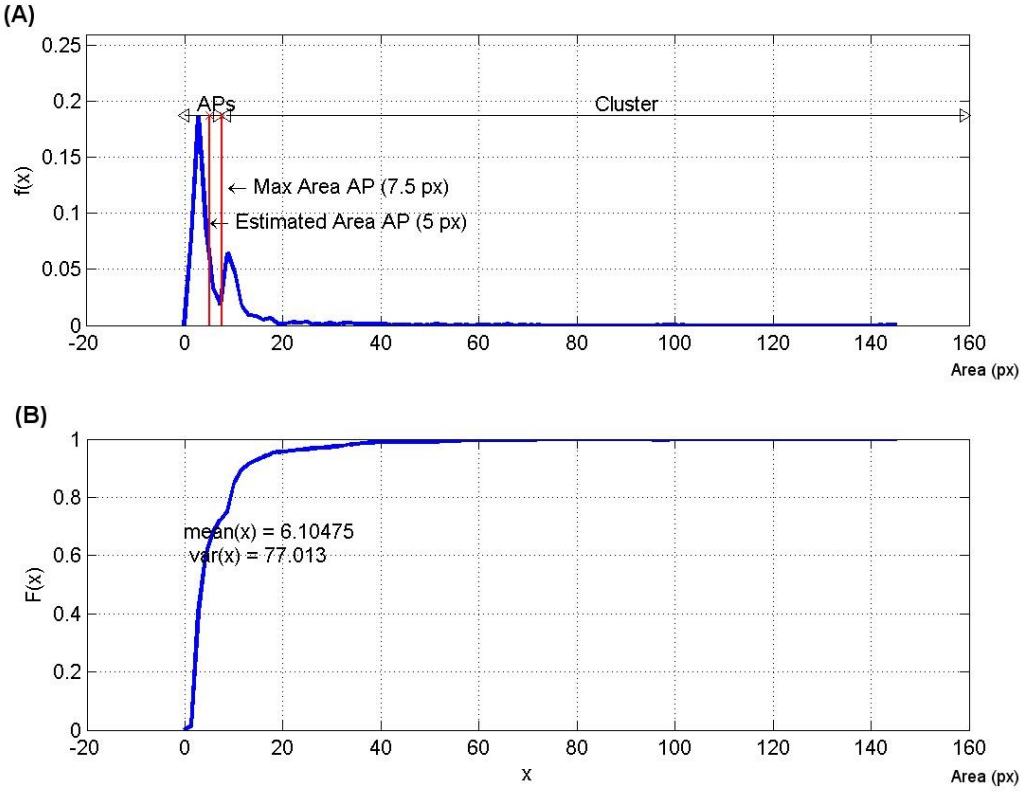

Figure 4.27. Analysis of the population of autophagosomes and its size. (A) Estimated probability density function, were X axis represents the area in pixels (px) on the puncta (AP size) and Y axis represents the function of the frequency of each AP size. (B) Cumulative distribution function. Max area AP: maximum area of autophagosomes.

Processing

Once the signal is identified on the images and the mean AP size is estimated, the module performs seven steps for filtering, identification of APs and assignment of the APs to their nuclei, for subsequent quantification.

1. Filtering of input images (Standardization):

Before image quantification, the module performs some modifications to optimize the analysis in the next steps:

- split the input image into the different colour channels (RGB, Red Green Blue)
- standardize image size
- increase contrast
- correct not uninform illuminations

2. Nuclei recognition:

The algorithm detects the nuclei of each cell and delimits them with a red perimeter (Figure 4.28).

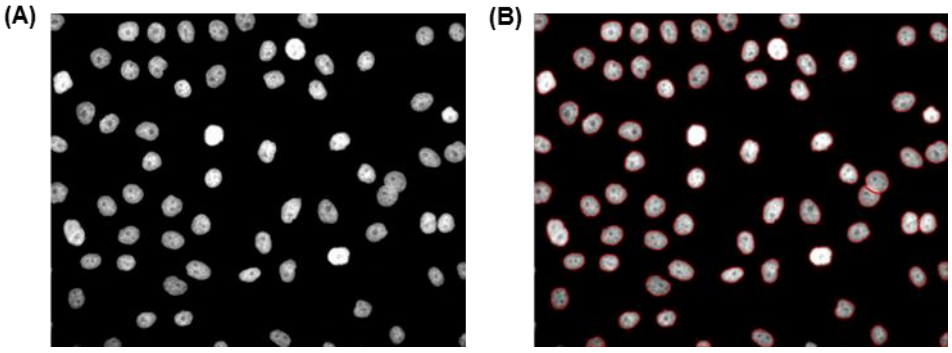

Figure 4.28. Nuclei recognition example. Left image (A) shows the original RGB file of the nuclear staining and right image (B) shows the recognized nuclei delimited with a red line.

3. Cytoplasm recognition:

The algorithm establishes an area of interest around each nucleus for subsequent search of autophagosomes and it is delimited with a red line (Figure 4.29). Besides, the algorithm is able to detect other cytoplasmic signal that can help to define the area of interest, for instance, the diffuse cytoplasmic GFP-LC3 signal or a transfection reporter. In the case of a transfection reporter, the algorithm could also sort the cells by positive or negative for transfection and limit the study exclusively to transfected cells, if desired.

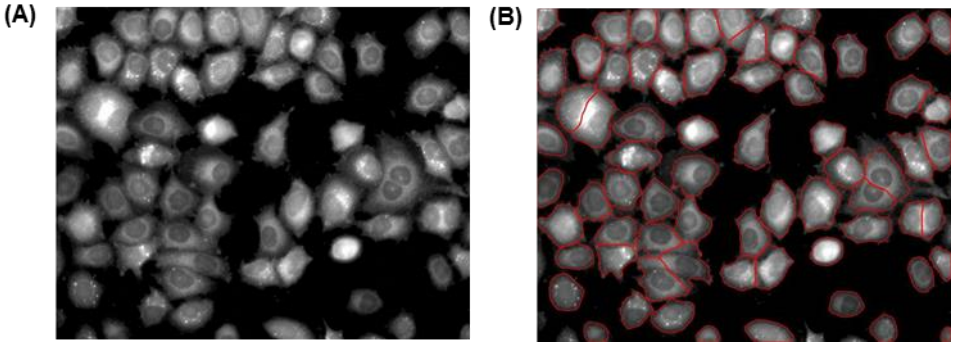

Figure 4.29. Cytoplasm recognition example. Left image shows the original RGB file of GFP-LC3 labelling and right image shows the detected cytoplasm delimited with a red line. It encircles the area delimitated by diffuse cytoplasmic GFP-LC3 signal

4. Complex filtering of LC3 images:

It consists on the elimination of the background signal. It is especially relevant in the case of cells transfected with GFP-LC3, as it generates a strong background with the GFP diffuse cytosolic signal, which requires a more exhaustive filtering procedure. Figure 4.30 shows a representative transformation of an original image to the filtered one.

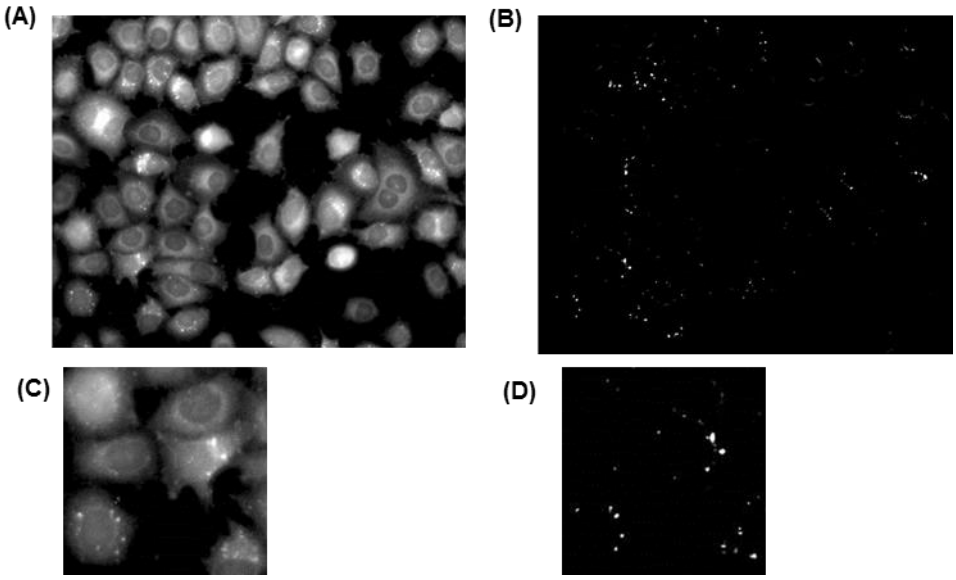

Figure 4.30. LC3 signal filtering. (A) Original RGB file of the GFP-LC3 labelling channel. (B) image after filtering GFP-LC3 dots. (C) and (D) magnifications of A and B, respectively.

5. Puncta recognition:

At this point, the cytoplasm area is filtered, only containing dots over a black background. The new image is subjected to iterative techniques of segmentation of intensity, identifying the brightest dots in the first iterations and the less intense dots in later iterations.

Only the detected signals with more than 20% of mean intensity of the cytoplasm are considered positive dots. The mean intensity of the cytoplasm is calculated with the original image, replacing the intensity of the autophagosomes by the mean intensity of its perimeter.

Images with many big sized clusters of APs with high and uniform intensity could not be correctly quantified by the algorithm, as they could be eliminated during the filtering process.

6. Relation of puncta to cells and cell indexing:

All the detected APs are assigned to a particular nucleus according to the previous cytoplasm recognition. Also, all the nuclei in the image are labelled with a consecutive number for cell identification (Figure 4.31). Cells whose nuclei are not completely inside the image will not be analysed.

7. Determination of isolated APs and clusters:

Depending on their size, two populations of APs can be distinguished: isolated APs and clusters of APs, which are identified with different colours, as shown in Figure 4.31, isolated APs are labelled in different colours (black arrows in Figure 4.31(B)) and clusters are labelled) in orange with blue perimeter (white arrows in (Figure 4.31 (B)).

For quantification, the populations can be considered separately or not. In the first case, the number of APs included in the clusters is estimated by dividing the total area of each cluster by the estimated AP size and thus, *the total number of estimated APs* per cell is the sum of the isolated APs and the estimated APs in clusters. In the second case, all dots are equally considered and they are quantified as *puncta per cell*. Both quantifications reveal important information that will be commented in next sections.

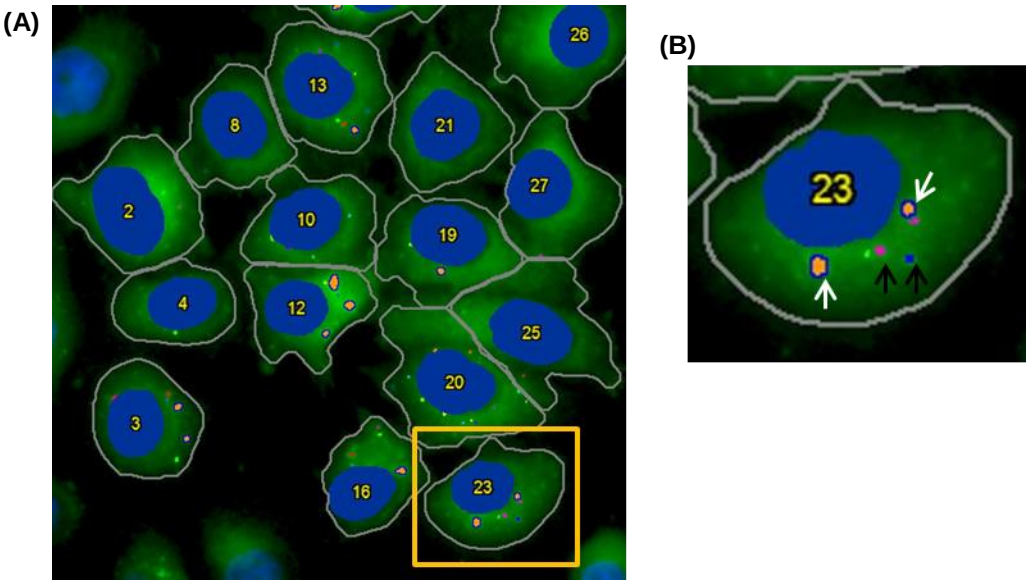

Figure 4.31. (A) Image of GFP-LC3 cells after the processing with the Wimasis algorithm, (B) magnification of a cell delimited with a grey line and with the blue mask representing the nucleus. In its cytoplasm, dots are classified as isolated APs (different colors, indicated with black arrows) and clusters (orange with blue perimeter, indicated with white arrows).

b) Data merge

All the obtained data is merged and included in two types of files with CSV format (Comma Separated Value): individual files for each image and a file with the overall data of all the images per experiment. Figure 4.32 shows an example of a CSV file with an individual image data. Lines 1, 2 and 3 provide the overall data of the analysis for that image that later will be incorporated to the summary file. From line 5, individual cell metrics are displayed (all the parameters per cell organized in one row per each cell). Here we detail the data on each column:

1. **ID:** cell number identification for cell indexing (column A)
2. **Cytoplasm Area [px]**: area in pixels of the cytoplasm. This value is only calculated for epifluorescence analysis (column B)
3. **Nucleus Area [px]:** area in pixels of the nucleus. (column C)
4. **Number Isolated APs (A):** number of isolated autophagosomes. Number of autophagosomes whose area in pixels is lower than the maximum area of autophagosomes established (column D).
5. **Number Clusters (B):** number of autophagosomes whose area is higher than twice the estimated AP area in pixels (column E).

	A	B	C	D	E	F	G	H	I	J	K
1	Autophagy Assay Key Metrics										
2	No. Cells	Estimated Area AP [px]	Mean AP per cell	Mean Puncta per cell	Mean AP Intensity	Mean Nucleus Area [px]	Std AP per cell	Std Puncta per cell	Std Nucleus Area [px]	Total Area AP [px]	
3	32	8	4.63	3.97	0.2	2538	3.35	3.06	684	847	
4											
5	Individual Cell Metrics										
6	ID	Citosol Area [px]	Nucleus Area [px]	Number Isolated APs (A)	Number Clusters (B)	Number Estimated APs in Cluster (C)	Puncta per cell (A+B)	Total Number Estimated APs (A+C)	Total AP Area [px]	Mean Intensity of Total AP Area	Total Area Cluster [px]
7	1	608	3203	3	0	2	3	5	8	0.21	0
8	2	66	1510	0	1	0	1	0	19	0.24	19
9	3	136	2227	5	0	0	5	5	11	0.17	0

Figure 4.32. Example of CSV file for a single image. Top part shows the Autophagy Assay Key Metrics that summarize the main parameters calculated for each cell. Bottom data shows de Individual Cell Metrics, detailed in

6. **Number Estimated APs in Cluster (C):** this value is calculated by dividing the area of each cluster by the estimated area of APs. Values are rounded (column F).

$$Number\ Estimated\ APs\ in\ Cluster = {Cluster\ area\ [px]}/{Estimated\ AP\ area[px]}$$

7. **Puncta per cell (A+B):** total number of detected dots in the cell without distinguishing from single or clustered autophagosomes (column G).

$$Puncta\ per\ cell = Number\ of isolated\ APs + Number\ of Clusters$$

8. **Total Number Estimated APs (A+C):** total number of autophagosomes in the cell, obtained by summing the isolated APs and the estimated number of autophagosomes in cluster in the cell (column H).

$$TotalNumberEstimatedAPs = NumberIsolatedAPs + NumberEstimated\ APs\ in\ cluster$$

9. **Total AP Area [px]:** sum of the area in pixels occupied by all autophagosomes detected in the cell (column I).

$$TotalAPArea = \sum Area_{APi}$$

10. **Mean Intensity of Total AP Area:** mean intensity of the autophagosomes detected in the cell (column J).

$$Mean\ Intensity\ of\ Total\ AP\ Area = \frac{1}{N}\sum Intensity\ of\ Total\ AP\ Area_i$$

The Order Summary file (Figure 4.33) displays the conclusive parameters of each image in sucesive lines. The information of each column is detailed below.

	A	B	C	D	E	F	G	H	I	J	K	L
1			Autophagy Assay Key Metrics									
2	File Name		No. Cells	Estimated Area AP [px]	Mean AP per cell	Mean Puncta per cell	Mean AP Intensity	Mean Nucleus Area [px]	Std AP per cell	Std Puncta per cell	Std Nucleus Area [px]	Total Area AP [px]
3	E024/E024_01_01_24H		87	8	1.75	1.56	0.19	2521	2.24	2.12	590	855
4	E024/E024_01_01_6H		32	8	4.63	3.97	0.2	2538	3.35	3.06	684	847
5	E024/E024_01_02_24H		70	8	1.56	1.37	0.23	2473	2.16	2.08	622	602

Figure 4.33. Examples of CSV file of a summary sheet. The Autophagy Assay Key Metrics summarize the main parameters calculated for each image.

1. **No. Cells:** total numbers of cells in the image (column A).

2. **Estimated Area AP [px]:** estimated area of autophagosomes in pixels in the image or AP size (column B).

3. **Mean AP per cell:** mean of the total number of estimated APs per cell (column C).

$$Mean\ AP\ per\ Cell = \frac{1}{N}\sum Number\ Estimated\ APs_i$$

4. **Mean Puncta per cell:** mean of puncta per cell (column D).

$$Mean\ Puncta\ per\ cell = \frac{1}{N}\sum Puncta\ Per\ Cell_i$$

5. **Mean AP Intensity:** mean intensity of autophagosomes. Only the cells with some autophagosomes are selected to calculate this value (column E).

$$Mean\ AP\ Intensity = \frac{1}{N}\sum Intensity\ AP_i$$

6. **Mean Nucleus Area [px]:** all cells are included to calculate this value (column F).

$$Mean\ Nucleus\ Area = \frac{1}{N}\sum Area\ Nucleus_i$$

7. **Std (Standard deviation) AP per cell:** standard deviation of total number estimated APs (column G).

$$Std\ AP\ per\ cell = \sqrt{\frac{1}{N}\sum (AP\ Per\ Cell_i - Mean\ AP\ PerCell)^2}$$

8. **Std Puncta per cell:** standard deviation of puncta per cell (column H).

$$Std\ Puncta\ per\ cell = \sqrt{\frac{1}{N}\sum (Puncta\ Per\ Cell_i - Mean\ Puncta\ Per\ Cell)^2}$$

9. **Std Nucleus Area:** standard deviation of nuclei area (column H).

$$Std\ Nucleus\ Area = \sqrt{\frac{1}{N}\sum(Nucleus\ Area_i - Mean\ Nucleus\ Area)^2}$$

4.1.1.2. Validation of the WimAutophagy module and examples of data analysis

Through several cases of study we validated the detection of APs performed by the algorithm, its robustness and flexibility. The cases of study will also serve to explain in better detail the parameters provided by the module.

For the validation of the accuracy and robustness of the algorithm on APs detection, the optimal test would be a comparison between manual counting of APs and the counting performed by WimAutophagy on the same images. However, due to the practical impossibility, we performed a visual contrast between the original images and the processed ones in at least the 30% of the cells on the images from the experiments presented below.

We first validated the detection of APs by the module WimAutophagy for LC3 immunolabeling with confocal imaging, as it is a clean signal. We used 661W control cells (overexpressing the unrelated protein PGK as control transfection) and Atg7 KD cells (with siRNA silencing Atg7), in order to have a negative control, as they cannot accomplish autophagosome formation. Transfected cells present a GFP transfection reporter that generates a green cytoplasmic signal. Examples are shown on Figure 4.34 A and C, where the red channel corresponds to LC3 immunolabeling and green channel to the GFP reporter. Image A shows a control cell with its corresponding green and red channels, revealing the presence of APs in the cytoplasm, and Figure 4.34 B corresponds to the same image after the processing with WimAutophagy. It

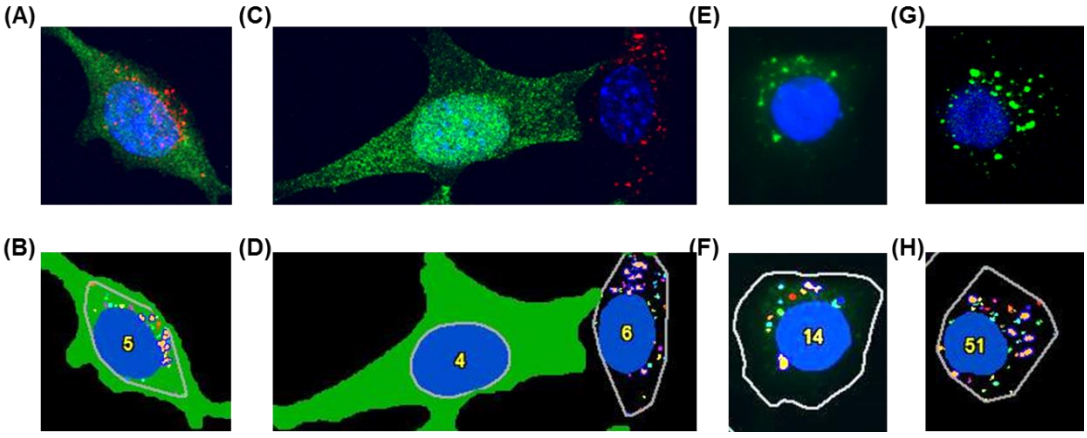

Figure 4.34. Representative images of the detection performed by the WimAutophagy module under different circumstances. (A,C,E,G) show original images, (B,D,F,H) show the same images after processing: (A-B) HeLa cells transfected with GFP-LC3 imaged with epifluorescence microscopy, (C-D) HeLa cells transfected with GFP-LC3 imaged with confocal microscopy, (E-F) 661w cells PGK with GFP transfection reporter (green) and LC3 immunostaining (red) imaged with confocal microscopy, (G,H) 661w cells: 4: Atg7 KD cell with GFP transfection reporter (green), 6: non-transfected cell, both were immunostained for LC3 (red). Blue channel corresponds to nuclear DAPI staining.

shows the clear recognition of the nucleus, with the pertinent numeration, and a highly accurate detection of APs, with a proper assignation of colours (varied colours for individual APs and orange with blue perimeter for clusters). Moreover, C picture shows two cells, one of them with green GFP reporter, that in this case indicates transfection for Atg7 KD. Thus, the green cell is unable to perform autophagy as it indicates the absence of red pixels. However, the aside cell lacks the green cytoplasmic signal, indicating that it was not transfected and thus, it is a wild-type cell, as the prominent presence of red autophagosomes indicates Figure 4.34 D shows that, indeed, in the cell number 4 (green) the algorithm is not detecting any APs, while it does on cell number 6, presenting that the algorithm is performing a precise detection of the LC3 signal and that it is not generating “false positives”.

We also validated the detection of LC3 signal for GFP-LC3 labelling and under different microscopy conditions (epifluorescence and confocal) using HeLa cells transfected with GFP-LC3. Figure 4.34 E and G show an example of both cases, respectively, and F and H show the correspondent detection of APs by the module. It is noticeable that epifluorescence microscopy generates a green cytoplasmic silhouette that is avoided by confocal microscopy. This silhouette makes the algorithm to stablish a stricter filtering step of epifluorescence images, resulting in a lower detection of APs and final counting, compared to confocal images, as shown in F and H. But, in both cases, the algorithm performs a robust and accurate APs detection.

Therefore, we have validated that the algorithm performs an accurate detection of APs, as no false positives are generated, and also that it is robust, as the algorithm is able to detect APs even in not optimal imaging conditions.

- **Case of study 1: following macroautophagic activity with WimAutophagy with different types of imaging (epifluorescence and confocal microscopy).**

For a better validation of the robustness of the algorithm, we compared images from

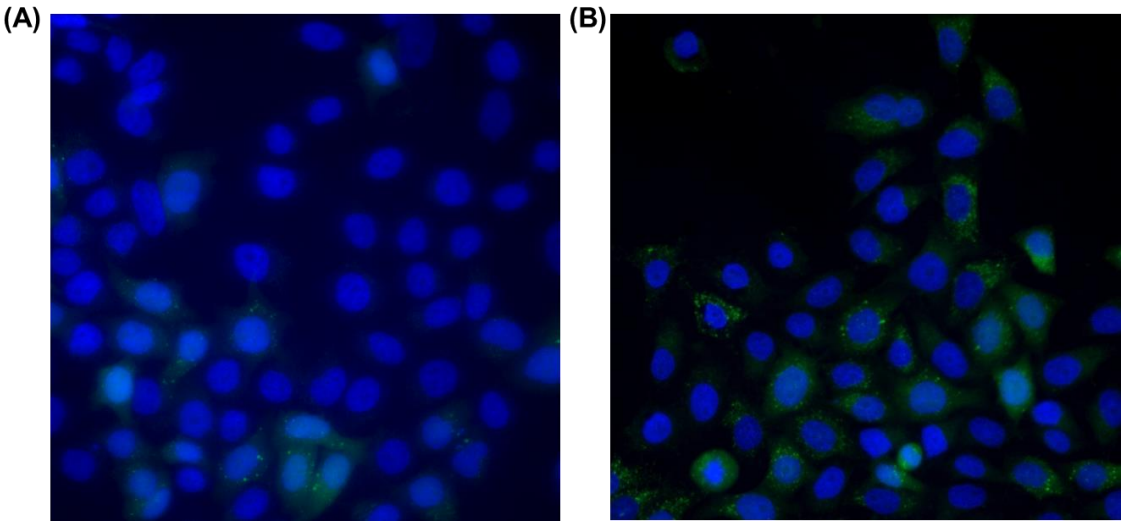

Figure 4.35. Representative images of epifluorescence microscopy processed with WimAutophagy module of HeLa GFP-LC3 cells cultured in control conditions (A) or with HCQ (B).

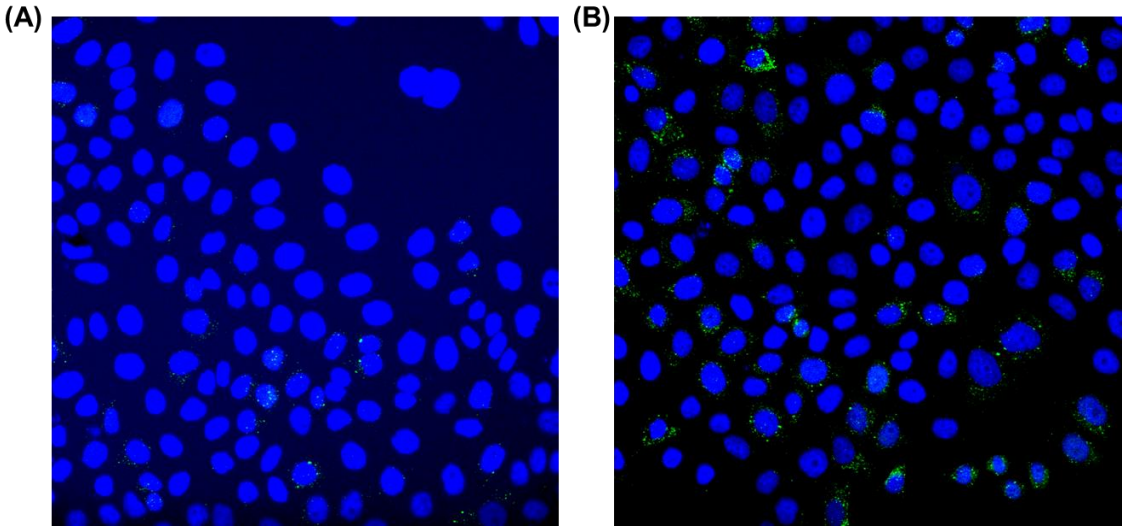

Figure 4.36. Representative images of confocal microscopy processed with WimAutophagy module of HeLa GFP-LC3 cells cultured in control conditions (A) or with HCQ (B).

epifluorescence and confocal microscopy obtained from same experiment. Also, to complete the explanation of the parameters provided by the algorithm, we will compare the most relevant in for both imaging conditions.

The experiment consisted on GFP-LC3 transfected HeLa cells cultured overnight (16h) in DMEM and, for the last three hours of culture, hydroxychloroquine (HCQ) 30mg/mL was added, a lysosomal inhibitor to block autophagic flux. Representative images of the experiment acquired with each type of microscopy are shown in Figure 4.35 and 4.36. With both imaging it is appreciable an increase of GFP-LC3 dots in the presence of HCQ (image (B) of both Figures). Also, comparing the two Figures it is appreciable the mentioned difference in the definition of both microscopies. Analysing the date will illustrate how this influences the final result.

Determination of the total area

To test the consistency of the detection of the algorithm, we compared the numeric results in both cases for the rawest parameter: *total AP area*, the detection performed by the algorithm of the LC3 labelled pixels. Results in Figure 4.37 clearly show the increase of LC3 labelling in the presence of HCQ in both graphics, (A) for epifluorescence and (B) for confocal. It is remarkable that confocal results present a higher scale, evidencing the lower quality of the epifluorescence images and the stricter filtering applied to them.

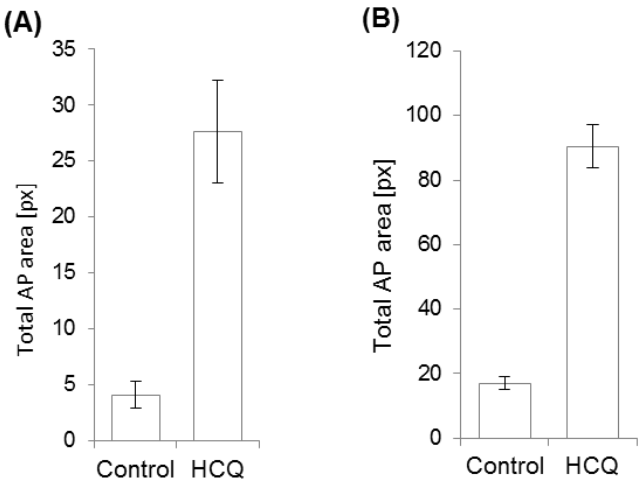

Figure 4.37. Graphic representation of the Total AP area [px] obtained with WimAutophagy module from: (A) epifluorescence images and (B) confocal images of HeLa GFP-LC3 cells cultured in control and with hydroxychloroquine (HCQ). ($p<0.000$ in both Figures).

Thus, we can conclude that the usage of images from different acquisition does not result in a differential analysis. Even if the detection conditions were different, the algorithm was able to detect the autophagosomes correctly and perform a proper quantification of the total area AP in conditions of low and high density of autophagosomes per cell. Therefore, we can say that the obtained results are analogous for both types of microscopy, highlighting the robustness of the developed algorithm.

Definition of the autophagosome size

During the pre-processing step, the algorithm estimates a mean size of APs for all images, which is indicated on the CVS files. Before the pre-processing, the user can also fix the AP size, if known. In any case, it is recommendable for a better understanding of the studied system to perform both analyses, as they are complementary. It is also possible to run the module estimating a mean size for all the treatments or a different size for each treatment.

The *autophagosome size* could be a relevant parameter when comparing different treatments, cell lines/tissues and their metabolic state, to better follow the autophagic activity, not only studying the changes of the number of autophagosomes generated but also of their size.

In this case of study, to illustrate its repercussion, we analysed the epifluorescence images without fixing AP size and confocal images with a fixed AP size of 8 pixels for all the images (based on previous analysis).

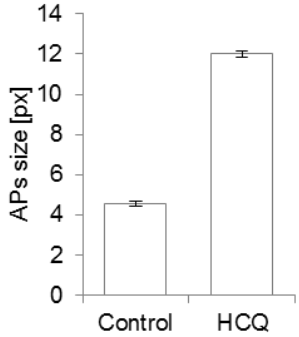

Figure 4.38. Graphic representation of the autophagosome size in pixels estimated by WimAutophagy in HeLa GFP-LC3 cells cultured in control conditions and with hydroxychloroquine (HCQ). ($p<0.000$).

For epifluorescence, the algorithm defined a mean AP size for each treatment as shown in Figure 4.38, where we can observe that HCQ induces an increment of AP size, showing that the blockage of the fusion of lysosomes and autophagosomes can affect the size of autophagosomes in this cell line.

Estimating the number of autophagosomes

To complete the validation and the data interpretation, we compared the parameters *puncta per cell* and *estimated APs per cell* for both imaging methods, and the repercussion of fixing or not the AP size. These parameters are the most sophisticated data provided by the algorithm, and the AP size is determining for their interpretation.

The quantification obtained fixing the APs size is presented in Figure 4.39-A. We can observe that the number of APs, quantified both as puncta or estimated APs per cell, is higher in HCQ treatment than in control, indicating a proper identification of the LC3 puncta. In this case we observe that the detected dots are mainly individual APs, as the quantification of the total estimated APs does not present an increase in the final number, which agrees with the fact that confocal microscope attains higher resolution.

In the example without fixing the APs size (Figure 4.39-B), the quantification of both parameters renders an increase of APs per cell in the culture with HCQ, validating the detection performed by the algorithm. In this case, there is neither a remarkable change between the quantification by puncta or estimated APs, but here it is due to the difference in AP size between both treatments. As seen in the previous section, HCQ is the treatment with more puncta and also with bigger size puncta, making that the estimation of the APs per cell (where the area of the clusters is divided by the estimated size of individual APs) results in a similar number to the puncta.

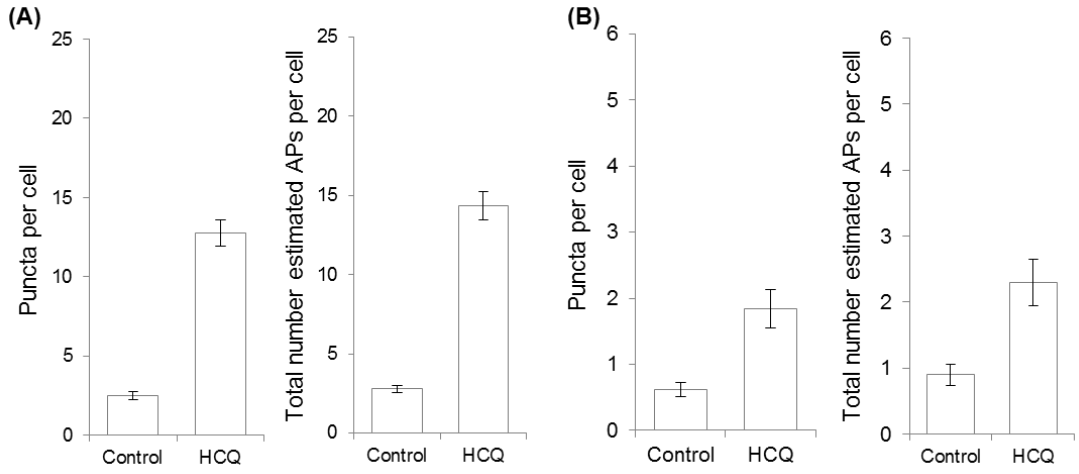

Figure 4.39. Graphic representation of the quantification of puncta per cell and total number of estimated APs per cell for images prefixing the AP size (A) and images without fixing it (B). ($p<0.000$).

Therefore, we have shown that the WimAutophagy module is able to work with images with different degrees of definition, acquired by different microscopy, and to provide analogue results for them, showing, thus, that it is an accurate algorithm, and robust, as these results are sustained for a representative number of experiments.

- **Case of study 2: evaluation of CMA in cell lines using WimAutophagy**

For examining the flexibility of the algorithm, we analysed images of cells immunolabeled for LAMP-2A, the CMA hallmark, as LAMP-2A positive lysosomes present a similar size to autophagosomes.

We used the 661W cell line transfected with siRNA lentiviral vectors to decrease the expression of LAMP-2A coupled to GFP to visualize transduced cells. As well, we also transfected them with a non-silencing lentiviral vector expressing the unrelated protein PGK coupled to GFP, as a control of transfection. Cells were treated with lysosomal inhibitors ammonium chloride and leupeptin (N/L) for 24h and, posteriorly, stained with LAMP-2A antibody. Images were acquired by confocal microscope and analysed with the WimAutophagy module. “APs” (in this experiment called *CMA+ lysosomes*) size was pre-fixed before the analysis in 8 pixels, based on previous analysis. Only GFP + cells were included in the analysis, to avoid non-transfected cells.

First, we checked the detection of the CMA+ lysosomes by the module. Figure 4.40 (left) shows an example field of 661W LAMP-2A KD cells, with transfected cells (green cytoplasm) and one non-transfected cell (dark cytoplasm). Cells were immunostained for LAMP-2A (red channel) but only the non-transfected cell shows CMA+ lysosomes. Figure 4.40 (right) shows the same image after the processing with WimAutophagy, with nuclei coloured in blue and numbered with the cell ID, and CMA+ lysosomes labelled in the pertinent colours according to their size (single

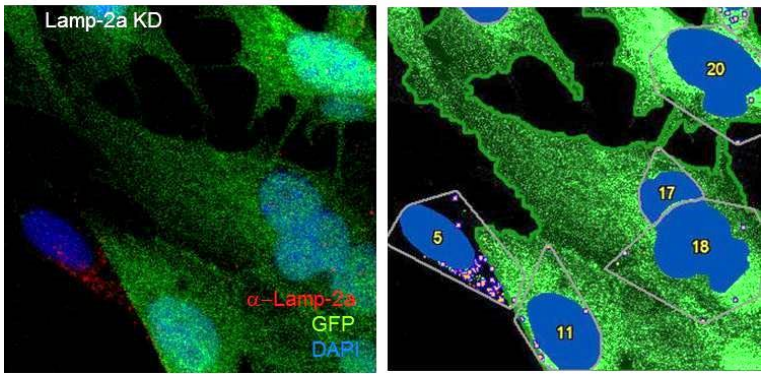

Figure 4.40. Left image represents 661W Lamp-2a KD with transfection GFP reporter and anti-LAMP-2A immunostaining. Right panel shows the same image after the module processing.

APs labelled in different colours and clusters in orange with blue perimeter). It is perceptible at a glance that GFP+ cells present scarcely any CMA+ lysosome while the non-transfected cell does, validating the detection of the algorithm for other organelles with similar size to autophagosomes too.

Then, we checked the quantification performed by WimAutophagy of the CMA+ lysosomes. Figure 4.41 shows representative images of the experiment (A) and their quantification for total CMA+ lysosomes area, puncta per cell and total estimated CMA+ lysosomes (B). On the panel (A) it is perceptible that control cells present CMA+ lysosomes in basal conditions and that their number is increased in the presence of lysosomal inhibitors, while LAMP-2A KD cells scarcely present any CMA+ lysosome. The quantification of CMA by any parameter reflects the differences appreciated on the images. It is noteworthy that the quantification was exclusively performed with the transfected cells in both cases and even though there is a minimal amount of CMA+ lysosomes, which is probably because the gene silencing is only a knockdown but not a knockout procedure. In any case, we can affirm that the algorithm is flexible enough to perform the quantification of other organelles with similar size to autophagosomes.

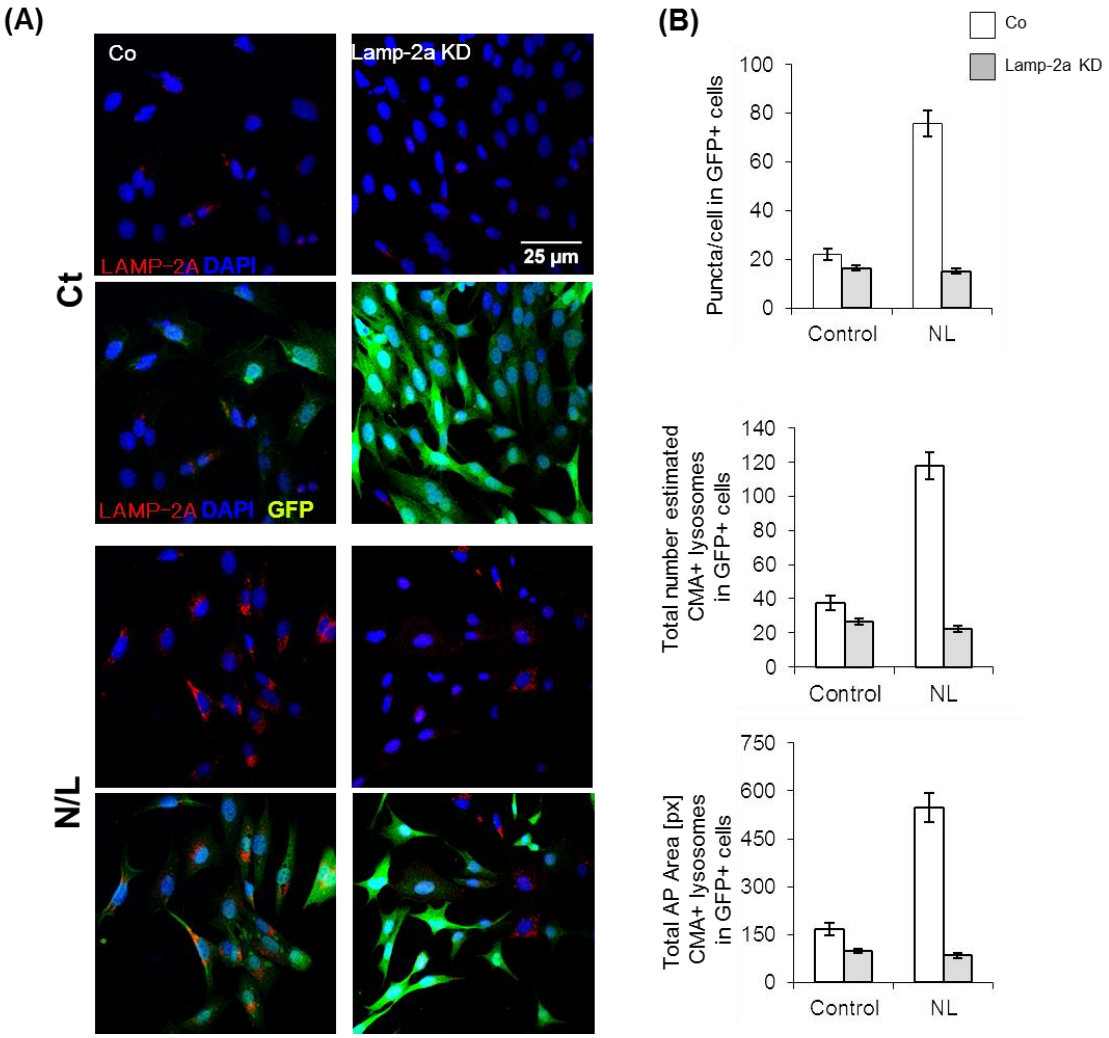

Figure 4.41. (A) Representative images of 611W control cells and Lamp-2a KD untreated and after N/L treatment. Top panels show only DAPI and LC3 staining. Bottom panels show also GFP signal to identify transfected cells. (B) Graphics for Puncta/cell, Total number of estimated APs and Total AP area (px) from the

- **Case of study 3: following macroautophagic activity in flat-mount retina with WimAutophagy**

In this experiment, we analysed the accuracy of the algorithm in flat-mount retinas of GFP-LC3 mice with C57/Bl6 background.

We focused on the photoreceptor layer, as they are the first affected in many retinopathies (Cuenca et al., 2015) and, specifically, we focused on the inner segment. We selected this region because, according to bibliography (Reme et al., 1999), the IS is an area enriched in APs. However, the obtained images on flat-mount retinas (Figure 4.42) were not appropriate for the module as the APs were hardly differentiated from the background fluorescence of GFP, even with confocal acquisition. Furthermore, even if the APs could be precisely identified, they should be assigned to a cell and that, as the nuclei were not in the same image, was not possible. Thus, we moved onto the outer nuclear layer, where the nuclei are visible, although they are surrounded by a small part of cytoplasm (Figure 4.43).

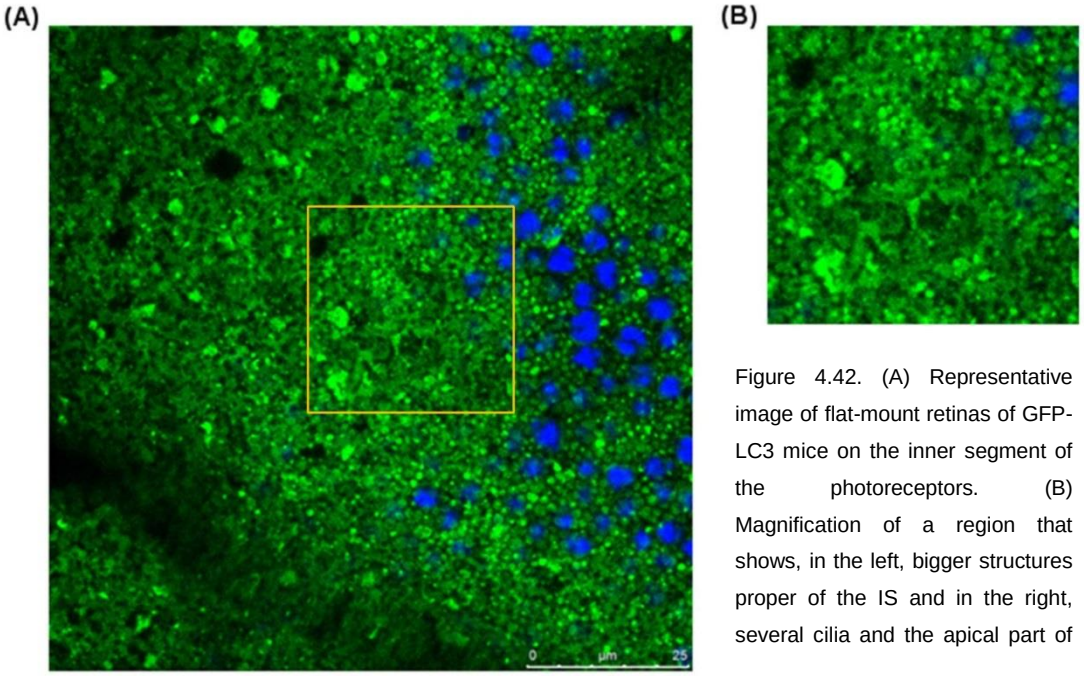

Figure 4.42. (A) Representative image of flat-mount retinas of GFP-LC3 mice on the inner segment of the photoreceptors. (B) Magnification of a region that shows, in the left, bigger structures proper of the IS and in the right, several cilia and the apical part of

For the experiment, retinas of GFP-LC3 mice at postnatal day 20 were dissected and cultured *in vitro* with EBSS and rapamycin to induce autophagy, as well as with protease inhibitors (PI) to follow the autophagic flux, for 24h. Figure 4.44 shows representative images of the experiment. In the control image, it can be observed an intense green background signal that hampers the identification of the APs. In culture with PI, APs appear more resolved and a bit more intense than in control, but the number of APs does not seem to be increased. In retinas cultured with EBSS and rapamycin, the background fluorescence is reduced and more intense dots with bigger size appear. Addition of PI shows the accumulation of these large dots and how they occupy almost all the narrow cytoplasm. This is suggesting that mouse retina at postnatal day

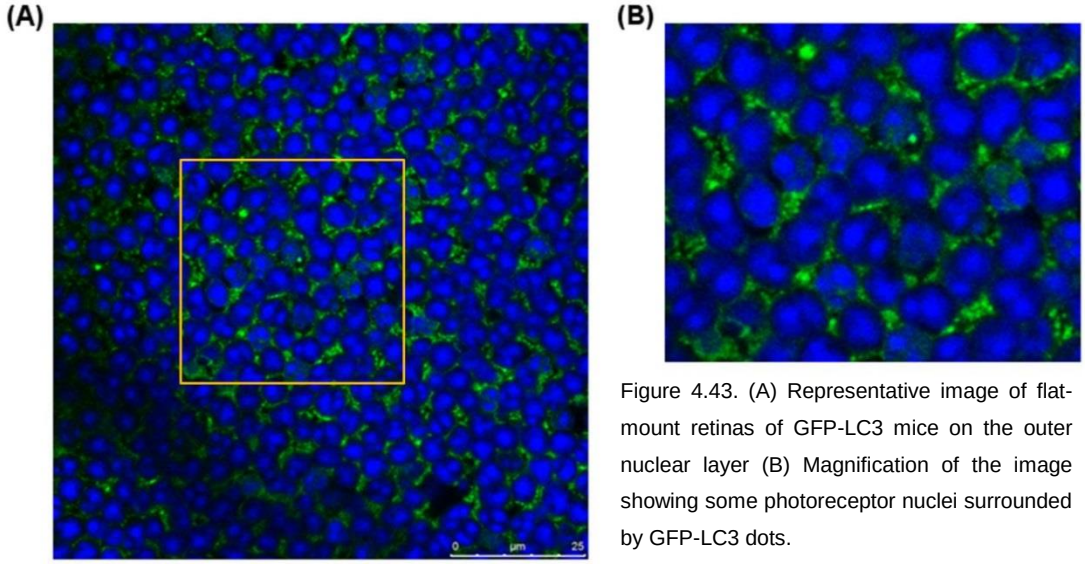

Figure 4.43. (A) Representative image of flat-mount retinas of GFP-LC3 mice on the outer nuclear layer (B) Magnification of the image showing some photoreceptor nuclei surrounded by GFP-LC3 dots.

20 do not present a high autophagic flux but, in the presence of an autophagy inducer, it could respond intensely.

For the analysis with WimAutophagy, we selected the confocal planes from each field that

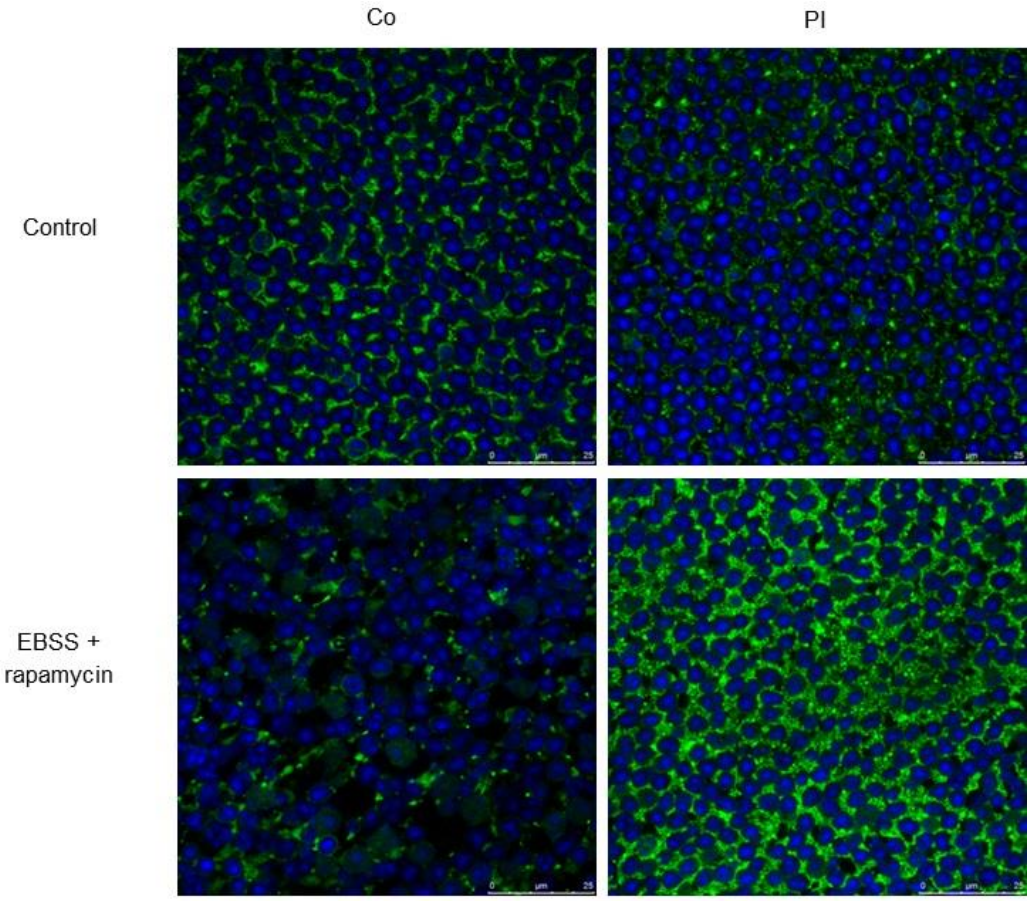

Figure 4.44. Representative image of flat-mount retina of C57 mice after the culture in DMEM or EBSS with rapamycin and both with or without protease inhibitors (PI). Green channel shows GFP-LC3 and blue channel, the nuclear marker DAPI.

included the photoreceptor nuclear layer at the regions where the central part of most of the nuclei were visible, and quantified separately every picture. The selected parameter to study the experiment was total AP area in pixels per cell in each confocal field. It is not as precise as the parameters studied for cells (Puncta per cell, Estimated APs per cell) but it was not possible for the algorithm to define precisely the cytoplasm area of each cell and, thus, to solve this problem, we estimated the mean APs per cell by dividing the total AP area by the number of nuclei per image.

The numeric results obtained are coherent with the images (Figure 4.45). There is no difference in the APs quantification between control and PI, even if it appears that the sharpening of the APs with PI is rendering a smooth trend of increase. EBSS culture with rapamycin shows a great variability in the quantification, which with the addition of PI, clearly shows the induction effect of EBSS and rapamycin with the enhancement of the APs area compared to basal conditions.

Therefore, even if the imaging conditions were not optimal for the algorithm it is still able to render a quantification that represents the observed.

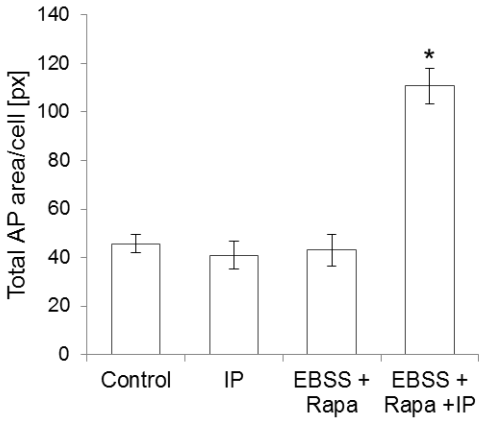

Figure 4.45. Graphic representation of the quantification with the WimAutophagy module for GFP-LC3 flat-mounted mice retinas cultured with EBSS+rapamycin and in presence /absence of PI.(*: p<0.000).

4.1.2. Apoptosis imaging analysis: WimApoptosis module

This module has been developed to quantify apoptotic cell death in cell or tissue samples, on images acquired by epifluorescence or confocal microscope. It has been adjusted to work with the most common methods to detect apoptosis which are:

- *Nuclear condensation:* as the last step previous to cell death, chromatin is condensed and attached to the nuclear membrane, and the DNA, fragmented. Thus, these steps can be observed as small or fragmented nuclei and easily detected with DNA labelling (DAPI, Hoechst…).
- *TUNEL labelling:* TUNEL assay (Tdt-mediated dUTP Nick- End Labeling) uses terminal deoxynucleotidyl transferase (Tdt) to add labelled nucleotides to the DNA fragmented strains.

- *Caspases immunostaining:* caspases are essential enzymes in the apoptotic process. Their activation can be detected by labelling with an antibody that recognizes the active/cleaved form of caspases.

4.1.2.1. WimApoptosis algorithm description

This algorithm follows the similar steps to the WimAutophagy; processing and data merge.

a) Processing

1. **Filtering of input Images (Standardization):** it consists on the elimination of noise in the input images. It follows the same steps as the WimAutophagy module. Once the image is split into its colour channels (RGB), the software standardizes the image size, increases the contrast and corrects irregular illumination.

Then, the algorithm recognizes the apoptotic cells. Depending on the labelling of the samples, some steps may not be applied:

2. **Nuclei identification:** nuclei are detected, surrounded by a white circle and numbered. Nuclei that are not completely inside the image will not be analysed.
3. **DAPI apoptotic cells recognition**: the mean area and brightness intensity of the nuclei are calculated. Those nuclei with reduced size area and brighter intensity will be considered DAPI apoptotic cells and will be labelled with a red perimeter (Figure 4.46, bottom panel).

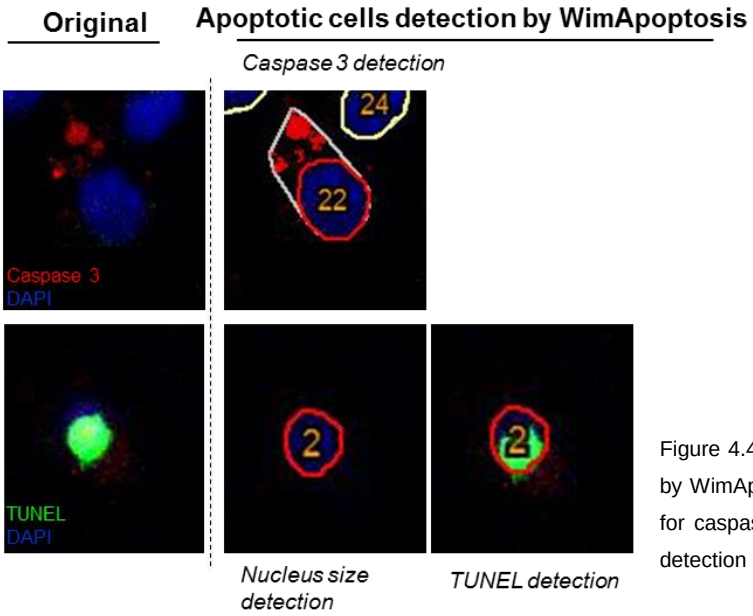

Figure 4.46 . Examples of processed images by WimApoptosis module. Top: output image for caspase 3 active; botton: apoptotic DAPI detection and TUNEL output image.

4. **TUNEL apoptotic cells recognition:** the algorithm contrasts the information from the DAPI and TUNEL channels. There will be considered apoptotic cells those presenting both labelling, avoiding unspecific labelling with TUNEL (Figure 4.46, bottom panel). They are identified by delimiting their nuclei with a red line.

5. **Caspase apoptotic cells recognition**: the algorithm stablishes an area of interest around the nuclei (cytoplasmic region) for subsequent search of caspase staining, and assignment to the corresponding nucleus. Caspase positive cells will be those which present a concrete number of caspase pixels in their cytoplasm and they are identified with a red perimeter around the nucleus (Figure 4.46, top panel).

After the pre-processing and recognition steps, the module generates a processed image for each parameter (DAPI, TUNEL and/or caspase). The output images present the nuclei of healthy cells with a yellow perimeter and of apoptotic cells, with a red one.

b) Data merge

The module also merges all the generated data into CSV files. There will be provided one file per individual image and a summary file of the whole experiment.

In the individual CSV file (Figure 4.47), the information is organized in two parts. The first two lines indicate the overall data of the analysis for that image and will be detailed bellow. The rest of the rows display the individual cell metrics:

	A	B	C	D	E	F	G	H	I
1	Number of Cells	Estimated Area Healthy Cells [px]	Number Apoptotic Cells DAPI	Estimated Area APOP Cells DAPI [px]	Mean Area APOP Cells DAPI [px]	Mean Intensity APOP Cells DAPI	Number Apoptotic Cells Tunel	Estimated Area APOP Cells Tunel [px]	Mean Area APOP Cells Tunel [px]
2	41	1571	7	602	709	0.41	9	524	658
3									
4	ID	Area Nuclei [px]	Mean Intendity	Positive DAPI Cells	Positive tunel Cells	Positive caspasa Cells	Positive caspasa & tunel Cells		
5	1	1071	0.26	No	No	No	No		
6	2	1791	0.38	No	No	Yes	No		

	J	K	L	M	N	O	P	Q	R
	Mean Intensity APOP Cells Tunel	Number Apoptotic Cells Caspasa	Estimated Area APOP Cells Caspasa [px]	Mean Area APOP Cells Caspasa [px]	Mean Intensity APOP Cells Caspasa	Number Apoptotic Cells Caspasa & Tunel	Mean Area APOP Cells Caspasa & Tunel [px]	Mean Intensity APOP Cells Caspasa & Tunel	
3	0.43	31	1446	1293	0.36	9	658	0.43	

Figure 4.47. Example of a CSV file for a single image. The bottom image is a continuation on the right of the top image. The first two lines show the summary metrics of the image. From the fourth line on it shows the individual metris for each cell.

1. ID: number for identification of cell in the control image (column A).
2. Nucleus Area [px]: nucleus area in pixels (column B).
3. Mean Intensity: mean intensity of the nuclei (column C).
4. Positive DAPI Cells: Yes/No to indicate if the cell is positive for apoptosis by DAPI staining (column D).

5. Positive TUNEL Cells: Yes/No to indicate if the cell is positive for TUNEL labelling (column E).
6. Positive caspase Cells: Yes/No to indicate if the cell is positive for active caspase staining (column F).
7. Positive caspase & TUNEL cells: Yes/No to indicate if the cell is positive for both caspase and TUNEL (column G).

The first lines of the individual image CSV file show the following information, which is the summary of the individual parameters:

1. **No. Cells:** total numbers of cells in the image (column B).
2. **Estimated Area Healthy Cells [px]:** estimated area of the healthy cells in pixels (column C).
3. **Number DAPI Apoptotic Cells:** number of the apoptotic cells detected with DAPI (column D).
4. **Estimated Area DAPI Apoptotic Cells [px]:** estimated area of the DAPI apoptotic cells in pixels (column E).
5. **Mean Area DAPI APOP Cells:** mean area of the DAPI apoptotic cells in pixels (column F).

$$Mean\ Area = \frac{1}{N}\sum Area_i$$

6. **Mean Intensity DAPI Apoptotic Cells:** mean intensity of the DAPI apoptotic cells (column G).

$$Mean\ Intensity = \frac{1}{N}\sum Intensity_i$$

7. **Number TUNEL Apoptotic Cells:** number of the TUNEL apoptotic cells detected (column H).
8. **Estimated Area TUNEL Apoptotic Cells [px]:** estimated area of the TUNEL apoptotic cells in pixels (column I).
9. **Mean Area TUNEL APOP Cells:** mean area of the TUNEL apoptotic cells in pixels (column J).

$$Mean\ Area = \frac{1}{N}\sum Area_i$$

10. **Mean Intensity TUNEL Apoptotic Cells:** mean intensity of the TUNEL positive cells (column K).

$$Mean\ Intensity = \frac{1}{N}\sum Intensity_i$$

11. **Number Caspase Apoptotic Cells:** number of the caspase apoptotic cell detected

(column L).

12. **Estimated Area Caspase Apoptotic Cells [px]:** estimated area of the caspase apoptotic cells in pixels (column M).
13. **Mean Area caspase APOP Cells:** mean area of the caspase apoptotic cells in pixels.

$$Mean\ Area = \frac{1}{N}\sum Area_i$$

14. **Mean Intensity caspase Apoptotic Cells:** mean intensity of the caspase apoptotic cells (column N).

$$Mean\ Intensity = \frac{1}{N}\sum Intensity_i$$

15. **Number TUNEL & Caspase Apoptotic Cells [px]:** number of the double positive cells for TUNEL and caspase detection (column O).
16. **Mean Area TUNEL & caspase APOP Cells:** mean area in pixels of the double positive cells for TUNEL and caspase detection (column P).

$$Mean\ Area = \frac{1}{N}\sum Area_i$$

17. **Mean Intensity TUNEL & Caspase Apoptotic Cells:** mean intensity double positive cells for TUNEL and caspase detection (column Q).

$$Mean\ Intensity = \frac{1}{N}\sum Intensity_i$$

The summary CSV file shows the following information, which is a compendium of all the individual files (Figure 4.48):

1. **Name of the image:** (column A).
2. **Number DAPI Apoptotic Cells:** number of the DAPI apoptotic cells detected (column B).
3. **Number TUNEL Apoptotic Cells:** number of the TUNEL apoptotic cells detected (column C).

	A	B	C	D	E	F
1	File Name		Number of Cells	Number Apoptotic Cells DAPI	Number Apoptotic Cells Tunel	Number Apoptotic Cells Caspasa
2	E026_wimasis/E026_wt_0		171	23	2	6
3	E026_wimasis/E026_wt_0		95	9	4	7
4	E026_wimasis/E026_wt_0		53	5	0	6
5	E026_wimasis/E026_wt_0		118	11	1	1
6	E026_wimasis/E026_wt_0		151	5	6	23
7	E026_wimasis/E026_wt_0		88	0	2	13

Figure 4.48. Example of a CSV file of a summary sheet. It shows the main parameters on each image.

4. **Number Caspase Apoptotic Cells:** number of the caspase apoptotic cell detected (column D).
5. **Number TUNEL & Caspase Apoptotic Cells [px]:** number of the TUNEL and caspase apoptotic cells detected (column O).

4.1.2.2. Validation of the WimApoptosis image analysis

In order to validate the developed algorithm, we performed two experiments with TUNEL and activated caspase 3 labelling, in cultured cells and tissue.

- **Case of study 1: quantifying cell death with active caspase 3, DAPI and TUNEL labelling in cells**

Mouse embryonic fibroblasts (MEFs) control and Bax/Bak double knockout (DKO) were used to validate apoptosis quantification performed by WimApoptosis. Bax/Bak DKO MEFs were used as negative control, as they cannot accomplish apoptosis because Bax and Bak proteins are necessary for the pathway. Cells were cultured with the apoptosis inducer staurosporin (STS) at 500 nM for 16h. Subsequently, apoptotic cell death detection was performed by TUNEL labelling and active caspase 3 immunostaining. Images were acquired with confocal microscopy and analysed with WimApoptosis.

Representative images of the experiment are shown in Figure 4.49-A. Control MEFs after

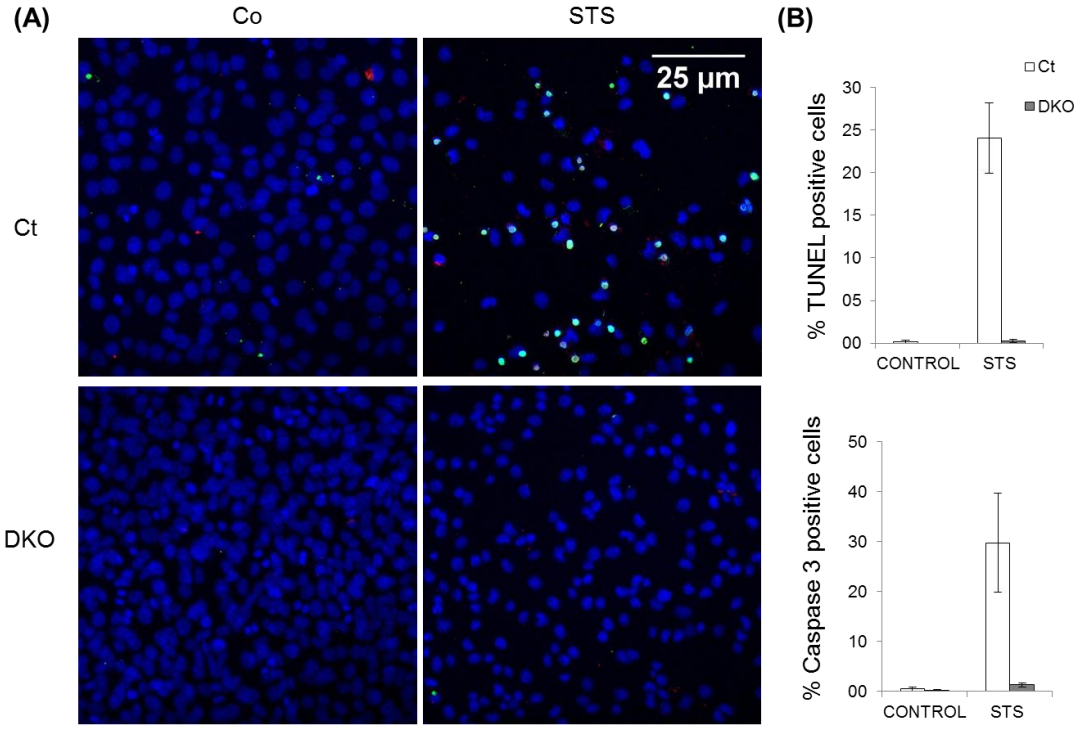

Figure 4.49 (A) representative images of wild-type and DKO Bax/Bak MEFs stained for DAPI, active caspase 3 and TUNEL after a 16h culture with staurosporine 500nM (STS). (B) Quantification of the percentage of positive cells for TUNEL and caspase 3 performed by WimApoptosis.

culture with staurosporine show an increment on both caspase 3 and TUNEL staining, reflected in the quantification obtained from WimApoptosis module in panel B. On the other hand, DKO MEFs scarcely present labelling after the treatment, as expected, and the quantification is almost cero, validating that the detection performed by the algorithm is not generating “false positives”.

For properly validating the algorithm, we estimated the correlation between the quantification by Wimasis and a manual quantification, as in this case is feasible. Figure 4.50 shows the correlation between both counts for TUNEL and caspase 3 with a great fit in both cases, but more precise for TUNEL. The reason why caspase 3 presents a more relaxed fit is because the staining is not as defined as TUNEL, and the applied algorithm is stricter for caspase 3, rejecting some signal that maybe in the manual count would be accepted.

Hence, we have validated the detection and quantification performed by the WimApoptosis module for cell sample imaging for the three different labelling: DAPI, TUNEL and Caspase 3

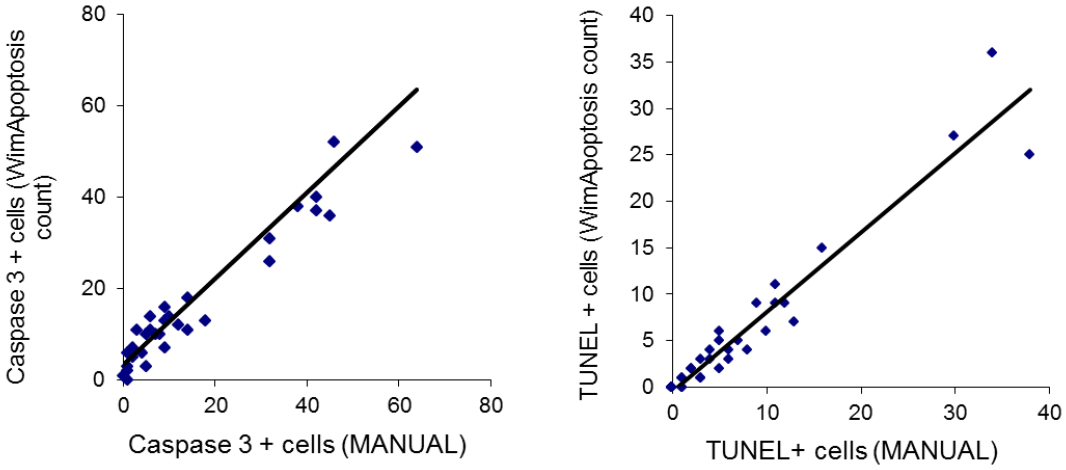

Figure 4.50. Correlations between manual quantification and the performed with the WimApoptosis module. The function obtained for TUNEL is y= 0.851x -0.3735 with a fit of R^2 = 0.9316 and for caspase 3 y=0.9395x + 3.4009 R^2=0.7286 with an fit of R^2=0.7286.

active.

- **Case of study 2: quantifying cell death with TUNEL labelling in flat-mount retinas**

For validation of the algorithm performance with tissue samples, retinas from rd10 mice at postnatal day 20 (P20) were used and cultured with trichostatin A (TSA) 1µM. Rd10 mouse is a model of retinitis pigmentosa and it presents a cell death peak of photoreceptors at postnatal day 20. Retinas were stained with TUNEL and the confocal images (a z stack of the different planes that comprised the ONL) were analysed with the WimApoptosis module Figure 4.51 shows an example image of the detection of TUNEL positive cells by WimApoptosis. We can appreciate that it can recognize whole nuclei as well as some nuclei that are already initiating the DNA fragmentation phase.

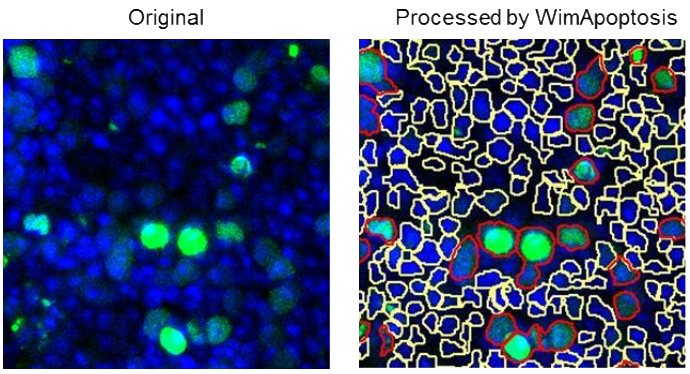

Figure 4.51. Example of image processing by WimApootosis with tissue images. Left image shows an original image of flatmount retina of Rd10 mouse at P20 stained with DAPI and TUNEL. Right image shows the image after WimApoptosis processing. The nuclei of apoptotic cells present red perimeter.

Figure 4.51-A panel shows representative images of the experiment. Rd10 control retinas present high cell death levels, as expected at this age, and, after the treatment with TSA, cell death is slightly reduced, even if it does not reach significance. 0

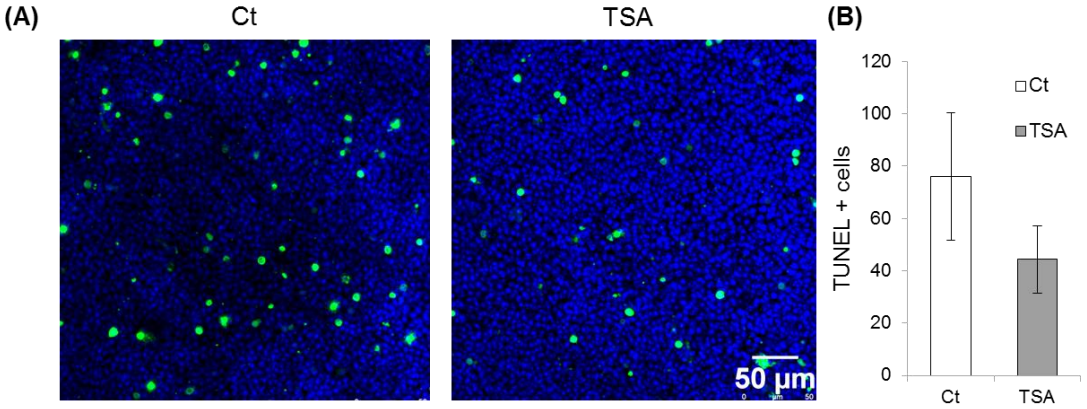

Figure 4.52 (A) Representative images of flatmount retinas at P20 after 24h of culture with TSA 1µM. (B) Quantification of TUNEL positive cells by WimApoptosis.

For further validation of the algorithm, the correlation between the manual quantification and the performed by Wimasis was calculated. Figure 4.52 shows the good fit of the correlation obtained, although it is perceptible that in this case, the algorithm is more precise than the

manual counting, as it is considering more cells as TUNEL positive cells. It is not because it is including “false positives” in the count but because it performs a more accurate detection than manual counting, validating the usage of WimApoptosis for tissues as well as for cultured cells.

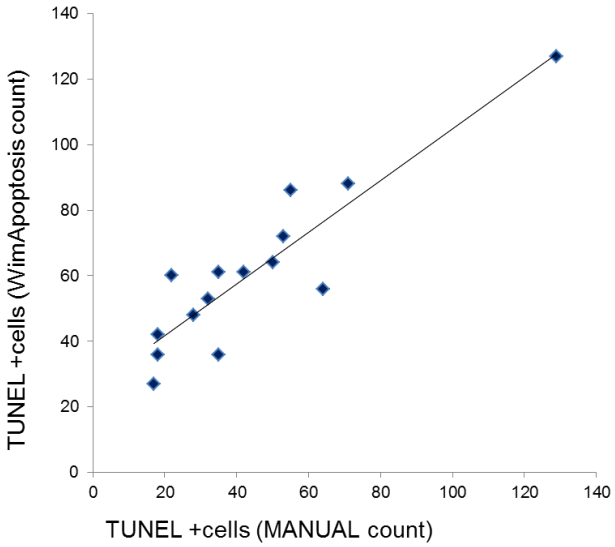

Figure 4.53 Graphic representation of the correlation between manual quantification and the performed with the WimApoptosis module. The obtained function is y = 0.7888x + 25.953 with a fit of $R^2 = 0.822$.

Hence, as a result of the collaboration with the Wimasis company there have been developed two modules for the imaging analysis of autophagy and apoptosis essays in different samples, labelling and microscope, providing a powerful tool for addressing, among others, neurodegenerative or oncologic studies.

5. DISCUSSION

5. DISCUSSION

5.1. Developing new tools for studying neurodegeneration

Autophagy is a field in expansion due to the growing interest on its function for elimination of long-lived, altered or aggregated proteins, which places autophagy an essential pillar for the cell homeostasis. It is a highly conserved process, which makes it relevant not only for studies in mammals but for other eukaryotes too. Autophagy is highly significant in many diseases as cancer or neurodegenerative diseases as well as in stroke, diabetes type 2 and a crescent list of alterations, where, often, cell death is also occurring. A valuable technique to study these contexts is fluorescence imaging and thus, the development of tools that improve the analysis of imaging data for autophagy and apoptosis assays will be decisive to the progress of research in these systems.

5.1.1. WimAutophagy algorithm

From its discovery, the approaches to autophagy have evolved, being the integration of the perception of autophagy as a dynamic process in the research methods a key for its improvement, besides the advance in all the laboratory technologies and the introduction of informatics as a routine tool.

As illustrated in the introduction, main approaches are TEM, western blot and fluorescence imaging. All of them present their strengths but, undoubtedly fluorescence imaging is the technique that can provide larger information and more precise. Therefore, the enrichment of the computer tools for the processing of imaging data will enhance the perspective of the autophagic process. There are several programs for imaging analysis suitable for the study of autophagy. For instance, there has been developed a macro for the free program Image J for puncta quantification in GFP-LC3 transfected cells (Chu et al., 2009; Dagda et al., 2008). Other examples, from private platforms, are the Imaging package in Pipeline Pilot (Accelrys) or Top Hat algorithm of MetaMorph (Molecular Devices). These platforms allow the user to work with a great input of images and to perform an analysis of the puncta per cell or the percentage occupied by the autophagosomes. The great advantage of Wimasis algorithms is that the module is already trained for autophagy detection and, besides, it automatically runs on a cloud, so the user only has to upload the images on the website and in a few hours, retrieve the results, avoiding the process of learning how to use the software, the setting up period and the time itself to analyse the images.

5.1.1.1. WimAutophagy working options

WimAutophagy is a very versatile module able to analyse images with different labelling, microscopy conditions and cell types. The standard marker to monitor autophagy is LC3. There are several ways to detect it by fluorescence. The most commonly used are overexpression of GFP-LC3 or immunolabeling. GFP-LC3 is a great tool to monitor the autophagic process, which even allows observing the two forms of LC3: I and II. In some cases, the diffuse cytoplasmic signal of LC3-I might be too intense, especially on the analysis of epifluorescence images, that it can dilute the dotted signal of LC3-II. However, the algorithm is able to avoid this distortion by applying a strict filtering of the image and by restricting the selection of APs in the pre-processing (according to signal intensity, area and relative position to a nucleus), resulting as a whole in a smaller scale for the quantification of epifluorescence images versus confocal images, as in case of study 1, but providing analogous results and, hence, leading to the same interpretation of the assay. In the GFP-LC3 tissue analysis, the case of study 3, the background was too intense that masked a great percentage of the APs signal. The obtained results showed no difference between the culture in control conditions or IP, suggesting that there could be a slowed down autophagic flux in basal state. But from previous results from the lab, we know that retinas at 20 days of age present an active autophagic flux and thus, we can deduce that the background signal is masking the signal of APs, that otherwise could be detected. However, when a great increase in APs happens, as in the culture in EBSS with rapamycin, the algorithm is able to detect them, probably because, in parallel with the increase of dots, also the background signal is a reduced. This reduction of the background signal would be due to a decrease of the cytosolic pool of LC3-I, as LC3-II could be generated at faster speed than in basal conditions and could also get to be faster than the production of LC3-I.

This example remarks the fact that the limitations of our techniques and tools define our results, and this is the reason why it is necessary to keep improving them. In this case, even if we validated the that the algorithm is able to perform a precise quantification of autophagy in cell imaging for GFP-LC3, as exemplified in the case of study 1, the conditions of the GFP-LC3 in tissue exceeded the limits of detection of the microscope and of the algorithm. Probably, a better quantification could be achieved by working with mice with lower levels of expression of GFP-LC3, which would reduce the intensity of the cytosolic LC3-I. Also, delimitating the cytoplasm of the cells with Tuj 1 (neuron-specific class III beta-tubulin) would help the algorithm to define the working area for the assignation of APs to cells.

The other LC3 detection way validated in this study, immunofluorescence labelling, provides better work conditions for the algorithm. The validation section and the experiment with 661w cells for studying the compensation mechanism between macroautophagy and CMA (section 4.2.1.5)), show clearly that the algorithm is able to perform an accurate detection of autophagosomes and cell assignment, as the quantification of p*uncta per cell, total estimated APs* and *total AP area* for Atg7 KD cells showed only a residual presence of LC3 in these cells. Moreover, the Atg7 KD construct that included a GFP transfection reporter, recognizable by the

algorithm, gave us the possibility to perform the analysis exclusively on transfected cells. A selective analysis is meaningful for any study with transfected cells, but it could be especially relevant in studies with low transfection percentages, to make them more precise, avoiding the inclusion of non-transfected cells in the quantifications. In our case, on top of this, it provided us the chance to compare transfected cells with non-transfected cells to check that culture conditions were optimal and to validate the process, as well.

Moreover, the case of study 2 helped us to validate the flexibility of the algorithm by detecting CMA + lysosomes on 661w control and LAMP-2A KD. The fact that WimAutophagy module can work with other labels than LC3, as LAMP-2A, broadens its application further than the macroautophagy field to CMA or even to the study of other vesicular systems in the cell (lysosomes, peroxisomes, endosomes, Golgi transport…). Also, to better adjust the algorithm to the CMA field, it would be necessary to include Hsc70 detection and quantification to study the colocalization of LAMP-2A and Hsc70, as this is the way to detect them when it is not possible to transfect the cells with the construct KFERQ-PA-mCherry1.

Hence, the module WimAutophagy is an accurate, robust and flexible tool to perform imaging analysis on very different models, including cell or tissue samples, and with different LC3 labelling (GFP-LC3 and immunostaining) with the great advantage that it runs on a cloud. Also, its flexibility would open the chance to apply to the study of other cellular processes as CMA.

5.1.1.2. Remarkable parameters provided by WimAutophagy module

In this study we have validated new software specifically adjusted for autophagy quantification with a potent and accurate algorithm. It quantifies autophagy by three parameters*: puncta per cell, total number of estimated APs* and *total AP area,* and in addition it provides the *AP size. Puncta per cell, total AP area* and *puncta size* are achievable by other software, but only the WimAutophagy module estimates the mean AP size to provide the *total estimated APs per cell*. This important intermediate parameter is derived from the pre-processing step of analysis of the puncta populations, that results in the setting of a medium AP size, necessary for the estimation of the number of individual APs that would be contained in a cluster.

Furthermore, autophagy modulation is traditionally studied by the changes in the number of APs, but it is known that also AP size is modulated, even if little has been described yet (Jin and Klionsky, 2014). Hence, AP size is not only an intermediate calculation to estimate APs per cell, but a parameter per se with rising interest. We could observe in the case of study 1 how HCQ, aside to impede the fusion between lysosomes and autophagosomes, was inducing the formation of bigger APs, probably as a consequence. As this modulator, probably all the autophagy modifiers are exerting, to a greater or lesser extent, an effect on the size of the APs that should be taken into account to understand their effect and apply this knowledge to the development of new treatments for pathologies related to autophagy.

Therefore, in order to integrate the variation of APs number and APs medium size in one parameter, we have generated the *total number of estimated APs,* which summarizes in one

number the “quantity of autophagy that is being performed by a cell”. Also *total AP area* could reflect similar information, as the bigger the size and number of APs, the larger the area occupied by APs, concretizing the idea of “how much volume of the cells is undergoing autophagic degradation”. But the advantage of *total estimated APs* compared to *total AP area* is that the autophagic activity is related to its basic unit: the autophagosome, and, in particular, to the mean autophagosome size of a particular system. Especially when pre-fixing a medium APs size for the whole experiment, t*otal number of estimated APs* provides an index to easily compare how treatments are modulating autophagy. This index avoids the loss of information observed on *puncta per cell,* where there is an underestimation of the “volume of the cell that is performing autophagy”, or on *total number of estimated APs* when the medium AP size is not pre-fixed where, as in our case, the treatment that presented more autophagosomes also induced a bigger size of them. Therefore, *total number of estimated APs* is particularly relevant when studying the autophagic flux, which compares the number of autophagosomes in basal conditions and under blockage, with HCQ, among others.

Therefore, WimAutophagy is a specialized tool for systematic quantification of autophagic assays with different cell types, autophagosome labelling and microscopy acquisition due to its precise preparation of the image and to the accurate quantification performed by the algorithm. It provides parameters traditionally used in the field, as *puncta per cell* and *total AP area*, but it also includes the measurement of *total number of estimated APs* per cell, that we purpose as an index that simplifies the measurement of autophagic activity relativized to its basic unit: the autophagosome. We also purpose to perform the analysis of the images always without and with fixing the medium AP size, for a deeper overview of how autophagy is being modulated.

5.1.2. WimApoptosis algorithm

Apoptosis is a cell death pathway essential for tissue and organism homeostasis and it is involved in many processes as neurodegeneration and cancer. WimApoptosis allows the recognition and quantification of apoptotic cells on microscopy images determined by three of the main methods: nuclear size, activated caspase 3 detection and TUNEL labelling. Moreover, it provides the quantification of double-stained cells with caspase 3 and TUNEL. This parameter is quite relevant because caspase 3 and TUNEL, even if both label apoptotic cells, they detect different steps of the apoptotic pathway: caspase 3 is activated in earlier steps and, after a chain of reactions, DNA is fragmented, which is labelled by TUNEL. If the user is interested on the temporal or spatial localization of an apoptotic wave, the quantification of both labelling separately and combined could be helpful. It could be interesting to remark that we used the activation of caspase 3 as it is one of the main markers for apoptosis, but other caspases could be analysed too, as they would present a similar signal distribution in the cell.

Another interesting parameter generated by the algorithm is the area of the detected cells. As shown in the results section, it provides the estimated area of each apoptotic cell for the different labelling and also the area of the nucleus of each cell, including healthy cells.

The high correlation obtained between the quantification performed by WimApoptosis and the manual quantification of caspase 3 and TUNEL positive cells, both in cell and tissue samples, and the non-detection of apoptotic cells in Bax/Bak DKO MEFs validates the algorithm showing its robustness and accuracy. It is remarkable the good performance on tissue as few imaging analysis tools are suitable for its study, and not in the fast way of the Wimasis system.

Thus, WimApoptosis is a robust tool for measuring apoptosis in cell and tissue samples labelled with the main markers. Moreover, it also provides the quantification of doubly marked cells, useful to monitor the kinetics of the apoptotic cell death process.

Therefore, we purpose two new tools for the analysis of autophagy and apoptosis that, used in combination, can be useful to monitor the aetiology of those patholgoies where autophagy and apoptosis are bonded, as neurodegeneration or cancer.

5.2. Autophagy and neurodegeneration in the retina

There are growing evidences that autophagy is essential for neuronal homeostasis and it is found in many neurodegenerative diseases an alteration of the process. Many neurodegenerative diseases are caused by the accumulation of aberrant proteins in the cytoplasm of neurons or the extracellular matrix and usually in these cases there is an impairment of the autophagic process. In addition, neurodegenerative diseases are related to aging, which among other alterations includes autophagy decline. Thus, neurodegeneration and autophagy impairment are in close relation. Furthermore, the main evidence of this relation is the mouse models Atg5$^{flox/flox}$; nestin-*Cre* mice (Hara et al., 2006) and Atg7$^{flox/flox}$; nestin-*Cre* mice (Komatsu et al., 2006). These mice models show that the lack of autophagy in central nervous system is enough to generate the accumulation of inclusion bodies and other neurodegeneration signs in the brain that finally lead to a behavioural impairment. Thus, the models demonstrate the fundamental role of basal autophagy for the brain physiology.

However, nothing is described in these models about the particular case of the retina, and little is known in the literature about the role of autophagy on the physiology of the retina, a highly specialized region of the brain. Thus, the objective of our study was to answer the question of how the lack of autophagy in the neural precursors could affect the physiology of the retina and if it was comparable to the decline derived from aging, described by our laboratory (Rodríguez-Muela, 2011). We were also interested in the study of cerebellum after the obtained results in the retina to contrast if these results were translatable to other parts of the CNS. We chose cerebellum because, as retina, it presents a greatly organized structure and it was suggested in the original description of the mouse model from Hara et al. (2006) to present cell death in a “cell-autonomous fashion”.

5.2.1. Dysfunctionality and structural alterations of the retina in the absence of autophagy

We have characterised the retinal phenotype of a murine model with autophagy absence in the neural precursors, the *Atg5*$^{flox/flox}$; nestin-*Cre* mouse, from functional and structural points of view and this section will discuss both data sets as a whole.

In the *Atg5*$^{flox/flox}$; nestin-*Cre* model, neural precursors start expressing nestin at E7.75 in some brain regions (Dahlstrand et al., 1995) and the total elimination of Atg5 and LC3-II is effective at E15.5 in the whole brain (Hara et al., 2006). In the nervous system, nestin positive neural precursors originate neurons as well as macroglia, that includes astrocytes and oligodendrocytes and the retinal pigment epithelium, with a main role in the visual cycle (Lendahl et al., 1990; Fisher, 1997; (Puelles López et al., 2008; Tang et al., 2013).

We first assessed a functional study by a full field electroretinogram under scotopic and photopic conditions, to analyse the response of rod and cone pathways. Our results show that the *Atg5*$^{flox/flox}$; nestin-*Cre* mice have a depressed scotopic response compared to control animals, indicating alteration in the rod function (see below). Conversely the waves registered under photopic conditions (flicker and b-photopic wave) present similar levels in *Atg5*$^{flox/flox}$; nestin-*Cre* and control animals, showing that cone function is maintained and, thus, that the diurnal vision is preserved.

We have registered several waves to define rod function. b-scotopic wave, which reflects the electrical work of rod bipolar cells, had a diminished amplitude in *Atg5*$^{flox/flox}$; nestin-*Cre* mice. This indicates that there could be an alteration on the bipolars themselves, or a lower reception of stimuli from rods, or both. The later situation is named as deafferentation and it means that bipolar cells loose the signalling input, as the photoreceptors degenerate, which leads to bipolar cells degeneration (D'Orazi et al., 2014). It has been shown that there is a positive correlation between the amplitude of the b-scotopic wave and the ONL thickness (if INL thickness remains invariable), for instance, in some retinitis pigmentosa models (McGill et al., 2012; Pinilla et al., 2005) or the rotenone model of Parkinson's disease (Esteve-Rudd et al., 2011). We tested this correlation and, indeed, there was a reduction of the ONL thickness in *Atg5*$^{flox/flox}$; nestin-*Cre* animals compared to control, indicating that there is a loss of photoreceptors in these retinas. We also studied the morphology of rod bipolar cells by immunostaining retinal cryosections with PKCα antibody and we found that some of the rod bipolar cells of *Atg5*$^{flox/flox}$; nestin-*Cre* mice were undergoing a remodelling process, a common feature of retinal degeneration as consequence of the deafferentation, where in the first place, neurons retract their dendrites and then, they sprout new dendrites to synapse with functional photoreceptors (Cuenca et al., 2015). We observed retraction of dendrites in some cells (Figure 4.5) as seen in models of retinitis pigmentosa (Cuenca et al., 2004; Strettoi et al., 2002) or retinal detachment (Fisher et al., 1995; Sakai et al., 2014). However, we did not observe sprouting of new processes, which is neither found in other retinal degenerative processes (Barhoum et al., 2008; Cuenca et al., 2004; Strettoi et al., 2002). To complete our characterization and confirm the absence of

sprouting, it would be desirable to test in addition the levels of glutamate receptor (mGluR6) by immunostaining retinal cryosections, as it is expressed in dendrites of bipolars and it has been shown to diminish its presence in rod bipolar cells of rd/rd mice during the degeneration process (Strettoi et al., 2003; Varela et al., 2003). We also noticed that in *Atg5*$^{flox/flox}$; nestin-*Cre* mice some varicosities of the rod bipolar cells were disorganized and presented an abnormal shape, as if they were empty, which has been described in other photoreceptor degenerative models (Cuenca et al., 2015; Marchena et al., 2011). In the case of rd/rd retinas, a model for retinitis pigmentosa, the axonal endings of the rod bipolar cells are smaller and more rounded than in control retinas since their development was arrested (Barhoum et al., 2008; Strettoi et al., 2002), but in the case of *Atg5*$^{flox/flox}$; nestin-*Cre*, most bipolar cells present normal axonal endings and only some present anomalies. Because the observed degeneration in rod bipolar cells is mild, and because mouse retina reaches maturity around postnatal day 35, it could suggest that the alterations observed in these cells should be posterior to development, as it will be discussed below.

Thus, the data suggests that the retina of *Atg5*$^{flox/flox}$; nestin-*Cre* mice is undergoing a photoreceptor degeneration that is followed by rod bipolar cells degeneration too. The values of a-mixed and b-mixed waves also pointed in the same direction. The relation between both waves also reveals noteworthy information about the morphology of the retina. When the ratio b-wave/a- wave is increased, it indicates higher levels of injury on rods than on cones, as seen, for instance, in retinitis pigmentosa (Pinilla et al., 2005). *Atg5*$^{flox/flox}$; nestin-*Cre* mice at seven weeks of age also presented an increase of the ratio of the b-mixed/a- mixed waves, as the a-mixed wave is diminished compared to control mice. This indicates a poor performance of photoreceptors (a- mixed wave), while the activity of bipolar cells (b- mixed wave) remains not significantly different from control. Since we saw that *Atg5*$^{flox/flox}$; nestin-*Cre* retinas have a lower activity of rod bipolars (b-scotopic wave), and the b-mixed wave is a sum of the electrical work of the bipolars, the b-mixed wave should also be affected in *Atg5*$^{flox/flox}$; nestin-*Cre* retinas. Probably this difference could be achieved by increasing the sampling. In any case, the ratio of the b-mixed/a- mixed waves should remain increased in *Atg5*$^{flox/flox}$; nestin-*Cre* retinas compared to control.

For further supporting rod degeneration, we performed a TUNEL labelling combined with cone opsins staining (blue, red and green) and we observed that they were never colocalizing, indicating that cones were not undergoing cell death and, thus, it should be rods. For a direct measurement of the degenerating rods, it would be preferably to perform a rod specific staining, but the assessed antibodies for rhodopsin stained almost exclusively the outer segment, making it impossible to assign apoptotic nuclei with rhodopsin label. The TUNEL labelling also enlightened the fact that cell death was only occurring in the ONL and not in other layers, even if some functional and morphological alterations were already detectable. Also, TUNEL staining was rarely found in the outer nuclei rows, where cones are placed, providing another support that cell death was affecting mainly rods and not cones.

Agreeing with the commented results, the STR was diminished in *Atg5*$^{flox/flox}$; nestin-*Cre* mice compared to control. The STR shows the performance of ganglion cells after exposition to very faint flashes that only stimulate rods, what in the end places STR as an indirect measurement of rods activity, when no alterations are observed in RGCs. The diminished STR reinforces even more the idea that rods are undergoing degeneration in *Atg5*$^{flox/flox}$; nestin-*Cre* retinas. We discard the possibility of damage in RGCs because, unlike other postsynaptic neurons, they remain stable in degenerative situations such as retinitis pigmentosa (Mazzoni et al., 2008).

Finally, the OP, which reflects the performance mainly of amacrine cells, with a residual contribution of ganglion cells, was also reduced in *Atg5*$^{flox/flox}$; nestin-*Cre* mice compared to control group. For confirming any morphological alteration, we performed a calbindin immunostaining, but we did not find any anomaly in amacrine cells. However, calbindin also labels horizontal cells and, even if the number of cells was stable in *Atg5*$^{flox/flox}$; nestin-*Cre* retinas (data not shown) and their synapses did not present alterations, their cell bodies were bit more closer to the OPL, with an appearance similar to that observed in 20 month-old retinas, before dendrite sprouting towards ONL (Terzibasi et al., 2009), suggesting that horizontal cells could be also undergoing a degenerative process.

As both the OP and STR have a component of RGCs activity and both are decreased, the data could also be interpreted as a decline of these cells, beside the other neurons in the retina. It would be then a mild degeneration that would be aggravated with age. Thus, to check it, it would be necessary to analyse retinas at more aged stages.

Altogether these data indicates that the absence of autophagy in cells derived from neural precursors in mice leads to the degeneration of the rod signalling pathway, affecting the functionality and morphology of rods, rod bipolar cells and also horizontal cells, while the cone pathway remains stable, which is a similar scenario to aged retinas (Kolesnikov et al., 2010a).It is noteworthy to suggest that the alterations of the rod pathway seem to be posterior to the finalisation of the retinal development, which could indicate that the lack of autophagy in neural precursor derived cells would not affect to the appropriate completion of the retina formation, not as suggested *in vitro* for chicken retinal development (Mellén et al., 2008). This could be explained as the embryos of *Atg5*$^{flox/flox}$; nestin-*Cre* mice inherit Atg5 from the oocyte, as the mother is Atg5 competent, allowing the normal development (Mizushima and Levine, 2010). Thus, the observed impairment of the retina could be related to an absence of energy supply because of the lack of autophagy in the post-birth retina, as it has been seen that rats treated with hypoglucemic chronic diet decrease their b-wave and induces retinal degeneration (Umino et al., 2006).

In addition, it could be interesting to observe how *Atg5*$^{flox/flox}$; nestin-*Cre* retinas react to light damage, as Atg7 knockout in rods, total body *beclin1* $^{+/-}$ and *Park2*$^{-/-}$ knockout mice have higher susceptibility to the challenge than control animals (Chen et al., 2013). However, Zhou et al. (2015) found that an Atg5 knockout mice for rods presented the same reaction than control animals even if they were subjected to higher levels of light intensity and longer exposure time.

Nevertheless, in our *Atg5*$^{flox/flox}$; nestin-*Cre* animals, as also RPE and macroglia are affected by the lack of autophagy, it seems probable that they would present higher sensitivity to light damage, as in the total body *beclin1* $^{+/-}$ and *Park2*$^{-/-}$ knockout mice.

5.2.2. Macroglia activation in the absence of autophagy in the retina

In the retina, glial cells include microglia, with an immune origin, and macroglia, with a neural origin, composed by astrocytes and Müller cells. Both, micro and macroglia are in tight relation with neurons to support them metabolically and to protect them, acting in a coordinated way. In fact, one of the first signs of retinal alteration is reactive gliosis (macroglia activation) (Cuenca et al., 2015). As *Atg5* $^{flox/flox}$; nestin-*Cre* macroglia was lacking autophagy, we were interested on how it could be affected in the retina.

Macroglia activation is characterized by hypertrophy, ramification of the cellular processes and up-regulation of GFAP (Pekny et al., 2014). By GFAP immunostaining we could analyse the activation state of astrocytes in *Atg5*$^{flox/flox}$; nestin-*Cre* retinas. We observed that *Atg5*$^{flox/flox}$; nestin-*Cre* astrocytes were active, compared to control. We considered that the reactive gliosis of astrocytes would be a reaction in response to the degeneration suffered by the retina after autophagy deficiency, as seen in diabetic retinopathy (Barber et al., 2000) or AD (Edwards et al., 2014), but that could also be reinforced by the lack of autophagy itself in macroglial cells and, thus, they could be activated as a manifestation of their own damage. Nevertheless, it has been suggested that autophagy impairment in macroglia does not elicit reactive gliosis. *Sumf1*$^{flox/flox}$;GFAP-Cre mice, where the specific knockout of sulfatase modifying factor 1 (SUMF1, a protein necessary for some lysosomal enzymes) in astrocytes induces the blockage of autophagy and they do not present reactive gliosis (Di Malta et al., 2012). However, a *Sumf1*$^{-/-}$ mouse model, with a total knockout body for the protein, does present gliosis, indicating that, even if autophagy was impaired in astrocytes, they were able to get active to support the degenerating neurons and the retina, which is more similar the case of *Atg5* $^{flox/flox}$; nestin-*Cre* retinas (Di Malta et al., 2012).

Furthermore, the aged retinas that present a blockage of the autophagic flux paralleled with an accumulation of ubiquitin (Rodríguez-Muela, 2011), presented astrocytes reactivity, as has also been shown in rat (Mansour et al., 2008) and human retinas (Wu et al., 2003). Thus, astrocytes from *Atg5* $^{flox/flox}$; nestin-*Cre* and aged retinas are activated compared to control probably in order to restore the tissue damage derived from the lack of autophagy, even if the astrocytes themselves are also depleted of autophagy to a greater (*Atg5* $^{flox/flox}$; nestin-*Cre*) or a lesser extent (aging).

However, it is dangerous to extrapolate astrocyte behaviour observed in the brain to the retina, because most of the attributed functions to astrocytes in the brain are carried out by Müller cells in the retina, even if both Müller cells and astrocytes cooperate to maintain neuronal homeostasis in this tissue (Coorey et al., 2012). Therefore, to better understand the phenotype after autophagy down-regulation, it would be desirable to study the macroglia state of activation

in *Atg5* $^{flox/flox}$; nestin-*Cre* and aged retinas, as they are almost imperceptible in the performed flat-mount approach. For instance, a GFAP immunostaining on retinal cryosections would show mainly the activation of Müller cells, as they are placed longitudinally in the retina, perpendicularly crossing all the layers. The observation of these cells is also relevant a failure of Müller cells to clear extracellular glutamate reduces de b-wave in the ERG (Barnett and Pow, 2000), and it could be also contributing to our results in *Atg5* $^{flox/flox}$; nestin-*Cre* mice. It would be meaningful too, to observe if there is reactive gliosis in an Atg5 KO specific for macroglia (GFAP-*Cre*), to confirm if the phenotype observed in the *Sumf1*$^{flox/flox}$;GFAP-*Cre* mice is only due to autophagy and not to an alternative consequence of it. Also, as astrocytes and Müller cells are involved in the preservation of the blood retinal barrier, it would be interesting to examine the state of the vasculature and its permeability which, in the case of being altered, it could enhance the degeneration of the retina (Cuenca et al., 2015). Besides, we cannot forget that the macroglia function is in tight conjugation with microglia and the latter also contributes to maintain extracellular homeostasis. For instance, it carries out the clearance of extracellular amyloid-β in an Alzheimer's disease model, which is actually mediated through autophagy. It could be especially relevant in to observe the activation state of microglia by immunostaining of retinal cryosections, with Iba-1 or other specific labelling as CD11b, in the *Atg5* $^{flox/flox}$; nestin-*Cre* model, as autophagy is not compromised in microglia and there is an alteration of proteostasis (next section), and compare it with aged retina.

5.2.3. Proteostasis alteration in the absence of autophagy in the retina

For further understanding the consequences of the autophagy blockage in the retina, we checked if it was leading to the accumulation of proteins tagged for degradation in the cytoplasm (Komatsu et al., 2007), as it is a common hallmark of autophagy impairment and it was described to occur in the brain of *Atg5*$^{flox/flox}$; nestin-*Cre* and *Atg7*$^{flox/flox}$; nestin-*Cre* mice (Hara et al., 2006; Komatsu et al., 2006).

By westernblot analysis we found that p62 levels were drastically increased in the retinas of *Atg5*$^{flox/flox}$; nestin-*Cre* mice compared with control. The immunostaining of retinal cryosections with p62 antibody, showed that p62 was increased among all the layers of *Atg5*$^{flox/flox}$; nestin-*Cre* retinas, but more intensely in the IPL. The IPL does not host any nuclei of the neuroretinal cells, thus, the accumulation could be explained to happen in the processes of retinal neurons, or in the cytoplasm of macro or microglia. In the description of (Hara et al., 2006) and (Komatsu et al., 2006), they remark that ubiquitin (another protein accumulated during autophagy blockage and related to p62 (Rubinsztein et al., 2011)) is mainly accumulated in neurons. However, in the total body *Sumf1*$^{-/-}$ mouse, they found that, while ubiquitin was found both in neurons and glia, p62 was preferentially found in astrocytes (Di Malta et al., 2012). Also, a mouse model deficient in $PI(3,5)P_2$, which induces autophagy blockage, presents remarkable accumulation of p62 in astrocytes in other brain regions as cerebellum or thalamus, not in oligodendrocites and neither microglia (Ferguson et al., 2009). In the case of *Atg5*$^{flox/flox}$; nestin-*Cre* retinas it seems more probable that p62 is accumulated in the glia (macro or micro) as the accumulations of p62 are

too big to be inside of a neuron, which also fits with the presented bibliography. Considering that Müller cells feet are located in the IPL, it could be them accumulating p62 tagged proteins, but also could fit with the silhouette of active astrocytes. As well, microglia should not be discarded, as the images could also suggest a pattern of active microglia (Cuenca et al., 2015). A deeper observation of the distribution of p62 in the *Atg5*$^{flox/flox}$; nestin-*Cre* retinas at the ONL reveals a transversal print at the limit between the ONL and IS, where the outer limiting membrane lays. It is a network of adherens junctions between Müller cells and between them and photoreceptors, which is involved in maintaining the structure of the retina through mechanical strength but could also constitute a permeability barrier (Omri et al., 2010). Also, there is a shade of the inner limiting membrane, where there are placed the conical endfeet of the Muller cell also surrounding retinal blood vessels. Thus, this could hint that Müller cells and astrocytes could be involved in the observed pattern of p62 accumulation, which also agrees with the observed increase of GFAP in the tissue.

In aged retinas we also found an increase in p62 by western blot and immunostaining compared to 3 month controls. However, the pattern observed by immunostaining in cryosections differs a bit from the observed in *Atg5*$^{flox/flox}$; nestin-*Cre* mice, not only in intensity, showing a small proportion of accumulated proteins compared to *Atg5*$^{flox/flox}$; nestin-*Cre* mice, but also because the staining of p62 fits more into the shape of neuroretinal cells than into the one of glia. Then, macroautophagy seems to be relevant for macroglia, as hinted in *Atg5*$^{flox/flox}$; nestin-*Cre* retinas, but macroglia is less affected by the blockage of autophagy derived from aging. This could be explained because neurons are post-mitotic cells and thus less plastic cells and metabolically dependant on glia, whether macroglial cells are not post-mitotic cells and metabolically independent. Also, the impairment of autophagic flux in aging leads to the accumulation of inclusion bodies, which could interfere with the intracellular vesicle traffic.

For further confirmation of these assumptions, it would be interesting to perform an immunostaining for GFAP, Iba-1 and p62 in retinal cryosections of *Atg5*$^{flox/flox}$; nestin-*Cre* and aged retinas, in order to delimit the localization of p62.

5.2.4. Study of the link between macroautophagy and CMA during aging and neurodegeneration

We have seen that autophagy blockage in *Atg5*$^{flox/flox}$; nestin-*Cre* and aged retinas leaded to an alteration of the proteostasis that ended up in degeneration and macroglial activation. It is known that many neurodegenerative models, most of them linked with age, present impairment of the macroautophagic process, as Alzheimer disease (Nixon et al., 2005) or Huntington (Martinez-Vicente et al., 2010) and it has also been shown that there is compensation through the increase of the chaperone-mediated autophagy, more or less effective in many situations (Koga et al., 2011a; Wang et al., 2009). Thus, we checked if in our case of retinal degeneration caused by macroautophagic impairment CMA could be up-regulated to maintain cellular homeostasis.

Then, we checked levels of the protein LAMP-2A, the key protein of the process as it internalizes in the lysosome the proteins selected for CMA degradation. Indeed, LAMP-2A levels were elevated in *Atg5*$^{flox/flox}$; nestin-*Cre* and aged retinas among all the layers, especially in the OS of the photoreceptors, OPL and IPL, INL and CGL. We also checked the levels of the other main protein of the process, the Hsc70 chaperone. We found that Hsc70 was expressed in similar regions to LAMP-2A: OS of the photoreceptors, OPL, INL and CGL. Within the ONL, it was interesting to find that Hsc70 was much more accumulated in cones than in rods, even in control animals (Figure 4.17). This increase could be pointing out a compensatory mechanism carried out by CMA in the absence of macroautophagy in retinal tissue, but especially relevant in cones.

To verify this suggestion, we used an *in vitro* model: the 661w cells, a cell line derived from immortalized mouse cones. For that purpose, the *Atg7* and *LAMP-2A* genes were knocked down by lentiviral transfection, To determine CMA activity of the cells, they were transfected with the photoactivable reporter KFERQ-PA-mCherry1 (Koga et al., 2011b) This reporter allowed us to follow the proteins exposing the KFERQ motif, recognized by Hsc70 to be degraded by CMA lysosomes, and we observed that Atg7 KD cells presented higher CMA activity in basal conditions than the control cells, suggesting that there could be a compensation of the lack of macroautophagy with an increase of the CMA pathway in 661w cells. The cell lines were also challenged with a paraquat treatment, an inducer of oxidative stress, and we found that 661w cells with diminished CMA activity were more sensitive, presenting higher levels of cell death. Moreover, the macroautophagic activity of the cells was analyzed by anti-LC3 immunostaining, and it was quantified using the WimAutophagy tool. It determined that LAMP-2A KD cells had a reduced macroautophagic activity compared to control cells, indicating that no compensatory induction of macroautophagy was happening, and that the possible crosstalk between macroautophagy and CMA in 661w cells was only unidirectional. Thus, only the lack of macroautophagy would up-regulate CMA, but not vice versa.

Connecting these results with those obtained in the retinas of *Atg5*$^{flox/flox}$; nestin-*Cre* and aged mice, they could suggest that cones were presenting a more active CMA activity than rods in basal conditions and also after macroautophagic impairment. It could be in relation with the fact that cones present a higher consumption of energy (Okawa et al., 2008) and a 2-fold more mitochondria than rods (Perkins et al., 2003), which leads to more oxygen generation, where CMA could act as a protective mechanism against ROS. It is common that rods are more affected than cones by injuries or retinopathies (Cuenca et al., 2015), and a different energy metabolism could be underneath. It has been described in different models of retinitis pigmentosa that, during the beginning of cone cell death, LAMP-2A is increased in cones, but not in other cells (Punzo et al., 2009). They suggested that the photoreceptors of the retina present different metabolism and, thus, that cones are able to increase LAMP-2A and macroautophagy in response to the suffered starvation. Thus, CMA could be contributing in cones, not only as an antioxidant resource, but also as an energy supplier in starvation. Therefore, the exclusivity of CMA in cones suggests that it could be one of the advantages of

cones to cope with injuries and metabolism alterations compared to rods, whose metabolism would rely more on macroautophagy, since they are more affected than cones by the lack of Atg5 and they present low levels of Hsc70.

It could be interesting to test the importance of CMA for the cone metabolism and survival, and the relevance of macroautophagy for rods, by analyzing the phenotype of LAMP-2 KO mice retinas by performing a functional and morphological study similar to the exposed here. In the case that cones presented higher degree of degeneration than rods, it could denote that their survival abilities would rely mainly in CMA. In the case that degeneration occurred equally, it would only point that macroautophagy is basic for both and only CMA is important for cones under stress conditions.

Then, the greater or lesser participation of the different autophagic pathways in different types of cells could explain the different cell death rates observed under pathologies or degenerative processes. Thus, we were interested on studying the cerebellum of *Atg5*$^{flox/flox}$; nestin-*Cre* mice, which is a highly structured part of the brain and it presented different patterns of cell death in different subpopulations. It is described by Hara et al. (2006) that granular cell layer of the cerebellum of *Atg5*$^{flox/flox}$; nestin-*Cre* mice presents TUNEL staining, while Purkinje cell layer does not, even if this cells also undergo degeneration and disappear with time. Thus, we thought that a different involvement of CMA in these cell types could explain the cell-type specificity in the cell death pattern.

We re-checked the levels of p62 and ubiquitin by western blotting *Atg5*$^{flox/flox}$; nestin-*Cre* mice cerebellum and, indeed, both proteins were increased in *Atg5*$^{flox/flox}$; nestin-*Cre* mice, even if ubiquitin only shows a trend. We, then, analysed the levels of LAMP-2A and Hsc70 by westernblot, to test if CMA could be elevated in cerebellum too. In this case, only LAMP-2A was increased, which agrees with the fact that it is the limiting protein of the process (Kaushik and Cuervo, 2012). To asses if LAMP-2A was differentially present in a cell type or another, we performed an immunostaining, in combination with p62, to observe at the same time the level of proteostasis alteration derived from macroautophagy blockage in the cell subsets. In fact, we found that LAMP-2A and p62 presented an exclusion pattern. Purkinje cells presented higher levels of LAMP-2A positive lysosomes, while granule cells presented a great accumulation of p62 in their cytoplasm. This could suggest that both cell types are facing the alteration of proteostasis, but Purkinje cells would be able to increase CMA activity and get protected from cell death for a longer time. It could be interesting in this case too, as in retina, to have a more physiological point of view by culturing Purkinje and granule cells from control and *Atg5*$^{flox/flox}$; nestin-*Cre* mice and measuring the CMA and macroautophagic activities, as performed in 661w cells. Also, it would complete the perspective, to study the phenotype of cell death in cerebellum in LAMP-2 KO mice, for confirming the relative importance of CMA and macroautophagy for the different subsets of cells.

Therefore, both observations in retina and cerebellum suggest that a different implication of the autophagic pathways could explain the greater or lesser protection under stress conditions in different cell types.

6. CONCLUSIONS

6. CONCLUSIONS

- The elimination of the autophagic gene Atg5 in neural precursors in mice induces neurodegeneration of the retina. It mainly affects rods and their downstream neurons rod bipolar cells, leading to a diminished scotopic vision.
- The elimination of the autophagic gene Atg5 in neural precursors, and the associated neurodegeneration, induces the activation of astrocites in mouse retina. This activation is also observed in aged retinas.
- The absence of the autophagic gene Atg5 in neural precursors and the decline of autophagy derived from aging both induce alterations on proteostasis including p62 accumulation, but with different patterns of distribution.
- Elimination of the autophagic gene Atg5 in neural precursors increases the presence of CMA-related proteins LAMP-2A and Hsc70 in the retina, as a possible compensatory response. CMA related proteins are also increased in mouse retina during aging.
- There is a differential pattern of CMA proteins among photoreceptors. Only cones, but not rods, are able to increase their levels in the studied models.
- The lack of macroautophagy in vitro in 661W cells induces a compensatory increment of chaperone mediated autophagy. However, the lack of chaperone mediated autophagy renders the cells more sensitive to oxidative stress, indicating the existence of a unidirectional crosstalk between the two pathways.
- In the cerebellum elimination of the autophagic gene Atg5 in neural precursors in mice induces an increase of the levels of p62 in the granular layer and also an increase of the chaperone-mediated autophagy LAMP-2A protein in Purkinje cells.
- In collaboration with Wimasis Company we have validated two modules for automatized imaging analysis of autophagy and apoptosis assays, designed to be applied on different samples and with different labelling, making them reliable and powerful tools for the study of neurodegeneration and other disease states.

7. BIBLIOGRAPHY

7. BIBLIOGRAPHY

Abada, A., and Elazar, Z. (2014). Getting ready for building: signaling and autophagosome biogenesis. EMBO Rep *15*, 839-852.

Aniento, F., Papavassiliou, A.G., Knecht, E., and Roche, E. (1996). Selective uptake and degradation of c-Fos and v-Fos by rat liver lysosomes. FEBS Lett *390*, 47-52.

Apps, R., and Garwicz, M. (2005). Anatomical and physiological foundations of cerebellar information processing. Nat Rev Neurosci *6*, 297-311.

Ashford TP, P.K. (1962). CYTOPLASMIC COMPONENTS IN HEPATIC CELL LYSOSOMES. The Journal of Cell Biology *12*, 198-202.

Athanasiou, D., Aguila, M., Bevilacqua, D., Novoselov, S.S., Parfitt, D.A., and Cheetham, M.E. (2013). The cell stress machinery and retinal degeneration. FEBS Lett *587*, 2008-2017.

Barber, A.J., Antonetti, D.A., and Gardner, T.W. (2000). Altered expression of retinal occludin and glial fibrillary acidic protein in experimental diabetes. The Penn State Retina Research Group. Invest Ophthalmol Vis Sci *41*, 3561-3568.

Barhoum, R., Martinez-Navarrete, G., Corrochano, S., Germain, F., Fernandez-Sanchez, L., de la Rosa, E.J., de la Villa, P., and Cuenca, N. (2008). Functional and structural modifications during retinal degeneration in the rd10 mouse. Neuroscience *155*, 698-713.

Barnett, N.L., and Pow, D.V. (2000). Antisense knockdown of GLAST, a glial glutamate transporter, compromises retinal function. Invest Ophthalmol Vis Sci *41*, 585-591.

Boya, P. (2012). Autophagy in the retina: development, physiology and pathology. In Autophagy of the Nervous System Z. Yue, and C.T. Chu, eds., pp. 149-173.

Boya, P., and Codogno, P. (2013). Cell biology: Recycling in sight. Nature *501*, 40-42.

Boya, P., Reggiori, F., and Codogno, P. (2013). Emerging regulation and functions of autophagy. Nat Cell Biol *15*, 713-720.

Cappellano, G., Carecchio, M., Fleetwood, T., Magistrelli, L., Cantello, R., Dianzani, U., and Comi, C. (2013). Immunity and inflammation in neurodegenerative diseases. American journal of neurodegenerative disease *2*, 89-107.

Coorey, N.J., Shen, W., Chung, S.H., Zhu, L., and Gillies, M.C. (2012). The role of glia in retinal vascular disease. Clinical & experimental optometry : journal of the Australian Optometrical Association *95*, 266-281.

Cuenca, N., Fernandez-Sanchez, L., Campello, L., Maneu, V., De la Villa, P., Lax, P., and Pinilla, I. (2015). Cellular responses following retinal injuries and therapeutic approaches for neurodegenerative diseases. Prog Retin Eye Res.

Cuenca, N., Pinilla, I., Sauve, Y., Lu, B., Wang, S., and Lund, R.D. (2004). Regressive and reactive changes in the connectivity patterns of rod and cone pathways of P23H transgenic rat retina. Neuroscience *127*, 301-317.

Cuervo, A.M., and Dice, J.F. (2000). Regulation of lamp2a levels in the lysosomal membrane. Traffic *1*, 570-583.

Cuervo, A.M., Hu, W., Lim, B., and Dice, J.F. (1998). IkappaB is a substrate for a selective pathway of lysosomal proteolysis. Mol Biol Cell *9*, 1995-2010.

Cuervo, A.M., Palmer, A., Rivett, A.J., and Knecht, E. (1995). Degradation of proteasomes by lysosomes in rat liver. Eur J Biochem *227*, 792-800.

Cuervo, A.M., and Wong, E. (2014). Chaperone-mediated autophagy: roles in disease and aging. Cell Res *24*, 92-104.

Chen, Y., Sawada, O., Kohno, H., Le, Y.Z., Subauste, C., Maeda, T., and Maeda, A. (2013). Autophagy protects the retina from light-induced degeneration. J Biol Chem *288*, 7506-7518.

Chu, C.T., Plowey, E.D., Dagda, R.K., Hickey, R.W., Cherra, S.J., 3rd, and Clark, R.S. (2009). Autophagy in neurite injury and neurodegeneration: in vitro and in vivo models. Methods Enzymol *453*, 217-249.

D'Orazi, F.D., Suzuki, S.C., and Wong, R.O. (2014). Neuronal remodeling in retinal circuit assembly, disassembly, and reassembly. Trends Neurosci *37*, 594-603.

Dagda, R.K., Zhu, J., Kulich, S.M., and Chu, C.T. (2008). Mitochondrially localized ERK2 regulates mitophagy and autophagic cell stress: implications for Parkinson's disease. Autophagy *4*, 770-782.

Dahlstrand, J., Lardelli, M., and Lendahl, U. (1995). Nestin mRNA expression correlates with the central nervous system progenitor cell state in many, but not all, regions of developing central nervous system. Brain research Developmental brain research *84*, 109-129.

Deter, R.L., Baudhuin, P., and De Duve, C. (1967). Participation of lysosomes in cellular autophagy induced in rat liver by glucagon. J Cell Biol *35*, C11-16.

Deter, R.L., and De Duve, C. (1967). Influence of glucagon, an inducer of cellular autophagy, on some physical properties of rat liver lysosomes. J Cell Biol *33*, 437-449.

Di Bartolomeo, S., Corazzari, M., Nazio, F., Oliverio, S., Lisi, G., Antonioli, M., Pagliarini, V., Matteoni, S., Fuoco, C., Giunta, L.*, et al.* (2010). The dynamic interaction of AMBRA1 with the dynein motor complex regulates mammalian autophagy. J Cell Biol *191*, 155-168.

Di Malta, C., Fryer, J.D., Settembre, C., and Ballabio, A. (2012). Autophagy in astrocytes: a novel culprit in lysosomal storage disorders. Autophagy *8*, 1871-1872.

Dohi, E., Tanaka, S., Seki, T., Miyagi, T., Hide, I., Takahashi, T., Matsumoto, M., and Sakai, N. (2012). Hypoxic stress activates chaperone-mediated autophagy and modulates neuronal cell survival. Neurochemistry international *60*, 431-442.

Edwards, M.M., Rodriguez, J.J., Gutierrez-Lanza, R., Yates, J., Verkhratsky, A., and Lutty, G.A. (2014). Retinal macroglia changes in a triple transgenic mouse model of Alzheimer's disease. Exp Eye Res *127*, 252-260.

Efeyan, A., Zoncu, R., Chang, S., Gumper, I., Snitkin, H., Wolfson, R.L., Kirak, O., Sabatini, D.D., and Sabatini, D.M. (2013). Regulation of mTORC1 by the Rag GTPases is necessary for neonatal autophagy and survival. Nature *493*, 679-683.

Esteve-Rudd, J., Fernandez-Sanchez, L., Lax, P., De Juan, E., Martin-Nieto, J., and Cuenca, N. (2011). Rotenone induces degeneration of photoreceptors and impairs the dopaminergic system in the rat retina. Neurobiol Dis *44*, 102-115.

Ezaki, J., Matsumoto, N., Takeda-Ezaki, M., Komatsu, M., Takahashi, K., Hiraoka, Y., Taka, H., Fujimura, T., Takehana, K., Yoshida, M.*, et al.* (2011). Liver autophagy contributes to the maintenance of blood glucose and amino acid levels. Autophagy *7*, 727-736.

Ferguson, C.J., Lenk, G.M., and Meisler, M.H. (2009). Defective autophagy in neurons and astrocytes from mice deficient in PI(3,5)P2. Hum Mol Genet *18*, 4868-4878.

Fisher, S.K., Lewis, G.P., Linberg, K.A., Barawid, E., and Verardo, M.R. (1995). Cellular Remodeling in Mammalian Retina Induced by Retinal Detachment. In Webvision: The Organization of the Retina and Visual System, H. Kolb, E. Fernandez, and R. Nelson, eds. (Salt Lake City UT).

Formichella, C.R., Abella, S.K., Sims, S.M., Cathcart, H.M., and Sappington, R.M. Astrocyte Reactivity: A Biomarker for Retinal Ganglion Cell Health in Retinal Neurodegeneration. Journal of clinical & cellular immunology *5*.

Frake, R.A., Ricketts, T., Menzies, F.M., and Rubinsztein, D.C. (2015). Autophagy and neurodegeneration. J Clin Invest *125*, 65-74.

Galluzzi, L., Bravo-San Pedro, J.M., Vitale, I., Aaronson, S.A., Abrams, J.M., Adam, D., Alnemri, E.S., Altucci, L., Andrews, D., Annicchiarico-Petruzzelli, M.*, et al.* (2015). Essential versus accessory aspects of cell death: recommendations of the NCCD 2015. Cell Death Differ *22*, 58-73.

Ghavami, S., Shojaei, S., Yeganeh, B., Ande, S.R., Jangamreddy, J.R., Mehrpour, M., Christoffersson, J., Chaabane, W., Moghadam, A.R., Kashani, H.H.*, et al.* (2014). Autophagy and apoptosis dysfunction in neurodegenerative disorders. Prog Neurobiol *112*, 24-49.

Gibson, S.B. (2013). Investigating the role of reactive oxygen species in regulating autophagy. Methods Enzymol *528*, 217-235.

Gwinn, D.M., Shackelford, D.B., Egan, D.F., Mihaylova, M.M., Mery, A., Vasquez, D.S., Turk, B.E., and Shaw, R.J. (2008). AMPK phosphorylation of raptor mediates a metabolic checkpoint. Mol Cell *30*, 214-226.

Hamasaki, M., Shibutani, S.T., and Yoshimori, T. (2013). Up-to-date membrane biogenesis in the autophagosome formation. Curr Opin Cell Biol *25*, 455-460.

Hara, T., Nakamura, K., Matsui, M., Yamamoto, A., Nakahara, Y., Suzuki-Migishima, R., Yokoyama, M., Mishima, K., Saito, I., Okano, H.*, et al.* (2006). Suppression of basal autophagy in neural cells causes neurodegenerative disease in mice. Nature *441*, 885-889.

Harding, T.M., Morano, K.A., Scott, S.V., and Klionsky, D.J. (1995). Isolation and characterization of yeast mutants in the cytoplasm to vacuole protein targeting pathway. J Cell Biol *131*, 591-602.

Hoon, M., Okawa, H., Della Santina, L., and Wong, R.O. (2014). Functional architecture of the retina: Development and disease. Prog Retin Eye Res *42C*, 44-84.

Hubbi, M.E., Hu, H., Kshitiz, Ahmed, I., Levchenko, A., and Semenza, G.L. (2013). Chaperone-mediated autophagy targets hypoxia-inducible factor-1alpha (HIF-1alpha) for lysosomal degradation. J Biol Chem *288*, 10703-10714.

Inoki, K., Li, Y., Zhu, T., Wu, J., and Guan, K.L. (2002). TSC2 is phosphorylated and inhibited by Akt and suppresses mTOR signalling. Nat Cell Biol *4*, 648-657.

Jin, M., and Klionsky, D.J. (2014). Regulation of autophagy: modulation of the size and number of autophagosomes. FEBS Lett *588*, 2457-2463.

Jung, C.H., Jun, C.B., Ro, S.H., Kim, Y.M., Otto, N.M., Cao, J., Kundu, M., and Kim, D.H. (2009). ULK-Atg13-FIP200 complexes mediate mTOR signaling to the autophagy machinery. Mol Biol Cell *20*, 1992-2003.

Kabeya, Y., Mizushima, N., Ueno, T., Yamamoto, A., Kirisako, T., Noda, T., Kominami, E., Ohsumi, Y., and Yoshimori, T. (2000). LC3, a mammalian homologue of yeast Apg8p, is localized in autophagosome membranes after processing. The EMBO journal *19*, 5720-5728.

Kaushik, S., and Cuervo, A.M. (2012). Chaperone-mediated autophagy: a unique way to enter the lysosome world. Trends Cell Biol *22*, 407-417.

Kaushik, S., Massey, A.C., Mizushima, N., and Cuervo, A.M. (2008). Constitutive activation of chaperone-mediated autophagy in cells with impaired macroautophagy. Mol Biol Cell *19*, 2179-2192.

Kihara, Noda, Ishihara, and Ohsumi (2001). Two Distinct Vps34 Phosphatidylinositol 3–Kinase Complexes Function in Autophagy and Carboxypeptidase Y Sorting in Saccharomyces cerevisiae. The Journal of Cell Biology *152*, 519-530.

Kim, J., Kim, Y.C., Fang, C., Russell, R.C., Kim, J.H., Fan, W., Liu, R., Zhong, Q., and Guan, K.L. (2013a). Differential Regulation of Distinct Vps34 Complexes by AMPK in Nutrient Stress and Autophagy. Cell *152*, 290-303.

Kim, J.Y., Zhao, H., Martinez, J., Doggett, T.A., Kolesnikov, A.V., Tang, P.H., Ablonczy, Z., Chan, C.C., Zhou, Z., Green, D.R.*, et al.* (2013b). Noncanonical autophagy promotes the visual cycle. Cell *154*, 365-376.

Kim, Y.C., and Guan, K.L. (2015). mTOR: a pharmacologic target for autophagy regulation. J Clin Invest *125*, 25-32.

Klionsky, D.J. (2008). Autophagy revisited: a conversation with Christian de Duve. Autophagy *4*, 740-743.

Klionsky, D.J., Abdalla, F.C., Abeliovich, H., Abraham, R.T., Acevedo-Arozena, A., Adeli, K., Agholme, L., Agnello, M., Agostinis, P., Aguirre-Ghiso, J.A.*, et al.* (2012). Guidelines for the use and interpretation of assays for monitoring autophagy. Autophagy *8*, 445-544.

Klionsky, D.J., Cregg, J.M., Dunn, W.A., Emr, S.D., Sakai, Y., Sandoval, I.V., Sibirny, A., Subramani, S., Thumm, M., Veenhuis, M.*, et al.* (2003). A unified nomenclature for yeast autophagy-related genes. *5*, 539-545.

Klionsky, D.J., Cuervo, A.M., and Seglen, P.O. (2007). Methods for monitoring autophagy from yeast to human. Autophagy *3*, 181-206.

Koga, H., Martinez-Vicente, M., Arias, E., Kaushik, S., Sulzer, D., and Cuervo, A.M. (2011a). Constitutive upregulation of chaperone-mediated autophagy in Huntington's disease. J Neurosci *31*, 18492-18505.

Koga, H., Martinez-Vicente, M., Macian, F., Verkhusha, V.V., and Cuervo, A.M. (2011b). A photoconvertible fluorescent reporter to track chaperone-mediated autophagy. Nat Commun *2*, 386.

Kolb, H. (2003). How the retina works. American Scientist *91*, 28-35.

Kolb, H. (2013 ed). Glial cells of the Retina, Webvision: The Organization of the Retina and Visual System.

Kolesnikov, A.V., Fan, J., Crouch, R.K., and Kefalov, V.J. (2010a). Age-related deterioration of rod vision in mice. J Neurosci *30*, 11222-11231.

Kolesnikov, A.V., Fan, J., Crouch, R.K., and Kefalov, V.J. (2010b). Age-Related Deterioration of Rod Vision in Mice. The Journal of neuroscience *30*, 11222-11231.

Komatsu, M., Waguri, S., Chiba, T., Murata, S., Iwata, J., Tanida, I., Ueno, T., Koike, M., Uchiyama, Y., Kominami, E.*, et al.* (2006). Loss of autophagy in the central nervous system causes neurodegeneration in mice. Nature *441*, 880-884.

Komatsu, M., Waguri, S., Koike, M., Sou, Y.S., Ueno, T., Hara, T., Mizushima, N., Iwata, J., Ezaki, J., Murata, S.*, et al.* (2007). Homeostatic levels of p62 control cytoplasmic inclusion body formation in autophagy-deficient mice. Cell *131*, 1149-1163.

Koyama-Honda, I., Itakura, E., Fujiwara, T.K., and Mizushima, N. (2013). Temporal analysis of recruitment of mammalian ATG proteins to the autophagosome formation site. Autophagy *9*, 1491-1499.

Krantic, S., and Torriglia, A. (2014). Retina: source of the earliest biomarkers for Alzheimer's disease? J Alzheimers Dis *40*, 237-243.

Kroemer, G., Galluzzi, L., Vandenabeele, P., Abrams, J., Alnemri, E., Baehrecke, E., Blagosklonny, M., El-Deiry, W., Golstein, P., Green, D.*, et al.* (2009). Classification of cell death: recommendations of the Nomenclature Committee on Cell Death 2009. Cell Death Differ *16*, 3-11.

Kuma, A., Hatano, M., Matsui, M., Yamamoto, A., Nakaya, H., Yoshimori, T., Ohsumi, Y., Tokuhisa, T., and Mizushima, N. (2004). The role of autophagy during the early neonatal starvation period. Nature *432*, 1032-1036.

Lalaoui, N., Lindqvist, L.M., Sandow, J.J., and Ekert, P.G. (2015). The molecular relationships between apoptosis, autophagy and necroptosis. Semin Cell Dev Biol.

Lamark, T., Kirkin, V., Dikic, I., and Johansen, T. (2009). NBR1 and p62 as cargo receptors for selective autophagy of ubiquitinated targets. Cell Cycle *8*, 1986-1990.

Lamb, C.A., Yoshimori, T., and Tooze, S.A. (2013). The autophagosome: origins unknown, biogenesis complex. Nat Rev Mol Cell Biol *14*, 759-774.

Lee, J.H., Yu, W.H., Kumar, A., Lee, S., Mohan, P.S., Peterhoff, C.M., Wolfe, D.M., Martinez-Vicente, M., Massey, A.C., Sovak, G.*, et al.* (2010). Lysosomal proteolysis and autophagy require presenilin 1 and are disrupted by Alzheimer-related PS1 mutations. Cell *141*, 1146-1158.

Lee, S., Sato, Y., and Nixon, R.A. (2011). Lysosomal proteolysis inhibition selectively disrupts axonal transport of degradative organelles and causes an Alzheimer's-like axonal dystrophy. J Neurosci *31*, 7817-7830.

Liang, C.C., Wang, C., Peng, X., Gan, B., and Guan, J.L. (2010). Neural-specific deletion of FIP200 leads to cerebellar degeneration caused by increased neuronal death and axon degeneration. J Biol Chem *285*, 3499-3509.

Lin, S.Y., Li, T.Y., Liu, Q., Zhang, C., Li, X., Chen, Y., Zhang, S.M., Lian, G., Ruan, K., Wang, Z.*, et al.* (2012). GSK3-TIP60-ULK1 signaling pathway links growth factor deprivation to autophagy. Science *336*, 477-481.

Lippai, M., and Low, P. (2014). The role of the selective adaptor p62 and ubiquitin-like proteins in autophagy. BioMed research international *2014*, 832704.

Lopez-Otin, C., Blasco, M.A., Partridge, L., Serrano, M., and Kroemer, G. (2013). The hallmarks of aging. Cell *153*, 1194-1217.

Mailand, N., Podtelejnikov, A.V., Groth, A., Mann, M., Bartek, J., and Lukas, J. (2002). Regulation of G(2)/M events by Cdc25A through phosphorylation-dependent modulation of its stability. EMBO J *21*, 5911-5920.

Mansour, H., Chamberlain, C.G., Weible, M.W., 2nd, Hughes, S., Chu, Y., and Chan-Ling, T. (2008). Aging-related changes in astrocytes in the rat retina: imbalance between cell proliferation and cell death reduces astrocyte availability. Aging Cell *7*, 526-540.

Marchena, M., Lara, J., Aijon, J., Germain, F., de la Villa, P., and Velasco, A. (2011). The retina of the PCD/PCD mouse as a model of photoreceptor degeneration. A structural and functional study. Exp Eye Res *93*, 607-617.

Martin, D.D., Ladha, S., Ehrnhoefer, D.E., and Hayden, M.R. (2015). Autophagy in Huntington disease and huntingtin in autophagy. Trends Neurosci *38*, 26-35.

Martinez-Fernandez de la Camara, C., Salom, D., Sequedo, M.D., Hervas, D., Marin-Lambies, C., Aller, E., Jaijo, T., Diaz-Llopis, M., Millan, J.M., and Rodrigo, R. (2013). Altered antioxidant-oxidant status in the aqueous humor and peripheral blood of patients with retinitis pigmentosa. PloS one *8*, e74223.

Martinez-Vicente, M., Talloczy, Z., Wong, E., Tang, G., Koga, H., Kaushik, S., de Vries, R., Arias, E., Harris, S., Sulzer, D.*, et al.* (2010). Cargo recognition failure is responsible for inefficient autophagy in Huntington's disease. Nat Neurosci *13*, 567-576.

Massey, A.C., Kaushik, S., Sovak, G., Kiffin, R., and Cuervo, A.M. (2006). Consequences of the selective blockage of chaperone-mediated autophagy. Proc Natl Acad Sci U S A *103*, 5805-5810.

Mazzoni, F., Novelli, E., and Strettoi, E. (2008). Retinal ganglion cells survive and maintain normal dendritic morphology in a mouse model of inherited photoreceptor degeneration. J Neurosci *28*, 14282-14292.

McFarlane, S., Aitken, J., Sutherland, J.S., Nicholl, M.J., Preston, V.G., and Preston, C.M. (2011). Early induction of autophagy in human fibroblasts after infection with human cytomegalovirus or herpes simplex virus 1. J Virol *85*, 4212-4221.

McGill, T.J., Prusky, G.T., Luna, G., LaVail, M.M., Fisher, S.K., and Lewis, G.P. (2012). Optomotor and immunohistochemical changes in the juvenile S334ter rat. Exp Eye Res *104*, 65-73.

Mellén, M.A., de la Rosa, E.J., and Boya, P. (2008). The autophagic machinery is necessary for removal of cell corpses from the developing retinal neuroepithelium. Cell Death Differ *15*, 1279-1290.

Mitter, S.K., Song, C., Qi, X., Mao, H., Rao, H., Akin, D., Lewin, A., Grant, M., Dunn, W., Jr., Ding, J.*, et al.* (2014). Dysregulated autophagy in the RPE is associated with increased susceptibility to oxidative stress and AMD. Autophagy *10*, 1989-2005.

Mizushima, N. (2007). Autophagy: process and function. Genes Dev *21*, 2861-2873.

Mizushima, N., and Levine, B. (2010). Autophagy in mammalian development and differentiation. Nat Cell Biol *12*, 823-830.

Mizushima, N., Levine, B., Cuervo, A.M., and Klionsky, D.J. (2008). Autophagy fights disease through cellular self-digestion. Nature *451*, 1069-1075.

Mizushima, N., Noda, T., Yoshimori, T., Tanaka, Y., Ishii, T., George, M.D., Klionsky, D.J., Ohsumi, M., and Ohsumi, Y. (1998). A protein conjugation system essential for autophagy. Nature *395*, 395-398.

Mizushima, N., Yamamoto, A., Matsui, M., Yoshimori, T., and Ohsumi, Y. (2004). In vivo analysis of autophagy in response to nutrient starvation using transgenic mice expressing a fluorescent autophagosome marker. Mol Biol Cell *15*, 1101-1111.

Mizushima, N., Yoshimori, T., and Levine, B. (2010). Methods in mammalian autophagy research. Cell *140*, 313-326.

Mizushima, N., Yoshimori, T., and Ohsumi, Y. (2011). The role of atg proteins in autophagosome formation. Annu Rev Cell Dev Biol *27*, 107-132.

Mukaiyama, H., Oku, M., Baba, M., Samizo, T., Hammond, A.T., Glick, B.S., Kato, N., and Sakai, Y. (2002). Paz2 and 13 other PAZ gene products regulate vacuolar engulfment of peroxisomes during micropexophagy. Genes Cells *7*, 75-90.

Nilsson, P., Loganathan, K., Sekiguchi, M., Matsuba, Y., Hui, K., Tsubuki, S., Tanaka, M., Iwata, N., Saito, T., and Saido, T.C. (2013). Abeta secretion and plaque formation depend on autophagy. Cell reports *5*, 61-69.

Nixon, R.A. (2013). The role of autophagy in neurodegenerative disease. Nat Med *19*, 983-997.

Nixon, R.A., Wegiel, J., Kumar, A., Yu, W.H., Peterhoff, C., Cataldo, A., and Cuervo, A.M. (2005). Extensive involvement of autophagy in Alzheimer disease: an immuno-electron microscopy study. Journal of neuropathology and experimental neurology *64*, 113-122.

Novikoff, A.B. (1963). Lysosomes in the Physiology and Pathology of Cells: Contributions of Staining Methods. In Ciba Foundation Symposium - Anterior Pituitary Secretion (Book I of Colloquia on Endocrinology) (John Wiley & Sons, Ltd), pp. 36-77.

Ochaba, J., Lukacsovich, T., Csikos, G., Zheng, S., Margulis, J., Salazar, L., Mao, K., Lau, A.L., Yeung, S.Y., Humbert, S*., et al.* (2014). Potential function for the Huntingtin protein as a scaffold for selective autophagy. Proc Natl Acad Sci U S A *111*, 16889-16894.

Okawa, H., Sampath, A.P., Laughlin, S.B., and Fain, G.L. (2008). ATP consumption by mammalian rod photoreceptors in darkness and in light. Curr Biol *18*, 1917-1921.

Omri, S., Omri, B., Savoldelli, M., Jonet, L., Thillaye-Goldenberg, B., Thuret, G., Gain, P., Jeanny, J.C., Crisanti, P., and Behar-Cohen, F. (2010). The outer limiting membrane (OLM) revisited: clinical implications. Clinical ophthalmology (Auckland, NZ) *4*, 183-195.

Paulus, W., Schwarz, G., Werner, A., Lange, H., Bayer, A., Hofschuster, M., Muller, N., and Zrenner, E. (1993). Impairment of retinal increment thresholds in Huntington's disease. Ann Neurol *34*, 574-578.

Pekny, M., Wilhelmsson, U., and Pekna, M. (2014). The dual role of astrocyte activation and reactive gliosis. Neuroscience letters *565*, 30-38.

Perkins, G.A., Ellisman, M.H., and Fox, D.A. (2003). Three-dimensional analysis of mouse rod and cone mitochondrial cristae architecture: bioenergetic and functional implications. Mol Vis *9*, 60-73.

Pinilla, I., Lund, R.D., and Sauve, Y. (2005). Enhanced cone dysfunction in rats homozygous for the P23H rhodopsin mutation. Neuroscience letters *382*, 16-21.

Przedborski, S., Vila, M., and Jackson-Lewis, V. (2003a). Neurodegeneration: what is it and where are we? J Clin Invest *111*, 3-10.

Przedborski, S., Vila, M., and Jackson-Lewis, V. (2003b). Series Introduction: Neurodegeneration: What is it and where are we? Journal of Clinical Investigation *111*, 3-10.

Puelles López, L., Martínez Pérez, S., and Martínez de la Torre, M. (2008). Neuroanatomía.

Punzo, C., Kornacker, K., and Cepko, C.L. (2009). Stimulation of the insulin/mTOR pathway delays cone death in a mouse model of retinitis pigmentosa. Nat Neurosci *12*, 44-52.

Qu, X., Yu, J., Bhagat, G., Furuya, N., Hibshoosh, H., Troxel, A., Rosen, J., Eskelinen, E.-L., Mizushima, N., and Ohsumi, Y. (2003). Promotion of tumorigenesis by heterozygous disruption of the beclin 1 autophagy gene. Journal of Clinical Investigation *112*, 1809.

Ragauskas, S., Leinonen, H., Puranen, J., Ronkko, S., Nymark, S., Gurevicius, K., Lipponen, A., Kontkanen, O., Puolivali, J., Tanila, H.*, et al.* (2014). Early retinal function deficit without prominent morphological changes in the R6/2 mouse model of Huntington's disease. PloS one *9*, e113317.

Rajagopal, D., Bal, V., Mayor, S., George, A., and Rath, S. (2006). A role for the Hsp90 molecular chaperone family in antigen presentation to T lymphocytes via major histocompatibility complex class II molecules. European journal of immunology *36*, 828-841.

Ravikumar, B., Vacher, C., Berger, Z., Davies, J.E., Luo, S., Oroz, L.G., Scaravilli, F., Easton, D.F., Duden, R., O'Kane, C.J.*, et al.* (2004). Inhibition of mTOR induces autophagy and reduces toxicity of polyglutamine expansions in fly and mouse models of Huntington disease. Nat Genet *36*, 585-595.

Reme, C.E., Wolfrum, U., Imsand, C., Hafezi, F., and Williams, T.P. (1999). Photoreceptor autophagy: effects of light history on number and opsin content of degradative vacuoles. Invest Ophthalmol Vis Sci *40*, 2398-2404.

Renna, Schaffner, Winslow, Menzies, Peden, Floto, and Rubinsztein (2011). Autophagic substrate clearance requires activity of the syntaxin-5 SNARE complex. J Cell Sci *124*, 469-482.

Rodríguez-Muela, N. (2011). Función de la autofagia en modelos degenerativos del sistema nervioso.

Rodriguez-Muela, N., Germain, F., Marino, G., Fitze, P.S., and Boya, P. (2012). Autophagy promotes survival of retinal ganglion cells after optic nerve axotomy in mice. Cell Death Differ *19*, 162-169.

Rodriguez-Muela, N., Hernandez-Pinto, A.M., Serrano-Puebla, A., Garcia-Ledo, L., Latorre, S.H., de la Rosa, E.J., and Boya, P. (2015). Lysosomal membrane permeabilization and autophagy blockade contribute to photoreceptor cell death in a mouse model of retinitis pigmentosa. Cell Death Differ *22*, 476-487.

Rodriguez-Muela, N., Koga, H., Garcia-Ledo, L., de la Villa, P., de la Rosa, E.J., Cuervo, A.M., and Boya, P. (2013). Balance between autophagic pathways preserves retinal homeostasis. Aging Cell *12*, 478-488.

Rogov, V., Dotsch, V., Johansen, T., and Kirkin, V. (2014). Interactions between autophagy receptors and ubiquitin-like proteins form the molecular basis for selective autophagy. Mol Cell *53*, 167-178.

Romijn, H.J., de Jong, B.M., and Ruijter, J.M. (1988). A procedure for culturing rat neocortex explants in a serum-free nutrient medium. Journal of neuroscience methods *23*, 75-83.

Rubinsztein, D.C., Marino, G., and Kroemer, G. (2011). Autophagy and aging. Cell *146*, 682-695.

Sakai, T., Tsuneoka, H., Lewis, G.P., and Fisher, S.K. (2014). Remodelling of retinal on- and off-bipolar cells following experimental retinal detachment. Clinical & experimental ophthalmology *42*, 480-485.

Sakai, Y., Koller, A., Rangell, L.K., Keller, G.A., and Subramani, S. (1998). Peroxisome degradation by microautophagy in Pichia pastoris: identification of specific steps and morphological intermediates. J Cell Biol *141*, 625-636.

Sancak, Y., Bar-Peled, L., Zoncu, R., Markhard, A.L., Nada, S., and Sabatini, D.M. (2010). Ragulator-Rag complex targets mTORC1 to the lysosomal surface and is necessary for its activation by amino acids. Cell *141*, 290-303.

Sarkar (2013). Regulation of autophagy by mTOR-dependent and mTOR-independent pathways: autophagy dysfunction in neurodegenerative diseases and therapeutic application of autophagy enhancers. Biochem Soc Trans *41*, 1103-1130.

Scherz-Shouval, R., and Elazar, Z. (2011). Regulation of autophagy by ROS: physiology and pathology. Trends Biochem Sci *36*, 30-38.

Schneider, J.L., and Cuervo, A.M. (2014). Autophagy and human disease: emerging themes. Curr Opin Genet Dev *26C*, 16-23.

Schneider, J.L., Villarroya, J., Diaz-Carretero, A., Patel, B., Urbanska, A.M., Thi, M.M., Villarroya, F., Santambrogio, L., and Cuervo, A.M. (2015). Loss of hepatic chaperone-mediated autophagy accelerates proteostasis failure in aging. Aging Cell *14*, 249-264.

Singh, R., and Cuervo, A.M. (2011). Autophagy in the cellular energetic balance. Cell Metab *13*, 495-504.

Singh, R., Kaushik, S., Wang, Y., Xiang, Y., Novak, I., Komatsu, M., Tanaka, K., Cuervo, A.M., and Czaja, M.J. (2009). Autophagy regulates lipid metabolism. Nature *458*, 1131-1135.

Sou, Y.S., Waguri, S., Iwata, J., Ueno, T., Fujimura, T., Hara, T., Sawada, N., Yamada, A., Mizushima, N., Uchiyama, Y.*, et al.* (2008). The Atg8 conjugation system is indispensable for proper development of autophagic isolation membranes in mice. Mol Biol Cell *19*, 4762-4775.

Strettoi, E., Pignatelli, V., Rossi, C., Porciatti, V., and Falsini, B. (2003). Remodeling of second-order neurons in the retina of rd/rd mutant mice. Vision Research *43*, 867-877.

Strettoi, E., Porciatti, V., Falsini, B., Pignatelli, V., and Rossi, C. (2002). Morphological and functional abnormalities in the inner retina of the rd/rd mouse. J Neurosci *22*, 5492-5504.

Tan, E., Ding, X.Q., Saadi, A., Agarwal, N., Naash, M.I., and Al-Ubaidi, M.R. (2004). Expression of cone-photoreceptor-specific antigens in a cell line derived from retinal tumors in transgenic mice. Invest Ophthalmol Vis Sci *45*, 764-768.

Tanaka, K., and Matsuda, N. (2014). Proteostasis and neurodegeneration: the roles of proteasomal degradation and autophagy. Biochim Biophys Acta *1843*, 197-204.

Tang, P.H., Kono, M., Koutalos, Y., Ablonczy, Z., and Crouch, R.K. (2013). New insights into retinoid metabolism and cycling within the retina. Prog Retin Eye Res *32*, 48-63.

Terman, A., Kurz, T., Navratil, M., Arriaga, E.A., and Brunk, U.T. (2010). Mitochondrial turnover and aging of long-lived postmitotic cells: the mitochondrial-lysosomal axis theory of aging. Antioxid Redox Signal *12*, 503-535.

Terzibasi, E., Calamusa, M., Novelli, E., Domenici, L., Strettoi, E., and Cellerino, A. (2009). Age-dependent remodelling of retinal circuitry. Neurobiol Aging *30*, 819-828.

Thumm, M., Egner, R., Koch, B., Schlumpberger, M., Straub, M., Veenhuis, M., and Wolf, D.H. (1994). Isolation of autophagocytosis mutants of Saccharomyces cerevisiae. FEBS Lett *349*, 275-280.

Tian, Y., Bustos, V., Flajolet, M., and Greengard, P. (2011). A small-molecule enhancer of autophagy decreases levels of Abeta and APP-CTF via Atg5-dependent autophagy pathway. Faseb J *25*, 1934-1942.

Titorenko, V.I., Keizer, I., Harder, W., and Veenhuis, M. (1995). Isolation and characterization of mutants impaired in the selective degradation of peroxisomes in the yeast Hansenula polymorpha. Journal of bacteriology *177*, 357-363.

Tomaru, U., Takahashi, S., Ishizu, A., Miyatake, Y., Gohda, A., Suzuki, S., Ono, A., Ohara, J., Baba, T., Murata, S.*, et al.* (2012). Decreased proteasomal activity causes age-related phenotypes and promotes the development of metabolic abnormalities. Am J Pathol *180*, 963-972.

Tsukada, M., and Ohsumi, Y. (1993). Isolation and characterization of autophagy-defective mutants of Saccharomyces cerevisiae. FEBS Lett *333*, 169-174.

Umino, Y., Everhart, D., Solessio, E., Cusato, K., Pan, J.C., Nguyen, T.H., Brown, E.T., Hafler, R., Frio, B.A., Knox, B.E.*, et al.* (2006). Hypoglycemia leads to age-related loss of vision. Proc Natl Acad Sci U S A *103*, 19541-19545.

Vakifahmetoglu-Norberg, H., Xia, H.G., and Yuan, J. (2015). Pharmacologic agents targeting autophagy. J Clin Invest *125*, 5-13.

Valdor, R., Mocholi, E., Botbol, Y., Guerrero-Ros, I., Chandra, D., Koga, H., Gravekamp, C., Cuervo, A.M., and Macian, F. (2014). Chaperone-mediated autophagy regulates T cell responses through targeted degradation of negative regulators of T cell activation. Nat Immunol *15*, 1046-1054.

Varela, C., Igartua, I., De la Rosa, E.J., and De la Villa, P. (2003). Functional modifications in rod bipolar cells in a mouse model of retinitis pigmentosa. Vision Research *43*, 879-885.

Vingtdeux, V., Chandakkar, P., Zhao, H., d'Abramo, C., Davies, P., and Marambaud, P. (2011). Novel synthetic small-molecule activators of AMPK as enhancers of autophagy and amyloid-beta peptide degradation. Faseb J *25*, 219-231.

Wang, Y., Martinez-Vicente, M., Kruger, U., Kaushik, S., Wong, E., Mandelkow, E.M., Cuervo, A.M., and Mandelkow, E. (2009). Tau fragmentation, aggregation and clearance: the dual role of lysosomal processing. Hum Mol Genet *18*, 4153-4170.

Wu, K.H., Madigan, M.C., Billson, F.A., and Penfold, P.L. (2003). Differential expression of GFAP in early v late AMD: a quantitative analysis. Br J Ophthalmol *87*, 1159-1166.

Yamamoto, Tagawa, Yoshimori, Moriyama, Masaki, and Tashiro (2011). Bafilomycin A1 prevents maturation of autophagic vacuoles by inhibiting fusion between autophagosomes and lysosomes in rat hepatoma cell line, H-4-II-E cells. Cell Struct Funct *23*, 33–42.

Yang, J., Bian, W., Gao, X., Chen, L., and Jing, N. (2000). Nestin expression during mouse eye and lens development. Mechanisms of development *94*, 287-291.

Yang, Q., She, H., Gearing, M., Colla, E., Lee, M., Shacka, J.J., and Mao, Z. (2009). Regulation of neuronal survival factor MEF2D by chaperone-mediated autophagy. Science *323*, 124-127.

Young, A.R., Chan, E.Y., Hu, X.W., Kochl, R., Crawshaw, S.G., High, S., Hailey, D.W., Lippincott-Schwartz, J., and Tooze, S.A. (2006). Starvation and ULK1-dependent cycling of mammalian Atg9 between the TGN and endosomes. J Cell Sci *119*, 3888-3900.

Yu, Z.Q., Ni, T., Hong, B., Wang, H.Y., Jiang, F.J., Zou, S., Chen, Y., Zheng, X.L., Klionsky, D.J., Liang, Y.*, et al.* (2012). Dual roles of Atg8-PE deconjugation by Atg4 in autophagy. Autophagy *8*, 883-892.

Yuan, W., Tuttle, D.L., Shi, Y.J., Ralph, G.S., and Dunn, W.A., Jr. (1997). Glucose-induced microautophagy in Pichia pastoris requires the alpha-subunit of phosphofructokinase. J Cell Sci *110 (Pt 16)*, 1935-1945.

Zhang, Y., Gao, X., Saucedo, L.J., Ru, B., Edgar, B.A., and Pan, D. (2003). Rheb is a direct target of the tuberous sclerosis tumour suppressor proteins. Nat Cell Biol *5*, 578-581.

Zhou, D., Li, P., Lin, Y., Lott, J.M., Hislop, A.D., Canaday, D.H., Brutkiewicz, R.R., and Blum, J.S. (2005). Lamp-2a facilitates MHC class II presentation of cytoplasmic antigens. Immunity *22*, 571-581.

Zhou, Z., Doggett, T.A., Sene, A., Apte, R.S., and Ferguson, T.A. (2015). Autophagy supports survival and phototransduction protein levels in rod photoreceptors. Cell Death Differ *22*, 488-498.

ABREVIATIONS

AP(s): autophagosome(S)

ATG: autophagy related genes

b- phot: b-photopic wave

bp: base pair

b-scot: b-scotopic wave

CMA: chaperone mediated autophagy

CNS: central nervous system

CSV: comma separated value

Da: Daltons

DAPI: 4',6-diamidino-2-phenylindole

DKO: double knockout

EBSS: Earle´s Balanced Salt Solution

ERG: electroretinogram

GCL: ganglion cell layer

GFAP: glial fibrillary acidic protein

GFP: green fluorescent protein

HCQ: hydroxychloroquine

Hsc70: 70-kD heat shock cognate protein

INL: inner nuclear layer

IPL: inner plexiform layer

KD: knock down

LAMP2: Lysosome-associated membrane protein 2

LC3: microtubule-associated protein 1A/1B-light chain 3

MEFs: murine embryonic fibroblasts

mTOR: mammalian target of rapamycin

N/L: ammonium chloride and leupeptin

NBR1: neighbour of BRCA1 gene

ONL: outer nuclear layer

OP: Oscillatory potential

OPL: outer plexiform layer

PAS: pre-autophagosomal structure

PBS: phosphate buffered saline

PE: phospatidylethanolamine

PFA: paraformaldehyde

PGK: phosphoglycerate kinase

PI: proteases inhibitors

PI3K(C3): phosphoinositide 3-kinase (complex III)

PKCα: protein kinase C alpha

PQ: paraquat

RGB: red green blue

RGC: retinal ganglion cells

ROS: reactive oxidative species

ROS: reactive oxidative species

RPE: retinal pigment epithelium

SEM: standart error of the mean

Std: Standard deviation

STR: scotopic threshold responses

STS: staurosporin

SUMF1: sulfatase modifying factor 1

TSA: trichostatin A

TUNEL: TdT- mediated dUTP Nick-End Labeling

vs: versus

FIGURES INDEX


VNIVERSITAS COMPLVTENSIS
MATRITENSIS


CSIC
CIB